Experimental Constraints on Silicate Perovskite Forming Reactions and Elastic Properties: Geophysical Implications for Chemical Heterogeneity in the Deep Mantle

Dissertation

zur Erlangung des Grades eines

Doktors der Naturwissenschaften

-Dr. rer. nat.-

der Fakultät für Biologie, Chemie und Geowissenschaften

der Universität Bayreuth

vorgelegt von

Ashima Saikia

2007

Vollständiger Abdruck der von der Fakultät für Biologie, Chemie und Geowissenschaften der Universität Bayreuth genehmigten Dissertation, zur Erlangung des akademischen Grades Doktors der Naturwissenschaften (Dr. Rer. Nat.).

Prüfungssausschuß:

Prof. David Rubie, Universität Bayreuth	(1. Gutachter)
Prof. F. Langenhorst, Universität Jena	(2. Gutachter)
Prof. Josef Breu, Universität Bayreuth	
Prof. L. Dubrovinsky, Universität Bayreuth	
Prof. Klaus Bitzer, Universität Bayreuth	
Prof. Ludwig Zöller, Universität Bayreuth	
Prof. S. Peiffer, Universität Bayreuth	

Datum der Einreichung der Dissertation:	5th October, 2007
Datum des Wissenschaftlichen Kolloquiums	6th February, 2008

Acknowledgements

I feel immense pleasure in availing this opportunity for expressing my deepest sense of gratitude and regards to my supervisors, Dr. Dan Frost and Prof. Dave Rubie for their dynamic guidance, constructive suggestions and untiring efforts extended during my entire doctoral research work at the Bayerisches Geoinstitut, Universität Bayreuth, Germany.

I am acknowledging my obligations to the Elitenetzwerk Bayern, International Graduate School program for funding my research projects and the administration of the Bayerisches Geoinstitut, for providing me necessary facilities to pursue my work.

More so I am indebted for substantial help and invaluable suggestions to Dr. Tiziana Boffa Ballaran with whom I carried out my entire diamond anvil cell work, to Prof. Masaki Akaogi, University of Gakushuin, Tokyo (Japan) for allowing me to use his laboratory facility for calorimetric measurements, to Dr. Catherine McCammon for helping me out with the Mössbauer measurements and analysis, to Dr. Nobuyoshi Miyajima for assistances in the TEM studies and to Dr. Florian Heidelbach for the SEM studies and for the German translation of my thesis summary.

I offer my special thanks to the entire technical and administrative stuff of the Bayerisches Geoinstitut for all the assistances.

Last but not the least I thank all who have directly and indirectly sympathized with me in completing my entire dissertation.

I remain

Ashima Saikia

Bayreuth, October 2007

Table of Contents

Zusammenfassung

Im Rahmen der vorliegenden Doktorarbeit wurden drei experimentelle Untersuchungen durchgeführt, um zu verstehen, wie die Zusammensetzung des Erdmantels die Stabilität von Mineralen und ihre elastische Eigenschaften bestimmt, und wie diese wiederum die seismischen Eigenschaften des tiefen Erdmantels beeinflussen. Die Phasenbeziehungen von Calciumsilikat-Perowskit wurden in Hochdruck-Hochtemperaturexperimenten untersucht, um den Effekt seiner Bildung auf die Charakteristika der seismischen Diskontinuität bei 520 km Tiefe im Erdmantel zu bestimmen. Der Effekt von variabler Zuammensetzung auf die Kompressibilität von Magnesiumsilikat-Perowskit wurde untersucht, um die geophysikalischen Konsequenzen chemischer Heterogenität im Erdmantel zu verstehen. Kalorimetrische Messungen der Granatmischreihe Pyrop-Majorit wurden durchgeführt, um grundsätzliche thermodynamische Daten für die Modellierung der Bildungsreaktionen von Magnesium- und Calciumsilikat-Perowskit bereitzustellen.

(i) **Die Calciumsilikat-Perowskit bildende Reaktion in der Übergangszone des Erdmantels: Implikationen für seismische Diskontinuität in der mittleren Übergangszone bei 520 km Tiefe.**

Globale seismische Beobachtungen zeigen, dass das Auftreten der seismischen Diskontinuität bei 520 km Tiefe in der mittleren Mantelübergangszone ein komplexes Erscheinungsbild hat. In einigen Regionen des Erdmantels erscheint diese Diskontinuität in zwei Diskontinuitäten in leicht unterschiedlichen Tiefen aufgespalten zu sein. Es ist daher vorgeschlagen worden, dass unter den Bedingungen der mittleren Übergangszone ausser dem Phasenübergang von

$(Mg,Fe)_2SiO_4$ Wadsleyit zu Ringwoodit auch die Entmischung von Calciumsilikat-Perowskit aus Majorit-Granat fähig ist, eine seismische Diskontinuität zu erzeugen.

Experimente mit der Vielstempelpresse wurden durchgeführt, um das Tiefenintervall der Bildungsreaktion von Calciumsilikat-Perowskit als Funktion von Druck, Temperatur und Majorit-Granatgehalt zu untersuchen und zu bestimmen, ob sie die beobachtete Aufspaltung der seismischen Diskontinuität bei 520 km Tiefe verursachen könnte. Unsere Resultate zeigen, dass die Entmischung von Calciumsilikat-Perowskit aus Majorit-Granat eine nicht-lineare Funktion des Druckes ist, was in einer relativ hohen Produktion von Calciumsilikat-Perowskit über einen schmalen Druckbereich hinweg resultiert. Der berechnete seismische Impedanzkontrast für diese Reaktion ist in guter Übereinstimmung mit seismischen Beobachtungen für eine aufgespaltene Diskontinuität bei 520 km Tiefe. Dagegen können Temperaturschwankungen im Erdmantel alleine nicht erklären, warum die Diskontinuität bei 520 km Tiefe in manchen Bereichen des Erdmantel aufgespalten ist und in anderen nicht. Die effektive Clapeyron-Steigung der Bildungsreaktion von Calciumsilikat-Perowskit deutet darauf hin, dass die Tiefe, bei der sie mit dem Phasenübergang von Wadsleyit zu Ringwoodit zusammenfallen würde, sehr viel grösser als 520 km ist, wo auch generell nur eine einzige Diskontinuität beobachtet wird. Daher ist die Aufspaltung der Diskontinuität bei 520 km sehr wahrscheinlich das Resultat unterschiedlicher Calciumgehalte des Erdmantels, verursacht entweder durch unterschiedliche Mantelfertilität oder unterschiedlich hohe Anteile von re-integrierter ozeanischer Kruste. Die Aufspaltung der seismischen Diskontinuität bei 520 km Tiefe ist daher ein empfindlicher Indikator der Mantelheterogenität.

(ii) **Eine Bestimmung der Zustandsgleichung von Magnesiumsilikat-Perowskit Einkristallen mit Gehalten von Fe und Al; Implikationen für die elastischen Eigenschaften des unteren Erdmantels.**

Magnesiumsilikat-Perowskit, die vorherrschende Phase im unteren Erdmantel, enthält zusätzlich zu zwei- und dreiwertigem Fe auch signifikante Anteile von Al. Die trivalenten Kationen Fe^{3+} und Al^{3+} können in die Magnesiumsilikat-Perowskitstruktur entweder durch gekoppelte Substitution auf den Mg und Si Positionen oder durch einfache Substitution nur

auf den Si Plätze eingebaut werden, wobei im letzteren Fall der Ladungsausgleich durch die Bildung von Sauerstoff-Leerstellen hergestellt wird. Bisherige Untersuchungen lieferten keine eindeutigen Ergebnisse in Hinsicht auf den Einfluss von Fe^{3+} und Al^{3+} auf die elastischen Eigenschaften, sowie darauf, welches der bevorzugte Substitutionsmechanismus unter den Bedingungen des unteren Erdmantels ist. Diese Eigenschaften sind aber entscheidend, wenn die Konsequenzen chemischer Heterogenität im unteren Erdmantel bestimmt werden sollen.

Messungen der Zustandsgleichung von gut charakterisierten Einkristallen von (Fe,Al)-$MgSiO_3$-Perowskit mit unterschiedlichen Gehalten von Fe und Al wurden mithilfe von Diamantstempelpressen kombiniert mit Röntgendiffraktomtrie durchgeführt. Die Einkristalle wurden in Vielstempelpressen bei 25 GPa und 1800-2000°C synthetisiert. Trivalentes Al^{3+} und Fe^{3+} werden durch den gekoppelten Substitutionsmechanismus eingebaut, wobei die Möglichkeit besteht, dass bei niedrigen Fe,Al-Gehalten auch der Einbau mit Hilfe von Sauerstoff-Leerstellen stattfindet. Die Kompressibiltät von Magnesiumsilikat-Perowskit steigt mit steigendem Gehalt von Fe und Al. Die **b**-Achse ist am geringsten kompressibel, während die **a**- und **c**-Achse eine ähnliche Kompressibilität aufweisen. Passt man die Kompressionsdaten einer Birch-Murnaghan Zustandsgleichung dritter Ordnung an, ergeben sich K' Werte von deutlich über 4, und das Kompressionsmodul erniedrigt sich stark mit dem Fe- und Al-Gehalt im Vergleich zu einer Anpassung der Daten an eine Zustandsgleichung zweiter Ordnung. Extrapoliert man die Birch Murnaghan Zustandsgleichung dritter Ordnung, so ergeben sich keine Dichteunterschiede für den Perowskit durch die Substitution mit Al und Fe unter den Bedingungen des unteren Erdmantels. Eine Anpassung dieser Zustandsgleichung mit einem K' von 4 jedoch passt besser zu den durch das geophysikalische PREM Modell vorhergesagten Dichtewerten. Die Substitutionsreaktion $Fe_{VIII}^{3+} + Al_{VI}^{3+} \leftrightarrow Mg_{VIII}^{2+} + Si_{VI}^{4+}$ in Magnesiumsilikat-Perowskit erhöht das Volumen von Perowskit relativ stärker als die Substitutionreaktionen $Al_{VIII}^{3+} + Al_{VI}^{3+} \leftrightarrow Mg_{VIII}^{2+} + Si_{VI}^{4+}$ oder $Fe_{VIII}^{2+} \leftrightarrow Mg_{VIII}^{2+}$. Unsere Ergebnisse zeigen daher ausserdem, dass die Bildung von metallischem Fe durch Disproportionierung im unteren Erdmantel bevorzugt stattfindet, was erklärt, warum die Fe^{3+} Konzentrationen im unteren Erdmantel wahrscheinlich hoch sind.

(iii) **Eine kalorimetrische Untersuchung der $Mg_3(Mg,Si)Si_3O_{12}$(Majorit)-$Mg_3Al_2Si_3O_{12}$(Pyrop) Granat-Mischkristallreihe.**

Sowohl Magnesium- als auch Calciumsilikat-Perowskit werden im Erdmantel durch Reaktionen gebildet, in denen Majorit eine wichtige Rolle spielt. Bei Drucken über 4 GPa können sowohl Mg als auch Fe auf der Oktaederpostion in Granat für Al substituiert werden, was auch als Majoritsubstitution bezeichnet wird. Diese Substitution kann im Phasendiagramm durch die Konode $Mg_3(Mg,Si)Si_3O_{12}$(Majorit)-$Mg_3Al_2Si_3O_{12}$(Pyrop) beschrieben werden. Thermodynamische Parameter entlang dieser Granat-Mischkristallreihe sind entscheidend für die Modellierung der Bildungsreaktionen von Silikat-Perowskiten.

Die Lösungsenthalpien der Granat-Mischkristallreihe im System Majorit-Pyrop wurden mithilfe der Bleiborat ($2PbO.B_2O_3$) Oxid Tropfenlösungs-Kalorimetrie gemessen. Die Ergebnisse zeigen, dass, beim Pyrop-Endglied anfangend, die Lösungsenthalpien mit steigendem Majorit-Gehalt nicht-linear geringer werden. Ein scharfer Bruch findet sich im Verlauf der Kurve der Lösungsenthalpien bei Pyropgehalten zwischen 32 und 24 mol%, was nahe an dem symmetrie-brechenden Übergang von kubischer zu tetragonaler Struktur liegt. Die thermodynamische Verfeinerung der Daten mithilfe eines regulären, symmetrischen Lösungsmodells für die Granat-Mischkristallreihe erlaubt es, die Daten über den kubisch-tetragonalen Übergang hinweg zu extrapolieren und die Eigenschaften des fiktiven kubischen Majorit-Endgliedes zu erhalten, die für die thermodynamischen Berechnungen erforderlich sind. Ein Wert von -37 kJ/mol wurde für die Lösungsenthalpie von kubischem Majorit-Granat ermittelt, was deutlich niedriger ist als die bisherigen Schätzungen von 5 kJ/mol. Die Daten zeigen ausserdem, dass die $Mg_3(Mg,Si)Si_3O_{12}$(Majorit)-$Mg_3Al_2Si_3O_{12}$(Pyrop) Mischkristallreihe stark nicht-ideale Mischungseigenschaften hat.

Summary

Three experimental investigations have been performed in order to understand how the composition of the mantle may influence mineral stability and elastic properties and how these may influence seismic properties of the deep mantle. The phase relations of calcium perovskite have been studied in high pressure and temperature experiments to examine the effect of its formation on seismic discontinuity features at 520 km depth in the mantle. The effect of varying composition on the compressibility of magnesium silicate perovskite has been examined in order to understand the geophysical consequences of chemical heterogeneity in the lower mantle. Calorimetric measurements of the pyrope-majorite garnet solid solution have been made to provide essential thermodynamic data for modeling the formation reactions of both magnesium and calcium silicate perovskite.

(i) **The calcium silicate perovskite forming reaction in the transition zone of the Earth's mantle: implication for the mid-transition zone seismic discontinuity at 520 km depth.**

Global seismic observations show complexity in the appearance of the mid-transition zone 520 km seismic discontinuity. In some regions of the mantle this discontinuity seems to be split into two discontinuities, at slightly different depths. It has been proposed that at mid-transition zone conditions apart from the $(Mg,Fe)_2SiO_4$ wadsleyite to ringwoodite transition, the exsolution of calcium silicate perovskite from majorite garnet may be capable of producing a seismic discontinuity.

Multianvil experiments were carried out to investigate the depth interval of the calcium perovskite forming reaction as a function of pressure, temperature, and garnet majorite content in order to examine if it could cause the observed split in the 520 km seismic discontinuity. Our results show the exsolution of calcium perovskite from majorite

garnet to be a non-linear function of pressure resulting in formation of a significant proportion of calcium perovskite over a narrow depth interval. Calculated impedance contrast for this reaction is in good agreement with seismic observations for a split 520 km discontinuity. Temperature variation in the mantle alone cannot explain why the discontinuity is split in some regions of the mantle but not in others. The effective Clapyeron slope of the calcium perovskite forming reaction indicates that the depth at which it would converge with that of the wadsleyite to ringwoodite transition is much deeper than 520 km, where a single discontinuity is generally observed. Therefore, the splitting of the 520 km discontinuity is more likely to result from variability in the Ca content of the mantle, either due to varying mantle fertility or due to varying proportions of recycled oceanic crust. The split in the 520 km discontinuity is therefore, a sensitive indicator of mantle heterogeneity.

(ii) **An equation of state study of Fe- and Al-bearing magnesium silicate perovskite single crystals; implications for lower mantle elastic properties**

Magnesium silicate perovskite, the dominant phase of the Earth's lower mantle, contains a significant amount of Al in addition to ferric and ferrous iron. Trivalent cations Fe^{3+} and Al^{3+} may substitute into magnesium silicate perovskite structure either by a coupled substitution onto both Mg and Si sites or by substitution onto the Si site with charge balance provided by the creation of an oxygen vacancy. Previous studies have been inconclusive as to the effects of Fe^{3+} and Al^{3+} on the elastic properties of silicate perovskite and on the favored substitution mechanism at mantle conditions. Such properties are required in order to assess the consequences of chemical heterogeneity in the lower mantle.

Equation of state measurements were carried out using in-situ single crystal X-ray diffraction in a diamond anvil cell on well-characterized (Fe,Al)-$MgSiO_3$ perovskite single crystals with varying Fe and Al contents. These crystals were synthesised using a multianvil apparatus at 25 GPa and 1800-2000°C. The substitution of trivalent Al^{3+} and Fe^{3+} is found to occur by a coupled substitution mechanism with the possibility that a mechanism involving the creation of oxygen vacancies may only be relevant at low trivalent cation concentrations. The compressibility of magnesium silicate perovskite increases with increasing incorporation of Fe and Al. The **b**-axis is least compressible while the **a** and **c** axes have a similar compressibility. Fitting the compression data to a 3rd

order Birch-Murnaghan equation of state, results in values of K' significantly greater than 4, and causes the bulk modulus to decrease strongly with Al and Fe content compared to when a 2nd order equation is employed. Extrapolating using the 3rd order Birch-Murnaghan fit shows there to be no effect on perovskite densities as a result of Al and Fe substitution at lower mantle conditions. However, a fit considering a K' of 4 provides a better match with predicted density for lower mantle when compared to the PREM geophysical model. The $Fe^{3+}_{VIII} + Al^{3+}_{VI} \leftrightarrow Mg^{2+}_{VIII} + Si^{4+}_{VI}$ substitution in magnesium perovskite increases the volume of perovskite more than either the $Al^{3+}_{VIII} + Al^{3+}_{VI} \leftrightarrow Mg^{2+}_{VIII} + Si^{4+}_{VI}$ or $Fe^{2+}_{VIII} \leftrightarrow Mg^{2+}_{VIII}$ substitutions. Our results show that the formation of metallic iron through disproportionation will be favoured at lower mantle conditions, which explains why Fe^{3+} concentrations of the lower mantle are likely to be high.

(iii) **A calorimetric study of the $Mg_3(Mg,Si)Si_3O_{12}$(majorite)-$Mg_3Al_2Si_3O_{12}$(pyrope) garnet solid solution.**

Both magnesium and calcium silicate perovskites are formed in the mantle through reactions that involve majoritic garnet. At pressures above 4 GPa, both Mg and Fe can substitute on to the octahedral Al position in garnet, in what is known as the majorite substitution. This substitution can be described by the join $Mg_3(Mg,Si)Si_3O_{12}$(majorite)-$Mg_3Al_2Si_3O_{12}$(pyrope). Thermodynamic parameters along this garnet solid solution are crucial for modeling the formation reactions of silicate perovskites.

Enthalpies of dissolution of garnet solid-solutions in the system $Mg_3(Mg,Si)Si_3O_{12}$(majorite)-$Mg_3Al_2Si_3O_{12}$(pyrope) were measured by lead borate ($2PbO.B_2O_3$) oxide drop solution calorimetry. Results show that starting from the pyrope end member, the enthalpies of dissolution decrease non-linearly with increasing majorite content. A sharp break in the slope occurs for the enthalpies of dissolution between pyrope contents of 32-mol% and 24-mol%, which is close to the symmetry breaking cubic-tetragonal transition. Thermodynamic refinement of the data using a symmetric regular solution model for the garnet solid solutions enables the data to be extrapolated in composition through the cubic-tetragonal transition to obtain the properties of the fictive cubic $Mg_3(Mg,Si)Si_3O_{12}$(majorite) end member, which is required in thermodynamic calculations. A value -37 kJ/mol was obtained for the enthalpy of solution of the fictive cubic majorite garnet, which is significantly lower than the previous estimate of 5 kJ/mol.

The data also show that the $Mg_3(Mg,Si)Si_3O_{12}$(majorite)-$Mg_3Al_2Si_3O_{12}$(pyrope) solid solution has strong non-ideal mixing properties.

Chapter 1

Introduction

Knowledge of the physical and chemical state of the deep interior of the Earth is the key to understanding its evolution and dynamics. Due to limitations in direct sampling of the deep Earth, most inferences about its interior must be based on indirect information obtained through geophysical and geochemical observations. Experimental data on mineral properties at deep mantle conditions become crucial, particularly in interpreting geophysical observations and assessing their implications for mantle geochemistry and dynamics.

The mantle represents the largest geochemical reservoir of the silicate Earth, comprising about 80% of volume of the total Earth. Our main information on the composition of the mantle comes from xenoliths, pieces of the mantle brought to the surface of the Earth by volcanic activity, and peridotite massifs, sections of the mantle emplaced in the crust by tectonic movements. In addition, the geochemistry of volcanic rocks produced at mid-oceanic ridges by partial melting of the mantle aids our understanding of mantle composition and a comparison with undifferentiated meteorite samples helps to constrain the likely composition of the Earth as a whole. The constancy in composition of erupted basaltic magmas with time infers that the bulk composition of the mantle may be relatively uniform as expected for a convecting mixed reservoir. Aside from a few inclusions in diamonds that may have a deeper origin, samples from the mantle come from depths of no more than 200 km. So, inferences about deep mantle structure need to be based on geophysical observations. Geophysical observations of the mantle have identified a number of globally-observed radial discontinuities that reflect seismic waves. These discontinuities are caused by sharp changes in mantle elastic properties and density. Such

observations have led to the division of the mantle into an upper mantle, a transition zone and a lower mantle, each separated by seismic discontinuities at a particular depth. The discontinuities may result from mineral phase transitions in an isochemical mantle but changes in the chemical composition of the mantle with depth would also be a possible explanation. As different possibilities exist, a range of geophysical observations need to be examined to determine the most likely explanation.

Except for strongly incompatible trace elements that are concentrated in the crust and siderophile and chalcophile elements that partition into the core, the mantle is the major repository for most elements in the Earth. An understanding of mantle composition and its compositional structure has, therefore, great implications for the chemical composition of the entire Earth. In addition geophysical observations contain information on the temperature of the mantle that can be extracted through comparison with experimentally determined measurements. Such information is crucial for understanding the dynamics and thermal evolution of the Earth.

1.1. Mantle mineralogy: inferences from petrological observations, seismology and experiments

Xenoliths brought to the surface by kimberlite and alkali basalt magmas in addition to abyssal and massif peridotites emplaced in the crust, show that the upper part of the mantle is generally an ultramafic rock termed peridotite, which is comprised of the minerals olivine, clinopyroxene, orthopyroxene and an Al-bearing phase. At depths shallower than 70 km, this Al bearing phase is plagioclase, but it transforms to spinel and then garnet with increasing depth. The deepest xenoliths, however, generally become entrained from depths no deeper than ~200 km. Geophysical techniques, primarily seismology, then become the only method for investigating the deeper mantle. Constraints also come from observations of the moment of inertia, gravity, heat flow of the Earth and electrical conductivity measurements. These geophyiscal observations, however, require interpretation using experimentally determined mineral properties and phase equilibria determinations.

The general approach adopted for deciphering the mineralogy of the mantle is to assume that the deep mantle is of a similar composition to the upper mantle as inferred

from peridotite samples and to experimentally determine the mineralogy of this bulk composition as a function of depth along an adiabatic thermal gradient. Based on such mineralogical models sound velocities are then calculated using available thermoelastic parameters and the results are compared with seismic reference models. By examining how well seismic velocities in the mantle match the model determinations, the assumptions made concerning the chemistry and temperature of the mantle as a function of depth can be assessed.

Even though there are limitations in the existing mineral physics data that inhibit a robust interpretation of seismic data, within the uncertainties of the current data a reasonable match is found between seismic observations of S and P wave velocities with depth and models constructed for a peridotitic mantle composition (Cammarano *et al.,* 2005). However, seismic tomography has shown that heterogeneities of thermal and chemical origin, most likely arising from the presence of subducted lithospheric slabs, exist in the mantle. In addition observations of seismic heterogeneity in the lower mantle do not seem to be well explained by thermal variations alone (Trampert *et al*., 2004). Some observations have also been interpreted to result from the presence of partial melting in the deep mantle (Williams and Garnero, 1996; Karato and Jung, 1998). At pressures > 3 GPa such melting is likely to only arise if the mantle is suitably enriched in volatile elements like H and C at these depths, which also raises questions as to the degree of chemical homogeneity that can be expected in the deep mantle.

Chemical composition of the mantle

Various approaches have been adopted to infer the average chemical composition of the mantle. The simplest approach is to assume that the composition of the mantle is the same as some pristine peridotite samples e.g., KLB1 etc. recovered at the Earth's surface. Ringwood, (1975) proposed a chemical composition based on recombining basaltic partial melt with the refractory mantle residue left behind. At mid-oceanic ridges basalts are generated by approximately 10% partial melting of peridotite mantle. Ringwood argued that the composition of the pristine mantle, that he termed pyrolite, would be the same as a mixture of peridotite melt residue and primitive mid-oceanic ridge basalt (MORB) compositions. Rather than assuming a particular residual and basalt composition, as Ringwood did, an alternative approach is to examine melt extraction trends in peridotite

xenoliths and massifs and extrapolate these trends back to an unmelted precursor (Walter, 2004). Models also exist based on chondritic meteorite compositions (Allegre *et al*., 1995; Javoy, 1995). These models assume that the bulk Earth formed from chondrite meteorite material but that siderophile elements were extracted from this composition to the core leaving most major elements in the mantle in chondritic proportions. Because all undifferentiated meteorites have higher Si/Mg ratios than the upper mantle, such models require an additional reservoir rich in Si to form. Usually it is proposed that Si was extracted either to the core or to the lower mantle. Such models are often cited as evidence that the lower mantle may have a chemical composition different from that of the upper mantle.

Seismic observations of the mantle

Vital constraints can be placed on mantle mineralogy from seismological reference models (Travel time-tables of Jefferys and Bullen, 1940; 1066A, 1066B models of Gilbert and Dziewonski, 1975; PREM Preliminary Reference Earth Model of Dziewonski and Anderson, 1981; IASP 91 model of Kennet and Engdahl, 1991; AK135, Kennet *et al*., 1995; Cammarano *et al.,* 2005). Seismic reference models such as the Preliminary Reference Earth Model (Dziewonski and Anderson, 1981) provide a radially symmetric velocity depth profile of the Earth based on the inversion of body wave travel time data and free oscillations of the Earth. In these models velocities in the Earth's interior are refined to a set of polynomial functions that operate over a specified depth interval, with the assumption that mantle discontinuities occur at predetermined depths. These discontinuity depths have been determined by analyzing seismic waves that are refracted by the discontinuity or from seismic waves that are converted from S to P waves, or visa versa, at the discontinuity. Information on amplitude of these discontinuity jumps and depth interval of velocity change across the discontinuity can also be used to place much needed constraints on mantle chemical structure (Stixrude, 1997).

Pyrolite mineralogy as a function of depth

The variation in the proportion of minerals that would crystallize from a pyrolitic bulk composition as a function of depth is show in Fig. 1.1 for the top 1000 km of the mantle

(Ringwood, 1991). For purposes of discussion this diagram can be conveniently divided into two components, which occupy each side of the diagram. On the left side is olivine and the higher pressure olivine polymorphs, while the right side is composed of the non-olivine Si and Al-rich phases of the mantle. Phase transformations in olivine occur with increasing pressure over very narrow depth intervals, whereas the phase transitions in non-olivine phases are gradual and occur over broad depth intervals. At a depth of 410 km, $(Mg,Fe)_2SiO_4$ olivine transforms to the high-pressure polymorph of wadsleyite β-$(Mg,Fe)_2SiO_4$ which is generally considered to cause the 410 seismic discontinuity that is globally observed at this depth. The 410 km seismic discontinuity marks the top of the transition zone region of the mantle, so called because a transition in seismic velocity gradient occurs within this region. At around 17.5 GPa corresponding to a depth of 520 km, wadsleyite undergoes an iso-chemical phase transition to ringwoodite, which likely causes a weak seismic discontinuity observed regionally at approximately this depth. The bottom of the transition zone and top of the lower mantle occurs at 660 km depth, (approximately 24 GPa), where ringwoodite breaks down to an assemblage of $(Mg,Fe)(Si,Al)O_3$ with the perovskite structure and (Mg,Fe)O magnesiowüstite. This transformation causes a strong globally observed seismic discontinuity at this depth.

Above 3 GPa the non-olivine phases in a pyrolite composition are orthopyroxene and clinopyroxene and the Al-rich phase garnet. With increasing pressure, both orthopyroxene and clinopyroxene components start to partition into garnet. This results from the substitution of Mg, Fe and Si onto the garnet Al octahedral position to create a component with pyroxene stoichiometry called majorite {i.e., $(Mg,Fe)_4Si_4O_{12}$}. By mid-transition zone conditions pyroxenes have completely dissolved into the garnet structure with garnet having the approximate stoichiometry $(Mg,Fe,Ca)_3(Mg,Al,Si)_2Si_3O_{12}$. At mid-transition zone conditions of approximately 18 GPa, $CaSiO_3$ starts to exsolve forming the

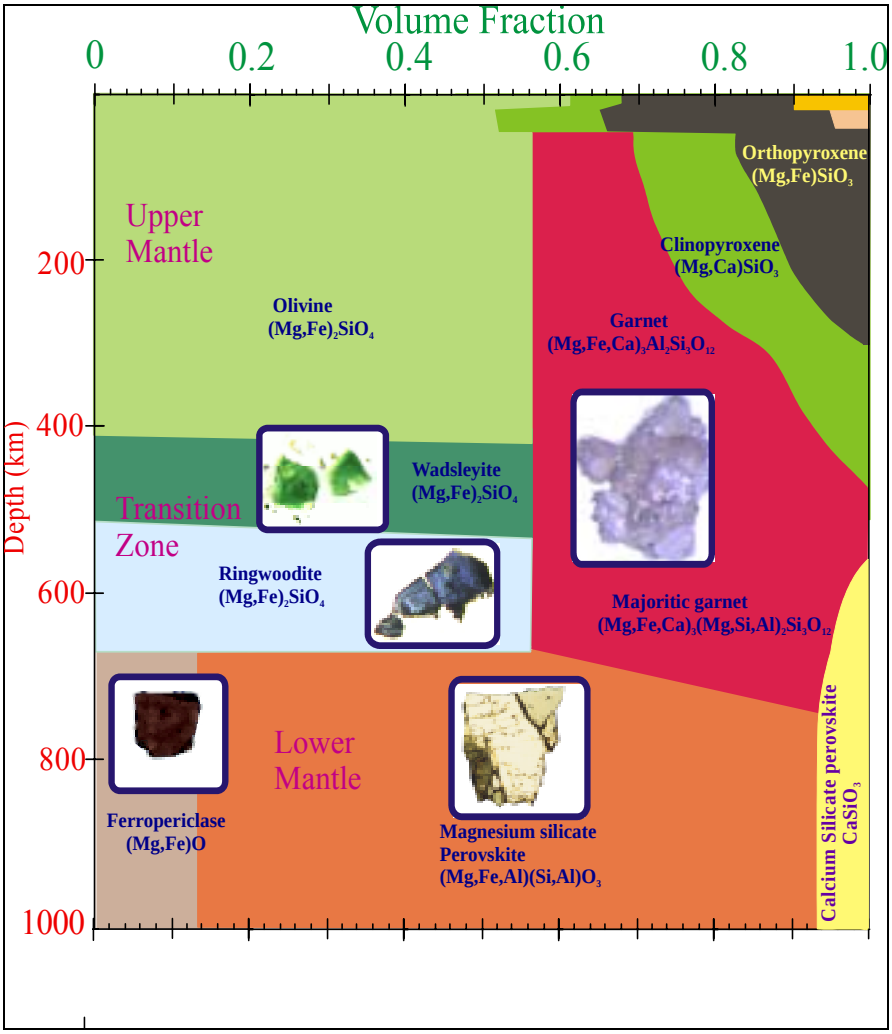

Figure 1.1 Pyrolite mantle mineralogy as a function of mineral volume fraction and depth variation. The small orange and pink region in upper right hand corner represents the stability field of feldspar and spinel respectively. Minerals recovered from high pressure-high temperature experiments are shown in the insets. Field of view of inset is ~200 microns. (With permission from Dr. D. J. Frost)

separate phase calcium silicate perovskite. At the top of the lower mantle the remaining garnet starts to dissolve into magnesium silicate perovskite. By depths of approximately 750 km in the lower mantle, a pyrolite composition assemblage comprises magnesium silicate perovskite, magnesiowüstite and calcium silicate perovskite. This assemblage is believed to be stable throughout the bulk of the lower mantle and only at pressures corresponding to the D'' layer on top of the core mantle boundary does magnesium silicate perovskite transform to a post perovskite polymorph with the structure of $CaIrO_3$ (Murakami *et al*., 2004).

Mantle Heterogeneity

Though the major element composition of the upper mantle appears to have remained uniform over recorded geologic time, trace element and isotopic studies (Sun and McDonough, 1989) imply the presence of significant heterogeneities in the basalt source region. This may indicate the comparatively more mobile nature of incompatible trace elements in comparison to major elements or it may indicate heterogeneities being created by the presence of subducted oceanic lithosphere residing in the mantle (Christensen and Hofmaan, 1994). It is quite likely that a subducted slab would take a significant length of time to be rehomogenized by convective stirring in the mantle (Holzapfel *et al*., 2005). It is, therefore, quite possible that large regions of the mantle are comprised of mechanical mixtures of melt-depleted peridotite and subducted oceanic crust on a variety of length scales. This will have significant implications for the structure and composition of the mantle in addition to its potential effect on geophysical observations.

1.2 Motivation

Changes in mantle mineralogy as a result of phase transformations that occur over relatively short depth intervals have been found to coincide with major seismic discontinuities in the Earth's mantle as shown in Fig. 1.2. A significant number of experimental studies have been devoted to determining the phase relations and physical properties of mineral phases associated with major seismic discontinuities such as those at 410 km (Katsura and Ito, 1989; Irifune and Isshiki, 1998; Kiefer *et al*., 2001; Frost, 2003; Li *et al*., 1998) and 660 km (Ito and Takahashi, 1989; Shim *et al*., 2001; Li and Li, 2003). Of key interest is to understand how temperature and chemical variations in the mantle may affect seismically observable phenomena such as the depth, depth interval and amplitude of the discontinuities in addition to the ambient sound velocity and density of the mantle. For this experimental data are required on the influence of variable mantle chemistry on phase stabilities and elastic properties.

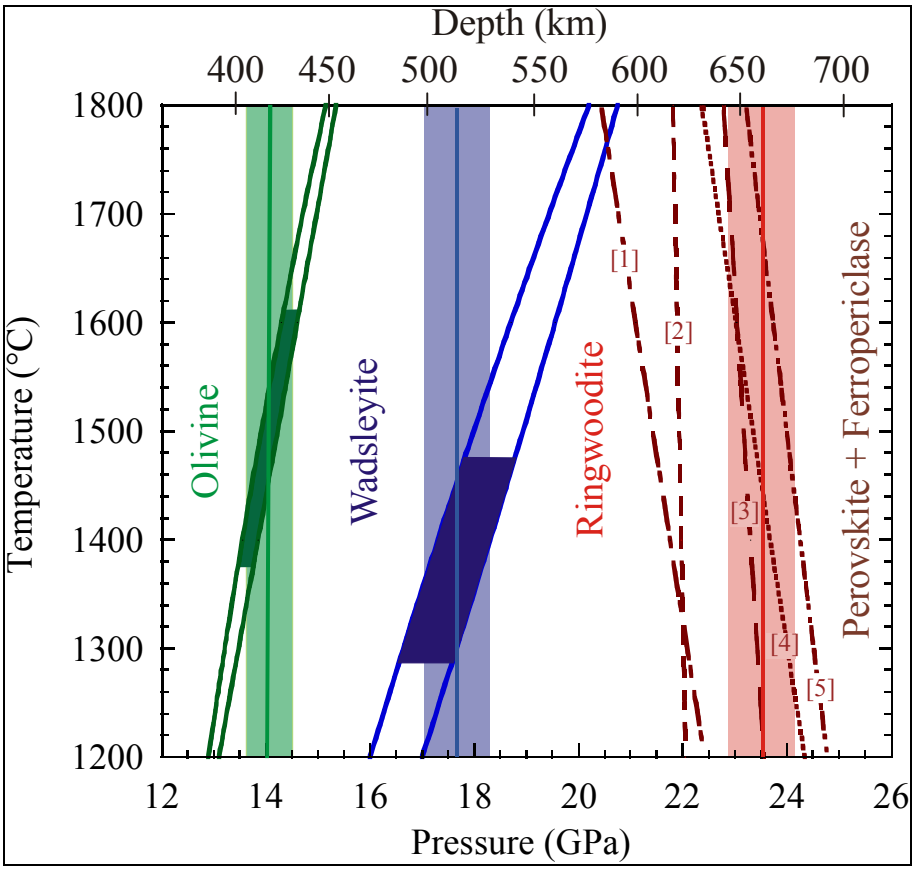

Figure 1.2. Pressure-temperature slopes of phase transformations in the Earth's mantle compared with average seismic discontinuity depths (solid vertical lines) for the 410 km (in green), 520 km (in blue) and 660 km (in red) and global topography (vertical shaded regions). Double curves mark the beginning and end of divariant regions for the olivine to wadslyeite and wadsleyite to ringwoodite transformations, and the shaded area in the curves show the temperature ranges compatible with globally-observed topography of these discontinuities. Individual curves for the Mg_2SiO_4 ringwoodite to perovskite + ferropericalse reaction are shown from different studies [1] Irifune *et al*., (1998) [2] Katsura *et al*., (2003) [3] Fei *et al*., 2004 [4] Ito and Takahashi, (1989) [5] Shim *et al.*, (2001). (With permission from Dr. D. J. Frost)

The olivine to wadsleyite transformation that causes the 410 km discontinuity occurs in the MgO-FeO-SiO_2 system and is therefore insensitive to chemical variations apart from the Fe/Mg ratio, although large concentrations of H_2O may also have an effect (Wood 1995; Smyth and Frost, 2002; Frost and Dolejs, 2007). The 660 km discontinuity, on the other hand, is likely to be more affected by variations in chemistry because, in addition to the MgO-FeO-SiO_2 system, perovskite will also be influenced by the Al_2O_3 content of the mantle and the Fe_2O_3 content. Recent experimental studies have shown that Fe_2O_3 has a strong affinity for magnesium silicate perovskite, which is stabilized by Al in the structure as a result of a coupled substitution. Such a substitution mechanism can also

affect the elastic properties of perovskite. From this analysis we can expect that the formation of magnesium silicate perovskite in the Earth's mantle is likely to be a complex process both physically and chemically. In addition, however, there is evidence that seismic heterogeneity in the deep lower mantle may exist and that the observed variations are not well correlated with changes in temperature (Trampert *et al.,* 2004). To understand and interpret these observations we require information on how chemistry may influence the elastic properties of major lower mantle minerals.

In addition to major seismic discontinuities, minor weak seismic discontinuities are also known to exist in the Earth's interior such as the Hales discontinuity at about 60-90 km depth, possibly caused by $MgAl_2O_4$ spinel transforming to garnet and the Lehmann discontinuity at 220 km depth that may mark a change in mantle anisotropy. Another weak discontinuity was reported by Shearer, (1990), from the mid-transition zone at 520 km depth. This has been considered to be caused by the wadsleyite to ringwoodite transition. However, recent findings of Deuss and Woodhouse, (2001) show that this discontinuity is split at some locations in the mantle into two distinct discontinuities one closer to 500 km and the other at approximately 560 km. The most likely explanation for the occurrence of a split in the 520 is that it results from the formation of calcium silicate perovskite ($CaSiO_3$) from majoritic garnet, which also occurs in this depth range. Previously the calcium silicate perovskite forming reaction had been poorly studied in pressure-temperature space and it was hard to constrain the exact pressure and temperature range over which it occurs. Studying this reaction is further complicated by the fact that majoritic garnet from which $CaSiO_3$ perovskite exsolves is a multi-component solid solution and as such the exsolution reaction is likely to be dependent on a significant number of variables.

A number of issues have remained unsolved about perovskite-forming reactions in the Earth's mantle, for which laboratory studies can provide substantial information. For instance,

(i) The pressure, temperature and compositional effects on the formation of calcium silicate perovskite from majorite garnet have remained unaddressed. This exsolution reaction could possibly cause a seismic discontinuity but the existing data are insufficient to verify this.

(ii) With the experimental observation that perovskite has a strong affinity for Fe^{3+} and that Fe^{3+} incorporation is coupled to the Al content in perovskite, an important question is how Fe^{3+} partitioning will effect the density of magnesium silicate perovskite. There are no systematic studies on the effects of varying bulk Fe content on the density and equation of state of Al-bearing perovskite. Such data will not only be important in modeling the amplitude of the 660 km discontinuity but are also critical for interpreting evidence for chemical heterogeneity in the lower mantle.

(iii) The substitution mechanism of trivalent cations Al^{3+} and Fe^{3+} into the magnesium silicate perovskite structure remains to be understood and the conditions of pressure, temperature and composition where different possible substitution mechanisms dominate are unclear. Thermodynamic modeling of the stability fields of different substitution mechanisms requires information on how they influence the perovskite molar volume, which has not been studied in the past.

(iv) Another aspect important to the study of both magnesium and calcium silicate perovskite forming reactions is to constraint the thermodynamic properties of the precursor phases of these transformations in order that thermodynamic properties of these lower mantle minerals can be determined through modeling of phase equilibria data. Only through the development of suitable thermodynamic models can experimental results be extrapolated, for example, to important lower temperature ranges, where reaction kinetics inhibits laboratory experiments. Both perovskite-forming reactions involve garnet and will be influenced by the composition of garnet particularly, the Al_2O_3 content of the garnet. Thermodynamic data for the garnet–majorite solid solution is crucial to understanding the silicate perovskite forming reactions. Such data will also constrain how the thermodynamic properties evolve as garnet undergoes a symmetry change from cubic to tetragonal.

1.3. Aims of the study

The aims of this research are to experimentally assess the effects of chemistry and temperature on the calcium silicate perovskite ($CaSiO_3$) forming reaction and to determine the effects of varying chemistry on the density and elastic properties of magnesium silicate perovskite ($MgSiO_3$). To achieve this a series of phase equilibria, synthesis and compressibility experiments have been performed. A major motivation in this work has been to determine the properties required to model phase transformations and seismic velocities in the mantle. Mineral transformations at high pressure can be better understood using thermodynamic modeling that aids extrapolation to a wide range of conditions and helps to constrain important parameters such as high-temperature elastic properties. For this reason calorimetric measurements were also performed to independently assess thermodynamic parameters for the pyrope-majorite garnet solid solution.

Three experimental investigations were carried out with following aims:

(i) Multianvil experimental study of calcium perovskite forming reaction from majorite garnet.

At mid-transition zone depths corresponding to pressures of approximatly 16 GPa, the total Ca content of the mantle contained in the majorite garnet phase. With increasing pressure however, majoritic garnet reaches saturation in the $CaSiO_3$ component and starts to exsolve $CaSiO_3$ perovskite.

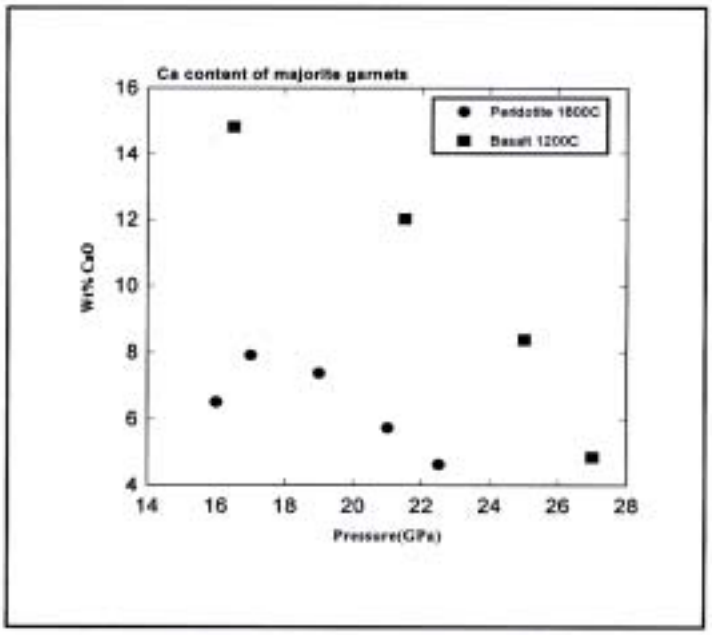

Figure 1.3. CaO content of majorite garnet in peridotitic (Nishihara and Takahashi, 2001) and basaltic (Irifune and Ringwood, 1993) compositions.

Fig. 1.3, shows the Ca content of majorite as a function of pressure in a peridotitic and basaltic bulk composition based on existing data of Nishihara and Takahashi, (2001) and Irifune and Ringwood, (1993). The Ca content decreases as $CaSiO_3$ perovskite exsolves with pressure. The results of previous studies are clearly quite different. As the bulk iron content of both these compositions is similar, the major variables which could possibly effect the $CaSiO_3$ solubilty in majorite garnet are pressure, temperature and the garnet Al/Si ratio i.e., the majorite content. In chapter 2 of this study the solubility of $CaSiO_3$ in majorite garnet as a function of these variables has been determined in high-pressure and high-temperature multianvil experiments. From these solubility data the proportion of $CaSiO_3$ perovskite formed in the mantle for any plausible mantle bulk composition at any pressure and temperature can be calculated. Combining the experimental solubility measurements with existing thermodynamic data for $CaSiO_3$ perovskite and garnet, a thermodynamic model has been developed to describe the formation of $CaSiO_3$ perovskite. In addition, the effect of this $CaSiO_3$ perovskite forming reaction on mantle seismic properties has been modeled and is shown to explain the split 520 km discontinuity.

(ii) Equation of state study of (Mg,Fe)(Si,Al)$MgSiO_3$ perovskite using diamond anvil cell.

Recent studies have indicated that the substitution of Al into (Mg,Fe)(Al,Si)O_3 perovskite is coupled to the Fe^{3+} regardless of oxygen fugacity and that a significant portion of the Fe in lower mantle perovskite is, therefore, likely to be in the Fe^{3+} state (McCammon, 1997; Frost *et al*., 2004). The effect of this important substitution on density and elastic properties are poorly constrained. In chapter 3 of this thesis these effects have been systematically investigated by employing single crystal x-ray diffraction in a diamond anvil cell.

Single crystals of suitable size for in-situ X-ray diffraction in a diamond anvil cell were synthesized using a multianvil press. Mössbauer spectroscopic and electron energy loss spectroscopic measurements were carried out on these crystals to precisely characterize the Fe^{3+} and Fe^{2+} contents. Samples were compressed to high pressures and their unit cell parameters were determined in-situ at room temperature. The results constrain the effect of varying iron and aluminum content on the density and elastic properties of magnesium silicate perovskite. Implications for seismic observations of the deep mantle are examined using these results.

(iii) Drop solution calorimetric measurements on the $Mg_3(Mg,Si)Si_3O_{12}$ (majorite)-$Mg_3Al_2Si_3O_{12}$ (pyrope) solid solution.

In order to model perovskite-forming reactions, knowledge of the thermodynamic properties of the minerals from which perovskites form are essential. In chapter 4 of this thesis drop solution calorimetric measurements are described on garnet solid solutions which were performed in order to determine the ideality of this solid solution and the properties of the $Mg_3(Mg,Si)Si_3O_{12}$ majorite end member.

Chapter 2

The calcium silicate perovskite forming reaction in the transition zone of the Earth's mantle, implications for the mid-transition zone seismic discontinuity at 520 km depth.

2.1 Introduction

All the existing mineralogical mantle models consider calcium oxide to be one of the important oxide constituents of the Earth's mantle (Ringwood, 1975; Anderson, 1983; Wänke *et al*., 1984; Allegre *et al*., 1995). So, the role of calcium bearing mantle phases is crucial for understanding mantle dynamics. At mantle conditions, the primary calcium host phases with increasing depth, are clinopyroxene, garnet, majorite garnet and calcium silicate perovskite respectively (Ringwood, 1991; Canil, 1994). Phase equilibrium studies show that at the upper mantle depths, clinopyroxene becomes increasingly soluble in majorite garnet with increasing pressure and by the mid-transition depth in the Earth's interior, the mantle's entire calcium budget is contained in majorite garnet. When this high-pressure tetragonal garnet phase becomes saturated in the Ca component at approximately 17 GPa, it starts to exsolve calcium silicate perovskite because the solubility of calcium oxide (CaO) in majorite garnet starts to decrease with increasing pressure (Irifune, 1987; Gasparik, 1990; Fei and Bertka, 1999). From the lower part of the transition zone downwards, the amount of calcium perovskite gradually increases with the decreasing solubility of CaO in garnet until the majorite garnet becomes virtually CaO free. The

formation of calcium silicate perovskite therefore is clearly dependent on the conditions where garnet becomes saturated in CaO.

Throughout the lower mantle calcium silicate perovskite is the dominant CaO bearing mineral. The formation of calcium silicate perovskite from garnet in natural systems with peridotitic and basaltic compositions occurs at approximately the same pressure inspite of differences in bulk CaO content, with basaltic compositions containing double the amount of CaO than contained in a peridotitic composition (Irifune and Ringwood, 1993; Nisihara and Takahashi, 2001). This clearly implies that the calcium solubility in garnet is dependent on some variable also other than pressure. The most likely explanation could be that the solubility of CaO in garnet is also dependent on the Al/Si ratio of garnet i.e., the proportion of the majorite component in garnet.

The formation of the dense calcium silicate perovskite mineral in the Earth's interior could cause discontinuities in the speed of sound waves as they pass through the interior, which is detectable at the Earth's surface. Recent seismic observations of the transition zone have identified a discontinuity at the mid-transition zone depth of 520 km often designated as 520d (520 km seismic discontinuity) (Shearer, 1990; Shearer, 1996; Shearer, 2000; Deuss and Woodhouse, 2001; Gilbert *et al*., 2003; van der Meijde *et al.,* 2005; Deuss *et al*., 2006). This discontinuity is found to be split into two discontinuities in some regions of the mantle, one at an approximately 500 km depth and another at a deeper depth of 560 km (Deuss and Woodhouse, 2001). The wadsleyite (β) to ringwoodite (γ) transition is often implicated to be the cause of the 520d (Weidner and Wang, 2000). As the exsolution of calcium silicate perovskite from majoritic garnet occurs at a similar mantle depth, it could also cause a discontinuity and thus result in a double or split 520d (Ita and Stixrude, 1992).

The variability in the depth of these discontinuities could be a strong function of change in either temperature or composition between different regions of the mantle. The most likely major type of chemical variation in the silicate mantle arises due to fractionation of oceanic crust and lithosphere at the mid-oceanic ridges through partial melting. The major elements that are fractionated during partial melting are Al, Ca, Si, and Na, which become concentrated in the oceanic crust and correspondingly depleted in the lithosphere (Walter, 2003). These components are eventually recycled back to the mantle by subduction of oceanic crust. Ongoing convective stirring in the mantle may homogenize these chemically distinct domains, although this may take a significant period of time for

homogenization to achieve local chemical equilibrium (van Keken, 2002; Holzapfel, 2005). However, if these chemically-distinct domains tend to accumulate due to density or rheological contrasts, it may led to formation of long-term heterogeneities in the mantle that are resistant to homogenization (Tackeley *et al*., 1993; Christensen and Hofmann, 1994; Helffrich and Wood, 2001).

The major global seismic discontinuities at 410 km and 660 km depths in the Earth's mantle correspond to phase transformation involving olivine {α-$(Mg,Fe)_2SiO_4$} to its high pressure polymorph of wadsleyite {β-$(Mg,Fe)_2SiO_4$} and ringwoodite {γ-$(Mg,Fe)_2SiO_4$} breaking down to magnesiowüstite and magnesium silicate perovskite respectively (Hellfrich and Wood, 2001). As these phases do not involve components like Ca and Al, which are significantly fractionated in the mantle, discontinuities arising due to these phase transformations tell us little about likely chemical variations in the mantle. However, a seismic discontinuity like that of 520d which may as well arise due to exsolution of calcium perovskite from majorite garnet involving components like Ca and Al, would be very sensitive to large scale mantle chemical heterogeneities; such as those that might result from the presence of significant proportions of remnant subducted oceanic crust in the mantle as the Ca and Al component are significantly fractionated at mid-oceanic ridges.

As majorite garnet is a multi-component solid solution, the exsolution reaction of calcium perovskite from majorite garnet is perceived to be quite complex. Existing data (Irifune and Ringwood, 1993; Gasparik, 1996; Nishihara and Takahashi, 2001; Litasov and Ohtani, 2005) on this reaction are not sufficiently consistent for modeling this reaction over the range of pressure, temperature and bulk composition relevant for the mantle. Moreover, the pressure interval between experiments in existing studies is not narrow enough to accurately describe the shape of the emerging calcium perovskite stability field.

The exsolution of calcium silicate perovskite for a range of mantle compositions was studied in the present work using high-pressure and high-temperature multianvil experiments. The solubility of $CaSiO_3$ in garnet was measured as a function of garnet majorite content between 17 and 23 GPa in the temperature range 1200-1600°C in order to ascertain with high precision, how the depth interval of this reaction compares to the wadsleyite to ringwoodite transition and whether this reaction could occur over a narrow enough pressure interval to cause an observable seismic discontinuity.

2.2. Experimental Details

2.2.1 Synthesis experiments

2.2.1.1 Starting composition synthesis

When we consider major types of mantle rocks such as a peridotite or basalt, the major type of chemical variation in garnets of these rocks arises due to the substitution of the majorite component i.e., (Si, Mg) becoming incorporated into the octahedral Al position in the garnet structure. For this reason we choose four Ca-free garnet compositions on the $(Mg,Fe)_4SiO_{12}$(majorite) - $(Mg,Fe)_3Al_2Si_3O_{12}$(pyrope) join for starting materials (Table 2.1). As can be seen in the Fig. 2.1, a normal mantle peridotitic garnet will be more majoritic than a garnet from a subducted basaltic composition, which has been recycled back to the mantle. Glasses were synthesized out of reagent grade oxide mixtures of SiO_2, Al_2O_3, Fe_2O_3 and MgO by fusing them at 1600°C in a 1-atmosphere furnace followed by rapid quenching in water. Glasses were analyzed for chemical composition by electron microprobe analysis using a point beam operating in wavelength dispersive mode at 15nA and 15kV. Quench recovered glasses were ground to powders and in order to reduce Fe^{3+} content of the glasses to Fe^{2+}, the glass powders were reduced in a CO_2/H_2 gas mixing furnace, at a gas composition of 04/06 H_2/CO_2 (an approximate fO_2 of 2 log units above iron-wüstite buffer) at 650°C for a day. Mössbauer analysis was performed on the reduced glass powders that confirmed the absence of Fe^{3+} in the glass powders. (Details on characterization techniques are discussed in next section).

Table 2.1: Chemical composition of the starting oxide mixes for garnet glass synthesis based on 12 oxygens per formula unit.

Composition	SiO_2	Al_2O_3	FeO	MgO	Total	Si	Al	Fe	Mg	∑Cations
Peridotite	53.0	9.2	5.3	33.5	100	3.63	0.74	0.3	3.33	8
Basalt	48.3	17.4	4.8	29.5	100	3.3	1.4	0.274	3.026	8
Pyrope	43.9	24.9	4.4	26.8	100	3	2	0.249	2.751	8
Majorite	54.8	6.2	5.5	33.5	100	3.75	0.5	0.311	3.439	8

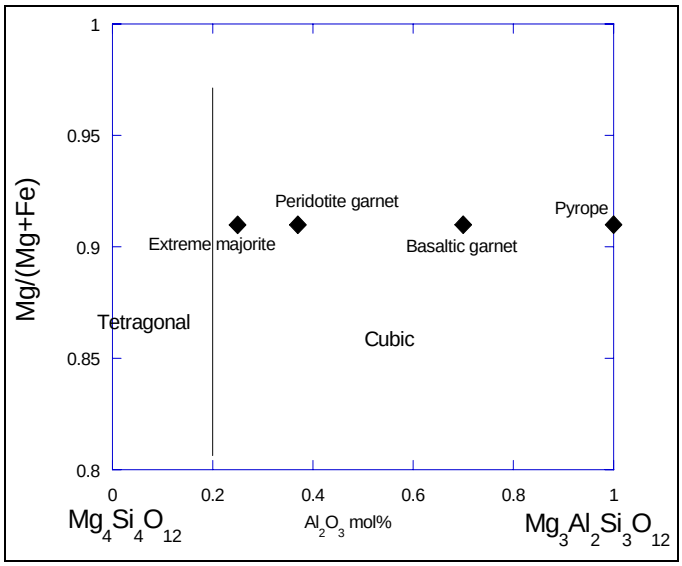

Figure 2.1: The glass starting compositions used in the present study are shown plotted on the majorite–pyrope solid solution join as a function of Mg number.

In order to measure the solubility of Ca in the garnet at high pressure these glass powders were saturated in the $CaSiO_3$ component by adding wollastonite ($CaSiO_3$). The wollastonite phase was synthesized from an oxide mixture of calcium carbonate ($CaCO_3$) and silica (SiO_2) powder. The $CaCO_3$ was first decarbonated for 24 hrs at 225°C in a 1-atmosphere furnace. The oxide mixture of decarbonated $CaCO_3$ and SiO_2 was than placed in a 1-atmosphere furnace for 16 ½ hours at 1000°C. This furnace temperature was scheduled to heat slowly at a rate of 2°C per minute, which ensured slow release of any remaining CO_2 from the sample. These samples were reground and again fused in a 1-atmosphere furnace at 1300°C in successive stages over 48 hours duration in total to finally crystallise wollastonite. Powder X-ray diffraction was employed to confirm the synthesis of wollastonite.

2.2.1.2 Pressure calibrant synthesis

Precise pressure determination is of utmost importance in our study. Therefore, in addition to using the normal oil pressure calibration for our multianvil experiments, we also used in-situ pressure calibration by including an olivine sample in all our experimental runs. Olivine compositions were synthesized from stoichiometric reagent grade oxide mixes of SiO_2, MgO and Fe_2O_3. After thorough grinding of oxide mixture, pellets were made out of

these mixtures, that were reduced in a CO_2/CO gas-mixing furnace at an fO_2 of 14.1, log units at 1000-1200°C depending on the Fe concentration of the samples. After three successive steps, each of 24 hours of reduction and rehomogenization by crushing and grinding, finally homogeneous olivine crystallized. Powder x-ray diffraction on the product phases mixed with Si powder as an internal standard was used for phase identification. (Details of the characterization techniques mentioned herein are discussed in section 2.3.)

2.2.2 Multianvil experimental study

2.2.2.1 Multianvil technique

Over the past 20 years use of multianvil apparatus for high-pressure, high-temperature experiments simulating mantle conditions have increased manifold and a number of publications have reviewed this technique and its applications (Kawai and Endo, 1970; Walker *et al.,* 1990; Rubie, 1993; Rubie *et al.,* 1993; Irifune, 2002; Frost *et al*., 2004; Keppler and Frost, 2005).

A multianvil press works on the concept of reduction of area (A) by applying a constant force (F), thereby increasing the pressure (P) according to the relation P = F/A. Essentially, in a multianvil apparatus, a hydraulic press generates an uniaxial force which is exerted onto a set of 6 steel anvil, which is referred to as the first stage anvils. Two variations of first stage anvil design are known, a split sphere or a spilt cylinder. This set of 6 anvils creates a cubic volume that is filled with a set of eight cubes (either of tungsten carbide or sintered diamond) with truncated corners, which functions as the second stage anvils. These truncated anvils create an octahedral pressure chamber. In this pressure chamber fits in the pressure cell usually an octahedra of MgO containing the sample, which is compressed to the required pressure. A hole is drilled in the MgO octahedra for insertion of a tubular resistance heater, usually made of graphite, metal foils (inconel, platinum, rhenium) or $LaCrO_3$. Stepped heaters, where thickness of the heater wall is increased in the central portion are also used sometimes to reduce thermal gradients across the large sample volumes. Sleeves of insulating material usually ZrO_2 are placed around the heater to prevent excessive heat transport to the tungsten carbide anvils. Experimental sample is placed in the center of the pressure assembly and separated from the heater by an MgO sleeve. MgO spacers fill up the space above and below the sample capsule. The top

MgO spacer has a hole for insertion of thermocouple with an alumina tube for temperature measurements. Pyrophyllite gaskets are used for supporting the truncations and for pressure sealing the high-pressure chamber. The maximum pressure achievable is dependent on the force applied by the hydraulic press, the truncation edge length of the second stage anvils, the edge length of the MgO pressure cell and ultimately by the strength and hardness of the tungsten carbide.

For our experimental investigations in the present work we have used different multianvil apparatus with varied designs located at the Bayerisches Geoinstitut. For our high-pressure studies we have employed different pressure assemblies i.e., different truncation edge lengths of the cubes and different octahedron edge lengths suiting our experimental pressure requirements. We have used tungsten carbide (WC) anvils as the second stage anvils from the commercial suppliers Toshiba (Japan) and Widia (Germany). WC cubes were isolated from the steel anvils by epoxy sheets and copper foils were used for contact between the pressure assembly (detail description of pressure assembly used in our study is given in section 2.2.2.2) and the first stage steel anvils. A thermocouple was inserted into the pressure assembly for temperature measurements and a copper coil protected the thermocouple in the gasket region (Fig. 2.2). A eurotherm controller converted the thermocouple e.m.f. to temperature.

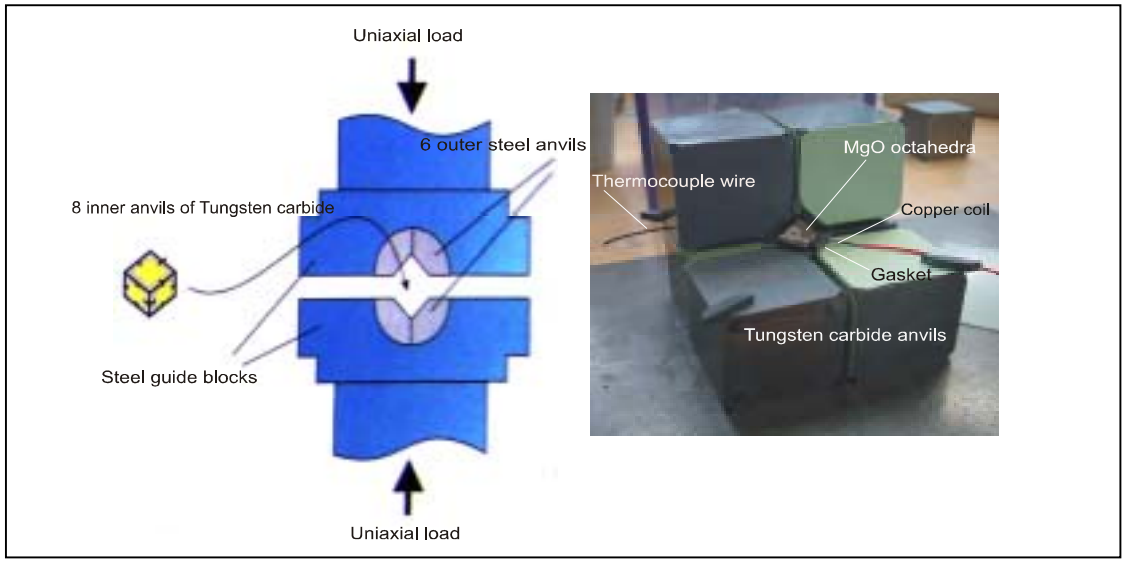

Figure. 2.2: Details of a multianvil apparatus and the experimental set up. On the left is a schematic view showing how the six inner anvils create a cubic space where the 8 tungsten carbide inner anvils fit in containing the pressure cell and directions of application of force. On the left a photograph showing the tungsten carbide anvil set up for an experiment. The MgO pressure medium can be seen placed inside the octahedral cavity formed by truncated tungsten carbide (WC) anvils. Out of the set of eight WC cubes, two cubes are not shown here to show the MgO octahedra inside.

2.2.2.2 Multianvil experiments

Multianvil experiments were performed in the pressure and temperature range of 17-23 GPa and 1200-1600°C, to constrain the $CaSiO_3$ perovskite forming reaction as a function of composition in the mid-transition zone of the Earth's mantle.

Initial experimental considerations

Initially, for our multianvil experiments we mixed the Ca-free garnet glass powder and the $CaSiO_3$ wollastonite in a 1:1 ratio on a trail basis. The first experiment was conducted at 1400°C for duration of 24 hours; on analysis of the run products we saw clear zones in the garnets showing that the experiment had not reached equilibrium (Fig 2.3 A). This led us to increase the experimental duration to 48 hours, which did not improve the equilibrium kinetics. We therefore, increased the experimental temperature to 1600°C. The run product showed a clear lack of $CaSiO_3$ for reaction with the garnet (Fig 2.3 B). So we finally chose a starting mixture of Ca-free garnet glass and $CaSiO_3$ wollastonite in a 1:2 ratio (Fig 2.3 C), where we could clearly observe garnet in equilibrium with calcium perovskite.

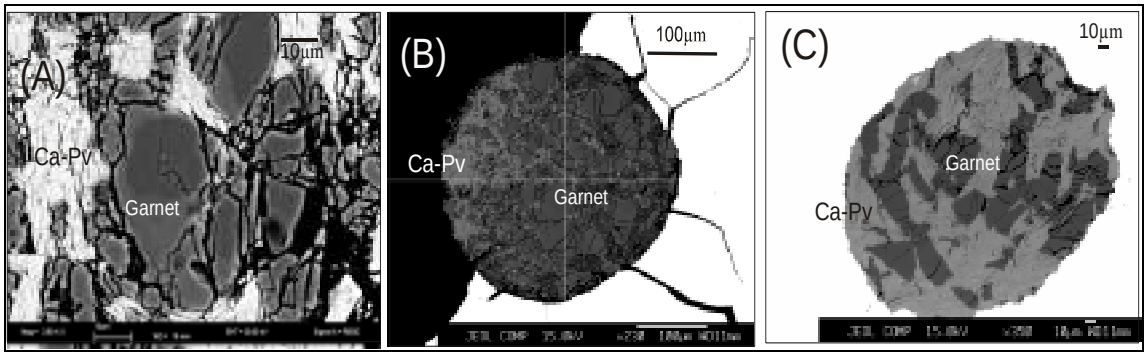

Figure. 2.3: Secondary and back-scattered electron images of different experimental run samples (A) Zonation in majorite garnet showing disequilibrium in a preliminary experiment. (B). Lack of $CaSiO_3$ for further diffusion into majorite garnet. (C). Majorite garnet and calcium perovskite (Ca-Pv) in equilibrium. During the experiment $CaSiO_3$ diffuses into the garnet until it becomes saturated in this component.

For the capsule material we initially tried an Al_2O_3 four-hole sleeve in which we placed the starting compositions in each hole. It reacted away at experimental temperatures and there was huge contamination from the capsule material into the starting materials (Fig 2.4 A). Then we tried a molybdenum (Mo) rod with spark eroded sample chambers for the

capsule; in this case the Fe of the starting compositions diffused into the capsule material. Finally, rhenium rod with spark-eroded sample chambers for the capsule material proved to be the right choice because it was stable at high temperatures and had no effect on the sample composition.

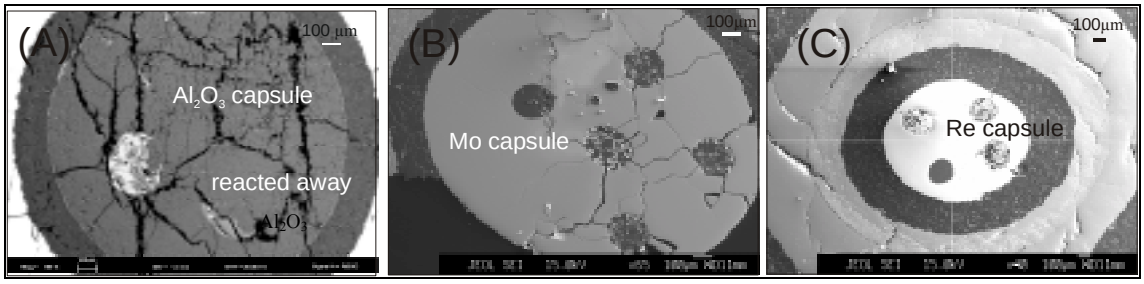

Figure 2.4: Different capsule materials tried out for our multianvil experiments (A) Alumina four hole sleeve which reacted away and only one sample could be recovered that too had contamination of Al_2O_3, (B) Mo (molybdenum) capsule made out of 1 mm diameter Mo rod with five spark eroded holes and (C) Shown here is a radial section through the high-pressure assembly the outer pressure medium and furnace with an inner four chamber Re (rhenium) capsule (white). Three sample chambers contain garnet plus Ca-perovskite assemblages (which appear lighter), while one sample chamber contains a $(Mg,Fe)_2SiO_4$ pressure calibrant sample (darker).

Multianvil experiments were carried out using multianvil presses of 1000-ton and 1200-ton axial compression capacities for this study. Experiments were carried out using 10/5 and 10/4 pressure assemblies i.e., using a Cr_2O_3 doped MgO octahedra of 10 mm edge length in combination with tungsten carbide cubes with 5 or 4 mm truncation edge lengths. A semi-conducting $LaCrO_3$ resistance furnace provided the electrical heating and the sample temperature was monitored using a W3%Re-W25%Re thermocouple, that was inserted axially into the furnace (Fig 2.5). The sample capsule was made out of 1mm long Re rod, that was spark eroded to produce four to five sample chambers each about 250 microns in diameter (Fig 2.4.C). The multi-chambered capsule allows us to run at least three of the garnet glass plus $CaSiO_3$ starting materials with different majorite components (i.e., Al/Si ratios) in three chambers in a single experimental run along with a $(Mg,Fe)_2SiO_4$ powder in another chamber for pressure calibration. A Re disc of 0.025 mm thickness and an alumina disc of 0.2 mm thickness successively covered the upper surface of the sample capsule to avoid reaction with the thermocouple. Experiments were first compressed to the desired load and were subsequently heated to the required temperature for at least 24 hours. Experiments were quenched by cutting the power supply to the

furnace. Decompression of the experiment was usually performed over a period of 17 hours.

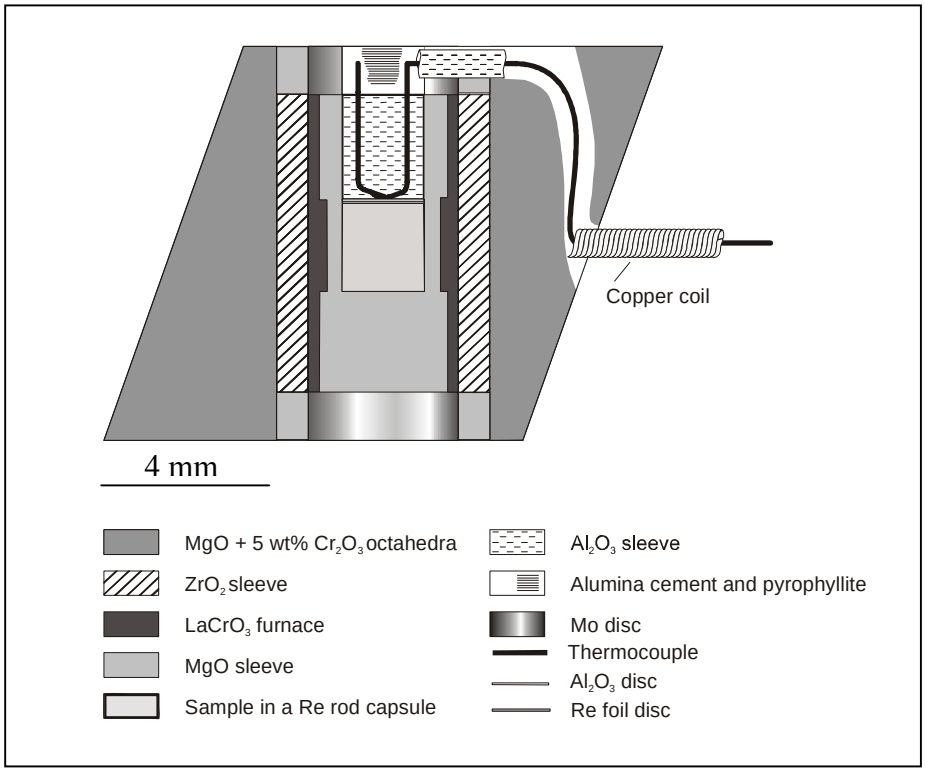

Figure 2.5: A schematic diagram of a 10/4 pressure assembly used for multianvil experiments of the present study, showing an axial cross section through the assembly. (10/4 assembly = 10 mm MgO octahedron edge length and 4 mm tungsten carbide truncation edge length).

During the experiments the starting glass plus $CaSiO_3$ mixture crystallized as garnet and calcium silicate perovskite and $CaSiO_3$ dissolved by diffusion into the garnet. We measured this solubility as a function of pressure, temperature and composition. When the majorite garnet became saturated in the Ca component, it started to exsolve Ca-perovskite with increasing pressure. As the garnet diffusion was found to be slow, we tried out fluxes for our experiments. We did an experiment where we chose the basaltic garnet plus $CaSiO_3$ composition and mixed it with about 5-mol% of two different fluxes B_2O_3 and NaCl. The multi-chambered Re capsule allowed us to put these two fluxed compositions into two capsule chambers along with a composition without flux and a pressure calibrant in the other two chambers in the same experiment. Experiment was carried out at 19.5 GPa (oil bar pressure) at 1400°C. Analysis of the experimental run product showed that the composition with NaCl flux showed no enhancement in CaO solubility in the garnets,

instead it crystallized NaCl crystals. However, the one with the B_2O_3 flux showed significantly enhanced reaction in comparison with the same composition without any flux. This indicated that the B_2O_3 generated melt at the experimental temperature that promoted equilibrium. So, all the subsequent experiments were fluxed with 5-mol% of B_2O_3. This increased the rate of reaction considerably at 1600°C and 1400°C but reaction at 1200°C was still far too slow for equilibrium to be achieved on a feasible time scale.

Reversal experiments

To ensure that we achieved equilibrium in our experiments, reversal experiments were performed using Ca-bearing garnets as the starting material. For this we chose the maximum calcium-bearing garnet compositions from our forward runs. High purity oxide powders of CaO, Fe_2O_3, MgO, Al_2O_3 were mixed in the proper stoichiometric proportions and fused at 1600°C in a furnace and rapidly quenched in water to produce the desired glass phase. Glass powders were reduced under conditions similar to those used for the other glass powders (see section 2.2.1) and were characterized by Mössbauer analysis.

Syntheses of the Ca-bearing garnets were carried out using a 5000-ton multianvil press, where large sample volumes could be utilized. Experiments were performed using 15 mm edge length truncated tungsten carbide cubes, which compressed a 25 mm edge length Cr doped MgO octahedra containing the sample capsule jacketed by an MgO spacer and a $LaCrO_3$ furnace. Sample capsules of 3.5 mm in length and 2 mm in diameter were made out of Re foil, which was in contact with a Re75%W25%-W3%Re97% thermocouple for temperature measurements. Garnets were crystallized at 15 GPa and 1600°C within an experimental duration of 1.5 hours. Phase identification was carried out using powder x-ray diffraction.

Table 2.2: Reversal Ca –bearing garnet glass compositions in cation proportions based on 12 oxygen per formula unit as determined from electron microprobe analysis.

Composition	Si	Al	Fe	Mg	Ca	∑Cations
Ca-Peridotite	3.62	0.65	0.31	2.66	0.80	8
Ca-Basalt	3.37	1.06	0.29	2.32	1.04	8
Ca-Pyrope	3.27	1.34	0.27	1.99	1.20	8
Ca-Majorite	3.67	0.49	0.35	2.83	0.76	8

Reversal experiments were carried out in the pressure range of 20-23 GPa at 1600°C for duration of 24 hours. Reversal experiments too were fluxed with B_2O_3 for promoting reaction kinetics.

The recovered run samples were mounted in epoxy resin and polished on the surface that was perpendicular to the axial direction of the furnace and close to the thermocouple. Samples were analyzed using Raman spectroscopy and composition of the observed phases was determined using an electron microprobe. Some of the samples were made into thin sections for analysis with transmission electron microscopy (TEM) to check for the possible incorporation of boron in the garnet phase. (See Appendix A, Table A 1 for list of phases observed during each experimental run).

2.3 Characterization and analytical techniques employed in this study

Powder x-ray diffraction

X-ray diffraction for phase identification has been a common characterizing technique since discovery of X-ray by Roentgen. The diffraction mechanism is governed by the Bragg's equation $n\lambda = 2d\sin\theta$, where λ is the wavelength of the radiation and d is the spacing between two parallel lattice planes and θ is the glancing angle of incidence and reflection on the lattice planes. This means that the unit cell parameters of a crystal will determine the d spacing for that crystal so the 2θ values for a particular X- ray wavelength will be characteristic of its crystal structure.

The crystallization of the olivines used for pressure calibration, the wollastonite sample and the Ca bearing garnets for reversal experiments was confirmed by X-ray powder diffraction. This technique could detect the presence of minor amount of undesired phases along with the sample. Characterizations were carried out using a Siemens D-5000 diffractometer operating in reflection mode with Cu $K\alpha_{1,2}$ radiation. Data were recorded in the 2θ range of 10°-120°, with a step size of 0.02° and counting time of 4 seconds per step. Silicon (NBS 640b, a = 5.43088Å) was used as an internal standard. The measured peaks were calibrated using the Si peaks. Identification of the phase was carried out using the

Stoe WinXPow software by matching the observed diffraction peaks with that of the reported peaks for the concerned phase as in the database.

Mössbauer Spectroscopy

Mössbauer spectroscopy was employed in this study for determining the oxidation state of Fe in starting glass compositions. In Mössbauer spectroscopy, a radioactive source provides a monochromatic γ radiation, which is allowed to pass through the sample (absorber). As this γ radiation has exactly the same energy needed to excite the nuclei in the sample it leads to a resonant vibration. To maintain this resonance the source is moved relative to the sample, which shifts the energy of the emitted γ radiation based on the Doppler effect. If resonance absorption takes place a detector behind the sample records the count rate as a function of source velocity in (mm /sec), which is the Mössbauer spectrum. Workers like Amthauer *et al*., (2004) and McCammon, (2004) have reviewed details of this technique.

The conventional Mössbauer spectroscopy technique was adopted for checking the oxidation state of Fe in the reduced garnet glass starting compositions. The quenched glasses were crushed to fine powder and were mounted on a sample holder of 12 mm diameter, which accounts for about 5 mgFe/cm^2 absorber thickness. The Mössbauer spectra were recorded at room temperature for durations of 1-2 days in transmission mode on a constant acceleration Mössbauer spectrometer with a nominal 1.85 GBq ^{57}Co source in a 6μ Rh matrix. The velocity scale was calibrated relative to 25 μm α-Fe foil using the positions certified for National Bureau of Standards standard reference material 1541, line width of 0.28 mm/s for the outer lines of α-Fe obtained at room temperature. Mössbauer spectra of the glasses were fitted using the commercially available fitting program RECOIL written by K. Lagarec and D. Rancourt (distributed by Intelligent Scientific Applications Inc., Canada), which is based on an extended Voigt based analytic line shape assuming a Gaussian distribution for Fe oxidation states (Fig. 2.6)

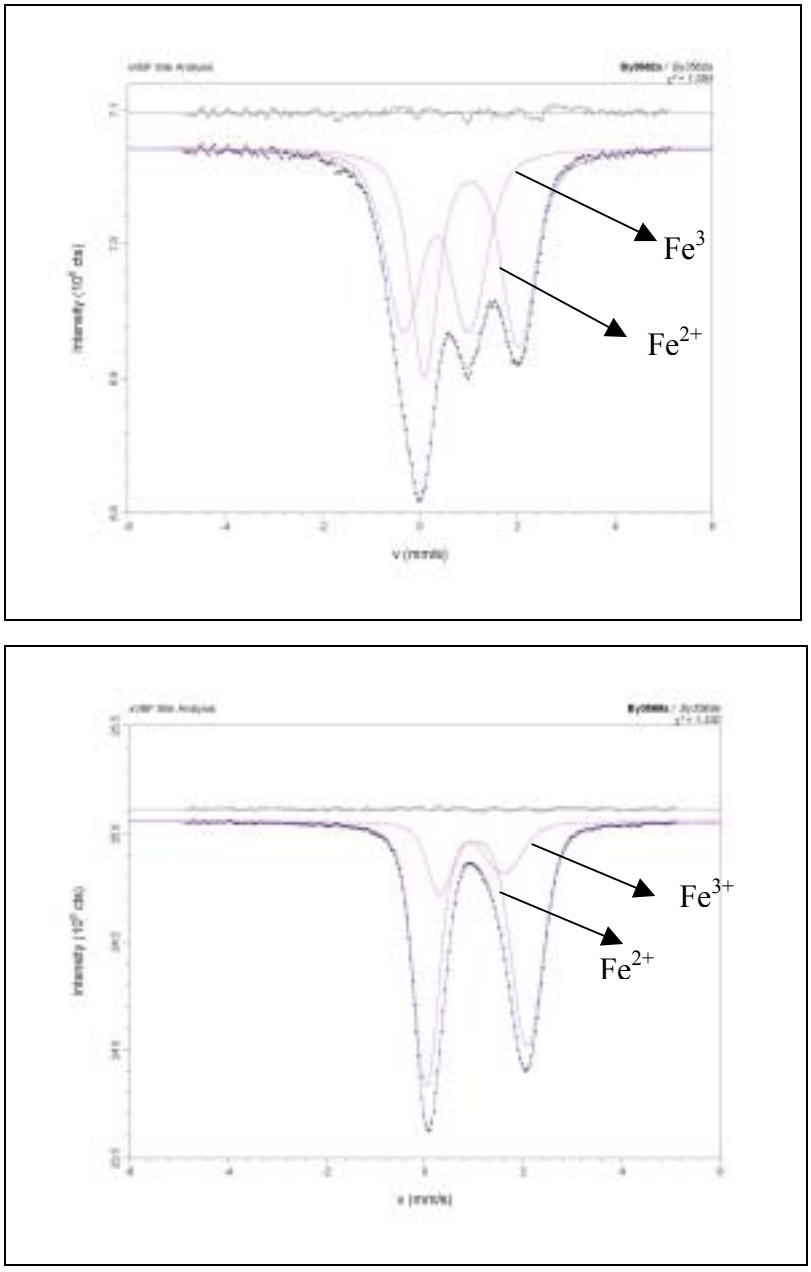

Figure. 2.6: Mössbauer spectra of majorite garnet glass starting composition. Shown here are the spectra collected before reduction (upper one) and after reduction (lower one) of the glass powder in CO_2/H_2 gas mixing furnace. Fe^{3+} can be clearly observed to be reduced after treatment in gas-mixing furnace (see section 2.2.2.1).

Electron microprobe analysis (EPMA)

In this technique a finely focused electron beam is directed at high velocity on a sample to be analyzed. As the electrons impinge upon the sample at high velocity they penetrate a volume of the sample whereby the incident higher energy electrons displace the inner shell electrons of the constituent atoms of the sample. Inner shell vacancies so created will be filled by electrons from outer shell generating characteristic X-rays in the process. These characteristic X-rays are analyzed by a crystal spectrometer (wavelength dispersive mode) or by an energy dispersive analysis system (Heinrich and Newbury, 1991; Reed, 1996)

In the wavelength dispersive mode as used in the present study, the crystal diffracts the various wavelength values of impinging electrons according to Bragg's law. The intensity and position of each spectral line was recorded in an electronic counting device, which was than compared with that of a standard having the same elemental make up to obtain quantitative analysis.

The concentrations of major elements in the quenched glass starting compositions and in the quench recovered run products of high pressure multianvil experiments were determined using the JEOL JXA-8200 WD/ED combined microanalyzer at the Bayerisches Geoinstitut, which is equipped with 5 wavelength dispersive spectrometers. The standard conditions and the measurement conditions for the present study are tabulated in Table.2.3.

Table 2.3: Electron microprobe analysis conditions used in the present study. Abbreviations: TAP (Thallium acid pthalate), PETH (Pentaerythritol high), LIF (Lithium fluoride), P (Peak), B (Background)

Elements	Crystals	Standards	Accl^{n}. voltage	Probe current	Count time (Secs)	
			kV	nA	P	B
Mg	TAP	Enstatite	15	15	20	10
Si	TAP	Andradite	15	15	20	10
Ca	PETH	Andradite	15	15	20	10
Al	TAP	Spinel	15	15	20	10
Fe	LIF	Fe metal	15	15	20	10

The glass samples used as starting materials with size variation from 1 to 2 mm and the octahedra (about 5 mm in diameter) recovered from the multianvil experiments were mounted in epoxy blocks of 25 mm diameter. Rough polishing of the samples was carried out with silicon carbide paper (150-4000 gem) and further fine polishing was done with ¼ micron diamond paste. Samples were then coated with carbon to a thickness of about 11 nm to avoid charging on the surface. Glasses, majorite garnet and calcium perovskite were analyzed at an acceleration voltage of 15 kV, probe current of 15 nA and 20 seconds of counting time at peak position and 10 seconds of background count. A point beam was employed which has an interaction surface of about 1 μm. All the phases were stable under these conditions and quantitative analyses were within a relative statistical deviation of 2%.

Transmission electron microscopy

This technique works on the principle that when a specimen is thin enough, high-energy electrons can pass through it (Williams and Carter, 1996). As boron was used as flux in our multianvil experiments to increase the reaction kinetics, it was essential to check whether the boron became incorporated into the majorite garnet structure during the experiments, because this could affect the solubility of Ca in the majorite garnet. As electron energy loss spectroscopy (EELS) is sensitive to a detection limit of as low as 1-mol% of elements we chose this technique for boron detection.

For this the microprobe samples embedded in epoxy were made into thin sections of about 30μm thickness. Thin section was glued to a glass slide using a glue, which dissolves in acetone. Mo square mesh of 100mesh size were glued on top of thin section such that the regions of interest are in the center of the mesh. After this the meshed thin section is recovered by dissolving the glue in acetone. Further thinning of the sample was carried out using Ar^+ ion beam in a Gatan dual ion mill model 600, at an angle of 14°, 4kV acceleration voltage and 1 mA beam current. At the end of thinning process the acceleration voltage was reduced to 3.5 kV to reduce beam damage. Usually thinning was continued till interference fringes were visible on the edges on inspection by optical microscope, which was about 35 hours in total. Samples were than coated with amorphous carbon about 5 nm using the BAL-TEC, ME020 coating system to avoid charging on the

surface. TEM imaging and EELS measurements were performed on a Philips CM20FEG analytical transmission electron microscope operating at 200 kV equipped with a parallel electron energy loss spectrometer. EELS spectra were collected in diffraction mode. No boron k-edge was observed as expected at around 186 eV (Fig. 2.7)

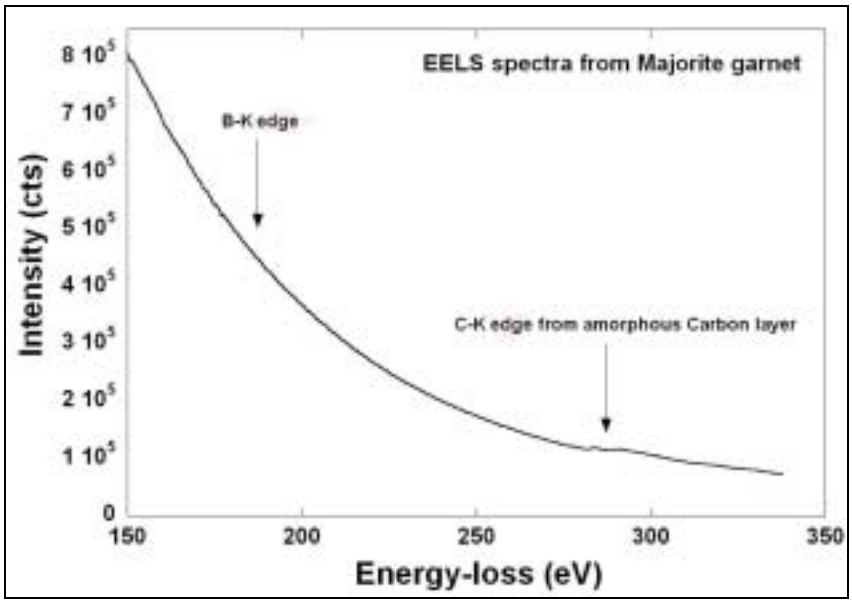

Figure 2.7: EELS spectra of the basaltic garnet composition collected to check for boron incorporation in its structure, as can be seen in the spectra there is no boron peak observed as expected at 186 eV.

Secondary electron microscopy (SEM)

In this technique, a focused beam of electrons is either scanned across a specimen resulting in the generation of secondary electrons, back scattered electrons and also auger electrons. In case of the secondary electrons, as they are emitted from the surfacial atoms of the sample, a quick image of the area where the electron beam is focused is produced. Sample morphology determines the contrast in the image. Moreover, X-rays are also generated in this process as the electron beam interacts with atoms of the sample causing transitions in the electron shells. The emitted X-rays have characteristic energies of the parent elements and detection and measurement of the energy spectrum allows a rapid qualitative elemental analysis, a technique usually known as energy dispersive x-ray spectroscopy (EDX) (Reed, 1996).

In the present study, the SEM technique was used on a routine basis for imaging the high-pressure, high-temperature multianvil run products that had been polished after being embedded in epoxy resin and with carbon coating to reduce charging on the surface (similar to that for EPMA analysis) at an acceleration voltage of 20 KeV and with different magnifications.

Raman spectroscopy

This spectroscopic method is based on the inelastic scattering of light called the Raman effect. When light is allowed to interact with a specimen, it excites the constituent molecules, which subsequently scatter the light. Most of this scattered light has a similar wavelength as the incident light while some of it is scattered with a different wavelength. This inelastically scattered light is the Raman scatter, which results from the changed molecular motions of the sample. The difference in energy between the incident light and Raman scattered light is equal to the energy of the scattering molecule and will be characteristic of a molecule and its environment in a specimen. By plotting the energy difference and the intensity of scattered light we obtain a Raman spectrum (Nasdala *et al*., 2004).

In the present study we used a LABRAM Raman spectrometer with a He-Ne laser with the 632 nm red line excitation for phase identification of our experimental run products. This was especially useful in case of our pressure calibrants where we could easily distinguish between the $(Mg,Fe)_2SiO_4$ polymorphs using this technique. Raman spectra were collected at ambient temperature with an instrumental resolution of 2 cm^{-1} for the peak positions. By comparing the obtained spectra with the relevant standard Raman data available for the mineral phase from the literature we carried out the phase identification (Fig. 2.8)

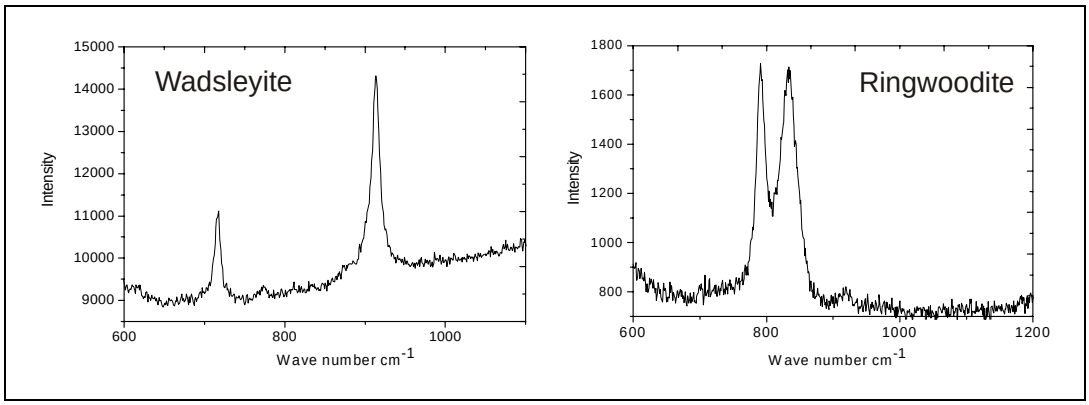

Figure 2.8: Raman spectra of wadsleyite and ringwoodite as crystallized by the in-situ pressure calibrants of our experiments. Phase identification was carried out by comparing these spectra with the existing Raman spectra from the literature for the concerned phase.

2.4. Results

During the high pressure experiments the garnet glass and $CaSiO_3$ compositions crystallized rapidly to garnet and perovskite respectively and $CaSiO_3$ was dissolved into the garnet during the heating period. Experimental durations of at least 24 hours ensured equilibrium compositions at 1600°C at lower pressures. However, in some cases at higher pressures, the inner cores of garnet remained unequilbrated but equilibrium was achieved in the rims with the aid of the B_2O_3 flux as mentioned in the experimental section. As discussed earlier, equilibrium was crosschecked by analyzing the reversal experiments in which Ca-bearing garnets exsolved Ca perovskite at high pressure. We had equilibrium in our experiments because for a given pressure the extent of CaO solubility in the garnet phase after $CaSiO_3$ exsolution converged to the same values as obtained in the forward runs within experimental error. At 1400°C, high Ca-bearing garnet was formed up to pressure of ~20 GPa, beyond which Ca contents in the garnet declined drastically. Time studies indicated that equilibrium was not achieved at these conditions; a possible explanation could be that at these conditions the B_2O_3 flux crystallized. In the case of experiments at 1200°C, even the fluxed experiments failed to reach equilibrium on a time scale of 48 hours. Longer duration requirements were not feasible.

During the experiments the $(Mg,Fe)_2SiO_4$ olivine pressure calibrant crystallized to form co-existing high-pressure phases. Pressure was determined from the Mg_2SiO_4(forsterite)-Fe_2SiO_4(fayalite) phase diagram using the field of coexistence

between $(Mg,Fe)_2SiO_4$ and (Mg,Fe)O magnesiowüstite plus stishovite (SiO_2) (Fig. 2.9). This divariant region extends from the Fe_2SiO_4 ringwoodite to magnesiowüstite plus stishovite transformation at approximately 16 GPa to 23 GPa with the Fe/(Fe+Mg) ratio of both ringwoodite and magnesiowüstite (when coexisting with stishovite) decreasing with increasing pressure. This reaction has been well studied (Matsuzaka *et al.,* 2000; Frost *et al*., 2001; Frost, 2003a). The Fe/(Fe+Mg) ratio of ringwoodite for example decreases by approximately 10% per GPa. As we can determine this ratio with an accuracy of approximately 1%, this gave us a precision in pressure determination of 0.1 GPa. A previous study had shown that the bulk Fe concentration of magnesiowüstite could be apparently high if ferric Fe is present. We calculated the pressure using the ringwoodite Fe concentration and used the phase relations previously determined at a similar oxygen fugacity (Frost *et al*., 2001; Frost, 2003a). In this way we calibrated accurately the pressure of Ca-perovksite formation relative to the pressure of phase transformations in the Mg_2SiO_4-Fe_2SiO_4 system (Frost *et al*., 2001; Frost, 2003b). The absolute error in pressure depends on determinations of end member phase transitions used to construct the existing Mg_2SiO_4-Fe_2SiO_4 phase diagram which are difficult to assess but could be up to 1 GPa. Our study relied more on the high precision of pressures determined relative to the Mg_2SiO_4-Fe_2SiO_4 phase diagram, rather than on accuracy in absolute pressure.

When the magnesiowüstite grains were too small in our experiments to get a reliable analysis, the pressure was determined using the ringwoodite Fe/(Fe+Mg) ratio alone. In those cases where a poorly chosen Fe/(Fe+Mg) ratio of the starting olivine composition led to crystallization of a single phase ringwoodite, pressure was determined from the oil pressure of the multianvil experiment. In experiments where the pressure was measured, the determined pressure showed excellent relationship with the multianvil oil pressure. The relative uncertainty using this calibration curve in comparison to pressures determined from phase relations in Mg_2SiO_4-Fe_2SiO_4 system was approximately ± 0.5 GPa. In some of our experiments the pressure calibrants even crystallized in the stability field of perovskite plus magnesiowüstite and stishovite (Run No.S3478, S3784), see Appendix A, Table A.2 for the perovskite compositions. Experimental results are given in Table 2.4,where the relative pressure errors were calculated using the mismatch between the analysed Fe contents of ringwoodite and magnesiowüstite compared with the phase diagram of Frost *et al.,* (2001).

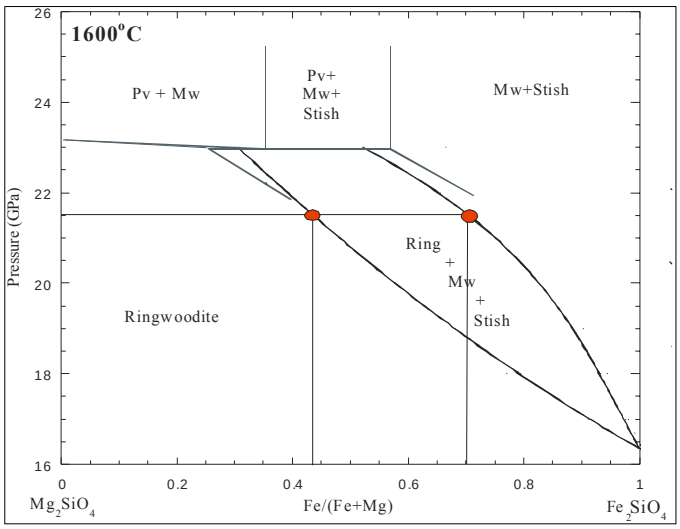

Figure 2.9: Phase relations in the Mg_2SiO_4-Fe_2SiO_4 system between 16-26 GPa at 1600 ^oC (Frost *et al*., 2001) used for calculating the pressures in our experiments. Olivine pressure calibrants during experiments crystallized into its corresponding high pressures phases of ringwoodite, magnesiowüstite and stishovite. From probe data we determined the Fe/Fe+Mg ratio of coexisting ringwoodite and magnesiowüstite after correction for ferric iron content (Frost, 2003a). By plotting the Fe/Fe+Mg values as shown marked by stars we could exactly determine the pressure in each of our experiments.

Table 2.4: Experimental results for garnet compositions recovered from multianvil experiments as determined by electron microprobe analysis for different experimental runs. Results are listed as peridotite, basalt, pyrope and majorite based on the different garnet starting compositions as listed in table 2.1.Listed here are the experimental run numbers, pressures in GPa for each experiment determined as described in text and the cation proportions of the garnet compositions calculated based on 12 oxygen per formula unit. Data in Ring (ringwoodite) and MW (magnesiowüstite) columns are the Fe/Fe+Mg ratios used for calculation of pressure as described in text. (See Appendix A, Table A.3 for the probe data of all experimental runs)

Run no.	Pressure	Si	Al	Fe	Mg	Ca	Total	Ring	MW
1600°C	(in GPa)								
Pyrope									
S3550	19.2(3)	3.41(2)	1.08(4)	0.21(1)	2.25(6)	1.10(4)	8.050	0.626(3)	0.937641
S3549	19.9(2)	3.12(1)	1.52(2)	0.17(2)	2.25(5)	0.90(5)	8.038	0.542(3)	0.87(3)
S3470	18.8(5)	3.32(5)	1.36(4)	0.05(2)	2.03(8)	1.22(1)	7.993		
S3475	22.6(5)	3.11(6)	1.82(6)	0.207(6)	2.47(6)	0.37(3)	7.982		
S3478	23(5)	3.09(2)	1.77(3)	0.28(5)	2.56(6)	0.32(3)	8.023		
S3484	22.3(5)	3.08(5)	1.81(5)	0.24(7)	2.57(7)	0.30(7)	8.011	0.36(2)	
S3490	21.4(5)	3.10(5)	1.76(9)	0.23(1)	2.47(6)	0.44(1)	8.013		
Basalt									
S3551	20.4(3)	3.33(6)	1.11(7)	0.1(1)	2.94(8)	0.61(4)	8.096	0.496(2)	0.88(2)
S3550	19.2(3)	3.29(2)	1.36(4)	0.178(9)	1.90(6)	1.27(7)	8.023	0.626(3)	0.937641

S3549	19.9(2)	3.38(1)	1.14(3)	0.16(2)	2.70(3)	0.65(3)	8.044	0.542(3)	0.87(3)
S3548	19.5(2)	3.41(2)	1.04(3)	0.30(2)	2.56(3)	0.75(3)	8.068	0.605(5)	0.863(4)
S3547	19.5(5)	3.45(2)	1.04(2)	0.21(1)	2.58(5)	0.74(4)	8.020	0.592(2)	0.844(6)
S3764	21.2(3)	3.34(3)	1.26(2)	0.21(2)	2.85(6)	0.35(1)	8.021	0.426(5)	0.73(1)
S3757	20.7(5)	3.36(3)	1.29(4)	0.199(8)	2.65(3)	0.47(3)	7.990	0.469(2)	0.774(6)
S3783	22.3(2)	3.34(2)	1.31(2)	0.262(7)	2.81(4)	0.29(1)	8.010	0.350(4)	0.71(5)
S3657	19.9(3)	3.38(2)	1.01(5)	0.44(1)	2.62(5)	0.64(2)	8.108	0.545(3)	0.88(1)
S3655	19.9(5)	3.36(5)	1.25(7)	0.39(3)	2.40(6)	0.62(4)	8.018		
S3655	19.9(5)	3.42(1)	1.04(3)	0.24(3)	2.77(9)	0.58(2)	8.060		
S3460	18.5(5)	3.502(7)	1.06(2)	0.049(4)	2.22(6)	1.12(3)	7.970		
S3470	18.8(5)	3.44(2)	1.09(1)	0.03(7)	2.37(3)	1.05(2)	8.006		
S3478	23(5)	3.30(2)	1.33(3)	0.25(1)	2.89(6)	0.24(2)	8.028		
S3480	22.1(5)	3.47(5)	1.16(7)	0.27(2)	2.67(4)	0.37(3)	7.950	0.380(5)	
S3484	22.3(5)	3.33(3)	1.34(2)	0.20(6)	2.93(3)	0.188(7)	8.000	0.36(2)	
S3498	21.4(5)	3.33(5)	1.28(9)	0.276(8)	2.80(6)	0.34(3)	8.031	0.28(2)	
Peridotite									
S3551	20.4(3)	3.54(4)	0.87(8)	0.26(3)	2.9(1)	0.44(8)	8.022	0.496(2)	0.88(2)
S3550	19.2(3)	3.62(2)	0.70(3)	0.22(8)	2.58(3)	0.92(3)	8.030	0.626(3)	0.937641
S3549	19.9(2)	3.58(1)	0.76(2)	0.11(4)	3.04(2)	0.54(2)	8.033	0.542(3)	0.87(3)
S3548	19.5(2)	3.61(1)	0.68(3)	0.23(2)	2.93(4)	0.59(3)8	8.051	0.605(5)	0.863(4)
S3547	19.5(5)	3.57(2)	0.77(3)	0.167(8)	2.88(5)	0.63(2)	8.037	0.592(2)	0.844(6)
S3764	21.2(3)	3.60(3)	0.80(2)	0.28(3)	3.02(2)	0.283(1)	8.000	0.426(5)	0.73(1)
S3757	20.7(5)	3.65(1)	0.69(1)	0.24(5)	3.082(4)	0.322(1)	7.998	0.469(2)	0.774(6)
S3784	23.5(4)	3.60(2)	0.68(9)	0.31(4)	3.4(1)	0.054(1)	8.061	0.545(3)	0.88(1)
S3460	18.5(5)	3.67(4)	0.63(3)	0.10(2)	2.79(7)	0.81(5)	8.010		
S3470	18.8(5)	3.664(3)	0.683(5)	0.05(2)	2.75(3)	0.84(3)	7.994		
S3475	22.6(5)	3.62(2)	0.791(2)	0.28(1)	3.21(5)	0.08(2)	7.984		
Majorite									
S3460	18.5(5)	3.78(4)	0.47(2)	0.098(9)	2.97(6)	0.65(4)	7.979		
S3470	18.8(5)	3.77(1)	0.49(1)	0.034(5)	2.87(7)	0.81(3)	7.985		
Reversals									
S3784	23.5(4)	3.15(1)	1.68(3)	0.26(2)	2.59(6	0.30(4)	8.000	0.545(3)	0.88(1)
S3538	17.9(5)	3.24(5)	1.36(5)	0.05(2)	2.82(7)	0.57(6)	8.067		
S3543	18.4(5)	3.14(6)	1.57(6)	0.16(3)	2.63(4)	0.55(5)	8.069		
S3515	19.8(5)	3.41(2)	1.08(2)	0.22(7)	2.42(3)	1.01(4)	8.042		
S3521	20.7(5)	3.55(4)	0.87(4)	0.33(2)	2.77(6)	0.48(4)	8.008		
S3523	20.8(5)	3.40(2)	1.18(3)	0.23(1)	2.53(2)	0.63(2)	8.015	0.464(3)	
1400°C									
Pyrope									
S3611	18.1(5)	3.17(3)	1.61(7)	0.144(7)	2.01(3)	1.08(5)	8.023		
S3614	18.6(5)	3.15(3)	1.56(5)	0.197(6)	2.09(6)	1.055(5)	8.064		
H2370	19.5(5)	3.10(6)	1.75(9)	0.236(5)	2.35(5)	0.58(4)	8.020	0.60(1)	0.93(1)
H2375	17.9(5)	3.24(1)	1.46(4)	0.200(5)	2.00(3)	1.11(3)	8.025		
H2241	19.6(5)	3.12(4)	1.76(6)	0.19(1)	2.41(5)	0.51(3)	7.996		
Basalt									
S3611	18.1(5)	3.301(8)	1.31(2)	0.199(4)	2.12(2)	1.11(2)	8.044		
S3614	18.6(5)	3.33(2)	1.17(4)	0.223(7)	2.49(2)	0.86(2)	8.080		
H2375	17.9(5)	3.40(3)	1.13(7)	0.223(8)	2.22(6)	1.04(3)	8.028		
Peridotite									
S3614	18.6(5)	3.56(1)	0.69(2)	0.263(7)	2.91(4)	0.66(4)	8.090		
S3611	18.1(5)	3.60(3)	0.71(5)	0.26(5)	2.68(4)	0.78(4)	8.042		

The Ca contents of garnet in equilibrium with Ca-perovskite at 1600°C and at 1400°C are shown in Fig. 2.10 (A) and (B). Data for all the reversal experiments at 1600°C are shown in Fig. 2.10(A). It was observed from the experimental data at 1600°C that the solubility of the Ca in garnet in equilibrium with calcium perovskite decreases with pressure. However, the Ca solubility increases with the garnet majorite content (i.e., Al/Si ratio) at a given pressure. This implies that the CaO saturation or the initiation of $CaSiO_3$ exsolution will occur at a higher CaO content with decreasing majorite component in majorite garnet at transition zone pressure-temperature conditions. Low Al/Si ratios of about 0.7 are representative of garnets formed in peridotitic bulk compositions, while higher values of about 1.4 are those for garnets formed in a basaltic composition.

Experimental data at 1400°C also showed a similar Ca solubility trend in garnet, i.e., CaO solubility in the majorite garnet composition decreases with increasing majorite component Al/Si+Mg. However, there is a small but distinguishable decrease in the Ca solubility compared with results obtained at 1600°C.

As Fe is also an important component in transition zone phases we carried out a few experiments to observe the effect of varying Fe concentration on the CaO solubility in the garnets in equilibrium with calcium perovskite. For this we mixed our fluxed starting compositions with a powder of 5-mol% Forsterite 80 composition, which is a relevant composition for the mantle depth at which this reaction takes place. We placed one iron-bearing sample along with a normal starting composition in a single run using the multi-chambered capsule. On analysis of the experimental run products no significant change in the CaO solubility was observed compared with that of the starting samples without additional mixing of Fe.

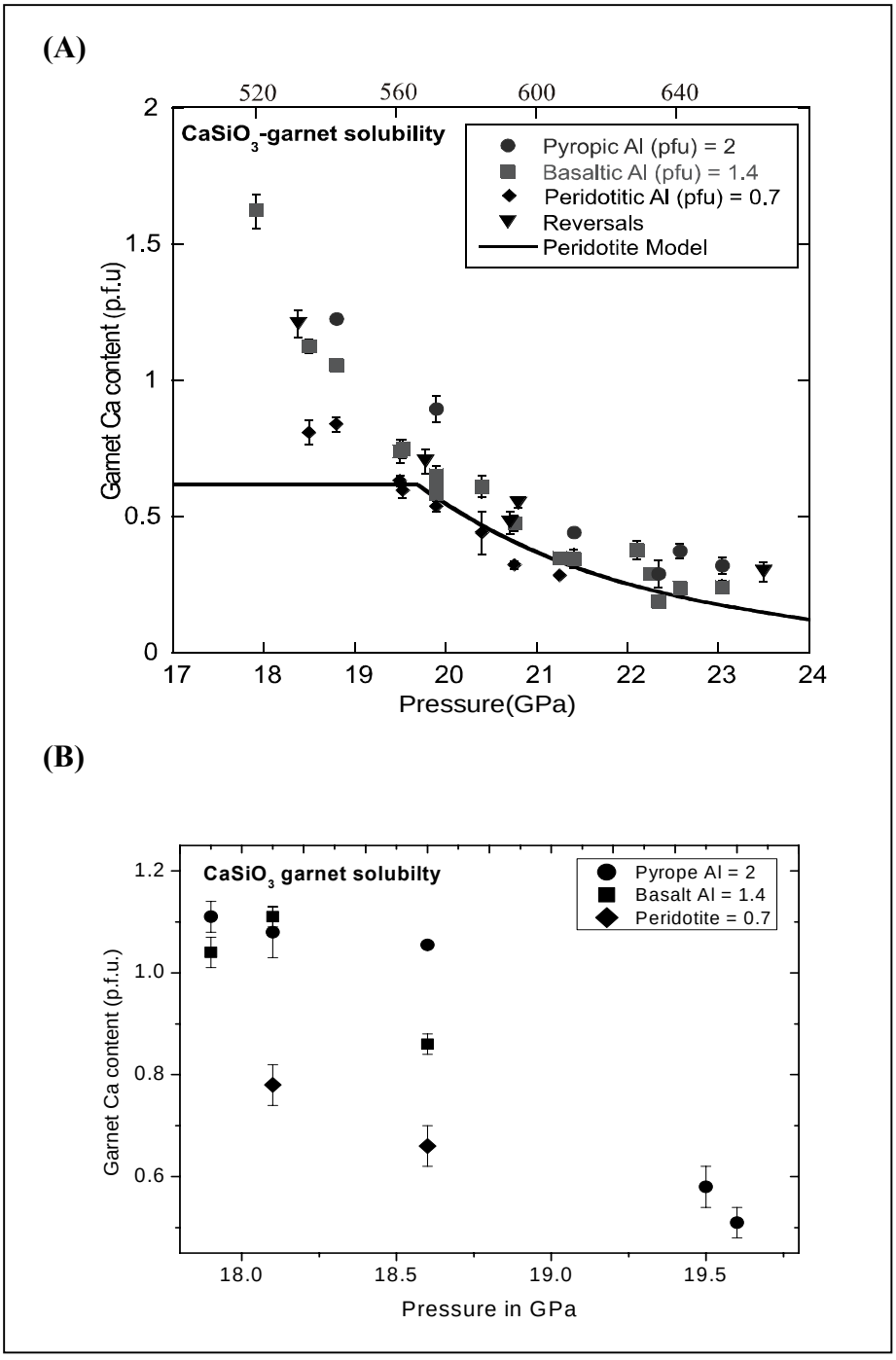

Figure 2.10. Experimental results for the Ca-content of garnet in equilibrium with Ca-perovskite as a function of pressure **(A)** at 1600°C and **(B)** at 1400°C. Symbols refer to starting compositions with different garnet majorite proportions named after the rock types in which the garnets would occur. Al (pfu) refers to the Al content per garnet formula unit, i.e. Al (pfu) = 2 refers to the formula $(Mg,Fe)_3Al_2SiO_{12}$. These Al contents only reflect the starting material because the Al content is lowered during the experiments. Reversals were performed using presynthesised Ca-bearing garnets as starting materials. The curve in **(A)** shows the calculated Ca content of garnet for a rock of peridotite composition based on peridotite composition from McDonough and Sun, (1995). For discussion on the peridotite model see section 2.5.

2.4.1 Thermodynamic modeling

The exsolution of calcium silicate perovskite from majorite garnet can be described by the following reaction

$$Ca_3Al_2Si_3O_{12}+3/4(Mg,Fe)_4Si_4O_{12} = 3\ CaSiO_3 + (Mg,Fe)_3Al_2Si_3O_{12} \quad [1]$$

Garnet Garnet Perovskite Garnet

where, the grossular component in the garnet exsolves to form calcium silicate perovskite, which leaves the garnet increasingly aluminium rich and combined with the majorite component, produces pyrope.

The experimental results were fitted to a thermodynamic model based on reaction [1]. The important variables in this fit are the volume change of the reaction and the non-ideal mixing parameters for majoritic garnet. Because the data cover a range of garnet-majorite compositions, this model was used to calculate the exsolution of $CaSiO_3$ over a range of bulk compositions relevant for the mantle. This also allowed our results to be extrapolated to lower temperatures at which slow kinetics inhibited the achievement of equilibrium in experiments.

At equilibrium conditions the standard state free energy change $\Delta G^0_{P,T}$ for reaction [1] is related to the activities of the reacting components by the equation,

$$\Delta G^0_{P,T} = -RT\ \ln K = -RT\ \ln \left[a^{Gt}_{Mg_3Al_2Si_3O_{12}}\right] \Big/ \left[a^{Gt}_{Ca_3Al_2Si_3O_{12}}\right]\left[a^{Gt}_{Mg_4Si_4O_{12}}\right]^{\frac{3}{4}} \quad [2]$$

where R is the gas constant, K is the equilibrium constant and a_i^{Gt} is the activity of component i in garnet. In order to estimate activities it was assumed that Ca mixes only on the dodecahedral site in garnet and that Fe behaves identically to Mg. The activity of $CaSiO_3$ is unity whereas the activities of the garnet components are described by

$$a^{Gt}_{Mg_4Si_4O_{12}} = \gamma^{Gt}_{Mg_4Si_4O_{12}} \left(X^{oct}_{Maj}\right)\left(X^{dodec}_{Mg}\right)^3 \quad [3]$$

$$a^{Gt}_{Ca_3Al_2Si_3O_{12}} = \gamma^{Gt}_{Ca_3Al_2Si_3O_{12}} \left(1 - X^{oct}_{Maj}\right)\left(X^{dodec}_{Ca}\right)^3 \quad [4]$$

$$a^{Gt}_{Mg_3Al_2Si_3O_{12}} = \gamma^{Gt}_{Mg_3Al_2Si_3O_{12}} \left(1 - X^{oct}_{Maj}\right)\left(X^{dodec}_{Mg}\right)^3 \quad [5]$$

$$\text{where, } X^{oct}_{Maj} = \left(\frac{2 - nAl}{2}\right) \quad [6]$$

$$X_{Mg}^{dodec} = \left(\frac{3 - nCa - nFe}{3}\right) \quad [7]$$

$$X_{Ca}^{dodec} = \left(\frac{nCa}{3}\right) \quad [8]$$

nAl, *nCa* and *nFe* are element proportions in garnet based on 12 oxygen formula units and γ is the activity coefficient. Si and Mg are therefore assumed to be locally ordered on the octahedral site.

The activity coefficients (γ) were first determined using a four-component symmetric solution model that include terms for the non-ideality of majorite mixing. However, all majorite terms, which were refined in the fitting, were very small and were therefore ignored. A ternary symmetric solution model was then used that accounted for non-ideality resulting from Mg, Ca and Fe mixing only on the dodecahedral site, i.e.,

$$RT \ln \gamma_{Mg_3Al_2Si_3O_{12}}^{Gt} = X_{Ca}^{2} W_{MgCa} + X_{Fe}^{2} W_{MgFe} + X_{Ca} X_{Fe} \left(W_{MgCa} + W_{MgFe} - W_{CaFe}\right) \quad [9]$$

$$RT \ln \gamma_{Ca_3Al_2Si_3O_{12}}^{Gt} = X_{Mg}^{2} W_{MgCa} + X_{Fe}^{2} W_{CaFe} + X_{Mg} X_{Fe} \left(W_{MgCa} + W_{CaFe} - W_{MgFe}\right) \quad [10]$$

where W are Margules interaction parameters. The following values were used based on published values (O'Neill and Wood, 1979; Frost, 2003b).

$$W_{MgFe} = 300 \text{ J/mol} \quad [11]$$

$$W_{CaFe} = 2000 \text{ J/mol} \quad [12]$$

Although many studies show the pyrope-grossular solid solution to have significant asymmetric excess enthalpy, entropy and volume properties, extrapolation of the many published models to pressures in excess of 20 GPa and 1873K yields wildly disparate activity coefficients. We therefore have no option but to treat W_{MgCa} as an adjustable parameter but the range of Ca contents covered by our data makes an asymmetric fit unconstrained and unnecessary for our purposes. Therefore, we refine symmetric terms for W_{MgCa} but constrain them to vary over a range predefined from literature values to get,

$$W_{MgCa} = 8000 + 300P \text{ J/mol} \quad [13]$$

where *P* is in GPa.

Fig. 2.11, shows the $RT\ln K$ calculated from the experimental data using the activity model. The data were fited in a least squares refinement to an equation for $\Delta G^0_{P,T}$ that gave,

$$\Delta G^0_{P,T} = -140763 + 26.773T - 12560P \text{ J/mol} \quad [14]$$

with T in K and P in GPa.

As $\Delta G^0_{P,T}$ is the standard Gibbs free energy change of the pure components at pressure and temperature, this can be simply described in terms of entropy, enthalpy and volume changes by,

$$\Delta G^0_{P,T} = \Delta H - T\Delta S + P\Delta V \quad [15]$$

We fit the calculated values for the $-RT\ln K$ term to equation [15] .The volume change of equation [1] is determined as 12.56 cm^3 mol^{-1} which is very reasonable given the volumes and equation of state properties of the phases involved

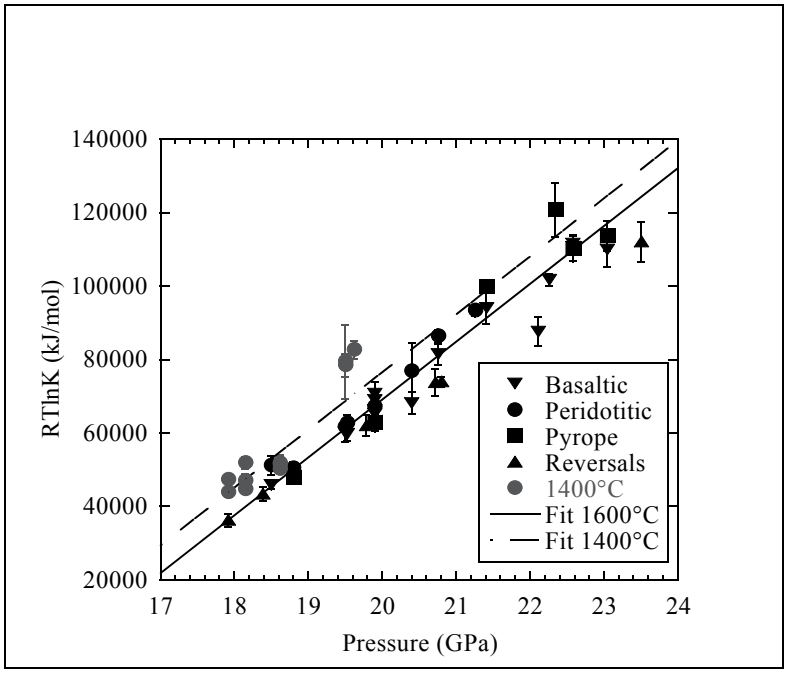

Figure. 2.11: A plot of $RT\ln K$ as defined in equation (2) as a function of pressure. Data from various starting compositions at 1600°C are indicated, while pyrope, basaltic and peridotitic compositions are plotted together at 1400°C. Fitted curves for $\Delta G^0_{P,T}$ described using equation (14) are shown at both temperatures.

2.5. Discussion

The garnet Ca content calculated for a fertile mantle peridotite composition based on the peridotite composition from McDonough and Sun, (1995) is shown by the solid curve in Fig. 2.10, along with the experimental results at 1600°C. Initially, as all the Ca is contained in the garnet, so the Ca content in garnet is constant with pressure. Above 19 GPa the garnet $CaSiO_3$ solubility limit is reached and the exsolution of $CaSiO_3$ begins quite sharply with increasing pressure, causing the garnet Ca content to decrease. However as $CaSiO_3$ exsolves, the residual garnet becomes more Al rich and thus the $CaSiO_3$ exsolution starts to level off. The exsolution reaction is therefore inherently non-linear with pressure.

We calculated the proportion of Ca-perovskite formed in a rock of peridotitic composition and also that in a rock of mid-oceanic ridge basalt (MORB) composition as shown in Fig. 2.12. As the calcium content of the MORB composition is higher than that of a peridotitic composition, the garnet in a MORB composition reaches saturation at lower pressures than in the peridotitic composition. The saturation point is affected by the MORB garnet having a higher Al content, which shifts the Ca saturation to higher pressures. As the exsolution reaction is inherently non-linear, the formation of Ca perovskite occurs over an extensive pressure interval and is complete only when the garnet itself transforms to magnesium silicate perovskite. Such non-linear transformations are however known to be capable of causing seismic discontinuities, because a significant amount of Ca perovskite is formed over an initial narrow pressure interval. Seismic waves would only be reflected off the initial gradient in sound velocity even though the entire reaction occurs over a depth interval of more than 60 km (Helffrich and Wood, 1996; Stixrude, 1997).

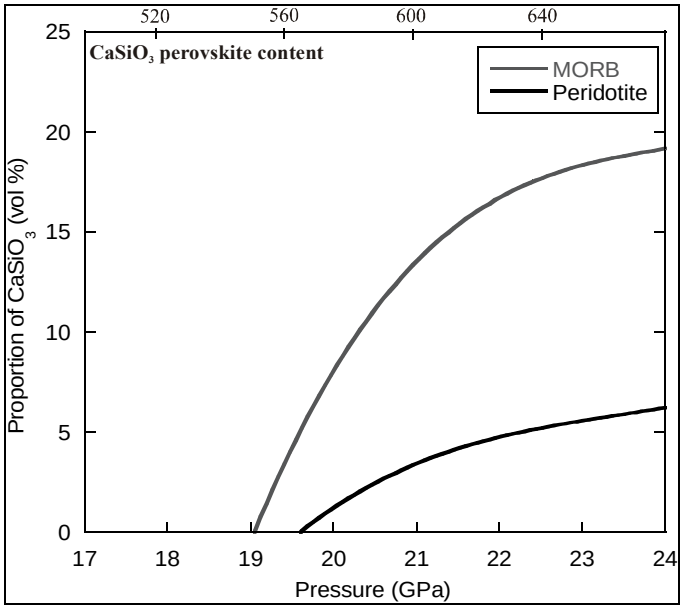

Figure. 2.12: The volumetric proportion of Ca perovskite that would form in rocks of peridotite and mid–oceanic ridge basalt composition as a function of pressure as calculated based on the thermodynamic model described in the text (see section 2.3.1).

For basaltic bulk compositions at certain conditions the exsolution of Ca-perovskite also involves a number of other phases, the stability fields of which are mutually influenced. As indicated by Eq. [1], as Ca-perovskite exolves with pressure, the garnet Al/Si ratio increases. For Al-rich lithologies such as basalts, the garnet Al content will reach that of the pyrope end member (i.e., 2 Al cations per formula unit) at pressures above 23 GPa. At these conditions the continued exsolution of Ca-perovskite from garnet requires the formation of an additional Al-rich phase. In this study the investigated garnet Al contents were always below 2 formula units and such a phase was not observed. In many previous studies the NAL phase (new aluminium rich phase) with the approximate formula $Na(Mg,Fe)_2Al_5SiO_{12}$ has been identified at these conditions (Hirose and Fei, 2002; Litasov and Ohtani, 2005) and, therefore, serves this purpose. This argument implies that the formation of the NAL phase is controlled by the garnet Al/Si ratio, as it should only form at pressures where garnet has obtained the pyrope stoichiometry as a result of Ca-perovskite exsolution. The presence of Na in NAL, however, may act to stabilize this phase in the presence of garnet with Al contents slightly below 2 formula units, as observed in some studies (Hirose and Fei, 2002; Litasov and Ohtani, 2005). At pressures higher than 25 GPa the NAL phase is reported to transform to a phase termed CF (calcium

ferrite structure), which has a composition approximately on the join $NaAlSiO_4$-$MgAl_2O_4$ (Hirose and Fei, 2002; Litasov and Ohtani, 2005).

Most oceanic basalt bulk compositions are more SiO_2-rich than compositions in the $MgSiO_3$-$CaSiO_3$-Al_2O_3 system and stishovite therefore coexists with garnet and Ca-perovskite at mid-transition zone conditions (Irifune, 1994; Litasov and Ohtani, 2005). At high temperatures (>1600°C) a phase termed CAS (calcium-alumino-silicate) with the approximate formula $CaAl_4Si_2O_{11}$ has been observed (Irifune, 1994; Hirose and Fei, 2002; Litasov and Ohtani, 2005) which can be understood to form through the reaction.

$$2Ca_3Al_2Si_3O_{12} + SiO_2 = CaAl_4Si_2O_{11} + 5CaSiO_3 \quad (11)$$

Garnet stishovite CAS perovskite

This reaction also contributes to the exsolution of $CaSiO_3$ perovskite from basaltic bulk compositions at temperatures above 1600°C (Litasov and Ohtani, 2005).

We have combined existing experimental results and mineral physics data (Sinogeikin and Bass, 2001; Sinogeikin *et al*., 2001; Li *et al*. 2006) to estimate the density and sound velocity changes for fertile peridotite and mid-oceanic ridge basalt compositions in the region of 520 km as shown in Fig. 2.13. The data employed were taken both from theoretical ab-initio calculations and also from experimental work for our calculations (Table 2.5). Volume at high-pressure and temperature were calculated using a third order Birch-Murnaghan equation of state and S-wave velocities were calculated following the procedure described in Akaogi *et al*., (2002). Although significant uncertainty remains in the extrapolation of mineral physical parameters to the pressures and temperatures of interest, recent ab-initio calculations (e.g., Li *et al*., 2006) have improved such estimates. The aim of this calculation is to illustrate the likely difference in velocity contrast expected for the wadsleyite-ringwoodite transformation and for the exsolution of Ca-perovskite and not to arrive at an accurate absolute velocity profile. With this defense and for the sake of simplicity the presence of stishovite has not been included in calculations for the MORB composition. The formation of NAL and CAS phases should be limited to high temperatures (>1600°C) and pressures (>23 GPa) respectively and will, therefore, not influence the curves shown in Fig. 2.13.

For fertile peridotite at 1400°C, the wadsleyite-ringwoodite transition produces a relatively strong discontinuity between 505-530 km, whereas the formation of Ca-perovskite creates a break in slope at approximately 540 km followed by a region with a higher velocity gradient which curves back towards the ambient transition zone gradient

over a depth of approximately 60 km. A similar situation occurs at 1600°C but because the Clapeyron slope of the wadsleyite-ringwoodite transition is steeper (0.005 GPa K^{-1}) than that of the Ca-perovskite reaction (0.002 GPa K^{-1}) the two discontinuities merge at approximately 560 km. Both discontinuities contribute to a generally steep gradient in seismic velocity in the lower part of the transition zone, which is a feature in common with seismic reference models (Dziewonski and Anderson, 1981).

Table 2.5. Elasticity data used for calculating density and S-wave velocity at high pressure and temperature. Wad (wadsleyite), Ring (ringwoodite), Perov (perovskite), V (molar volume) α_0, α_1, α_2 (thermal expansion coefficient and its derivatives related by the equation $\alpha(T) = \alpha_0+\alpha_1T+\alpha_2/T^2$), K_0 (bulk modulus), K' (pressure derivative of bulk modulus), G (shear modulus), G' (pressure derivative of shear modulus).
Sources: Mg_2SiO_4 Wad (Jackson and Rigden, 1996; Li *et al*., 1998;Cammarano *et al.,* 2003), Ring (Meng *et al.,* 1994; Matsuzaka *et al.,* 2000; Sinogeikin and Bass, 2002;Cammarano *et al.,* 2003); Fe_2SiO_4 Wad (Fei *et al*., 1991), Ring (Sato, 1977; Masuzaka *et al.*, 2000); $Mg_4Si_4O_{12}$ garnet (Akaogi *et al.,* 2002; Sinogeikin and Bass, 2001; Sinogeikin and Bass, 2002); $Mg_3Al_2Si_3O_{12}$ garnet (Sinogeikin and Bass, 2001; Sinogeikin and Bass, 2002; Akaogi *et al.,* 2002; Cammarano *et al.,* 2003); $Ca_3Al_2Si_3O_{12}$ garnet (Conrad *et al*., 1999; Sinogeikin and Bass, 2001; Sinogeikin and Bass, 2002; Akaogi *et al*., 2002; Cammarano *et al*., 2003;); $Fe_3Al_2Si_3O_{12}$ garnet (Skinner ,1966;Akaogi *et al*., 1998; Sinogeikin and Bass, 2002; Jiang *et al.*, 2004);$CaSiO_3$ perov (Li *et al*., 2006).

		V cm^3/ mol	**α_0 ($x10^5$)**	**α_1 ($x10^9$)**	**α_2**	**Ko (GPa)**	**K'**	**dK/dT ($GPaK^{-1}$)**	**G (GPa)**	**G'**	**dG/dT ($GPaK^{-1}$)**
Mg_2SiO_4	Wad	40.51	2.85	3.20	0	174	4	-0.019	121-28x_{Fe}	1.3	-0.017
Fe_2SiO_4	Wad	43.15	2.32	7.12	-0.243	166	4	-0.0215			
Mg_2SiO_4	Ring	39.48	2.448	4.056	-0.6029	182	4	-0.027	112-40x_{Fe}	1.5	-0.016
Fe_2SiO_4	Ring	41.86	2.455	3.59	-0.3703	197	4	-0.0284			
$Mg_4Si_4O_{12}$	Garnet	113.88	2.87	2.89	-0.5443	162	4.2	-0.02	85	1.4	-0.0092
$Mg_3Al_2Si_3O_{12}$	Garnet	113.19	2.87	2.89	-0.5443	169	4.2	-0.02	94	1.3	-0.0092
$Ca_3Al_2Si_3O_{12}$	Garnet	125.31	2.87	2.89	-0.5443	165	5.4	-0.02	107	1.3	-0.0092
$Fe_3Al_2Si_3O_{12}$	Garnet	115.44	1.78	1.21	-0.5071	176	5.5	-0.0277	95.6	1.4	-0.0092
$CaSiO_3$	Perov	27.45	3.22	6.88	0	236	4	-0.036	135	1.28	-0.01

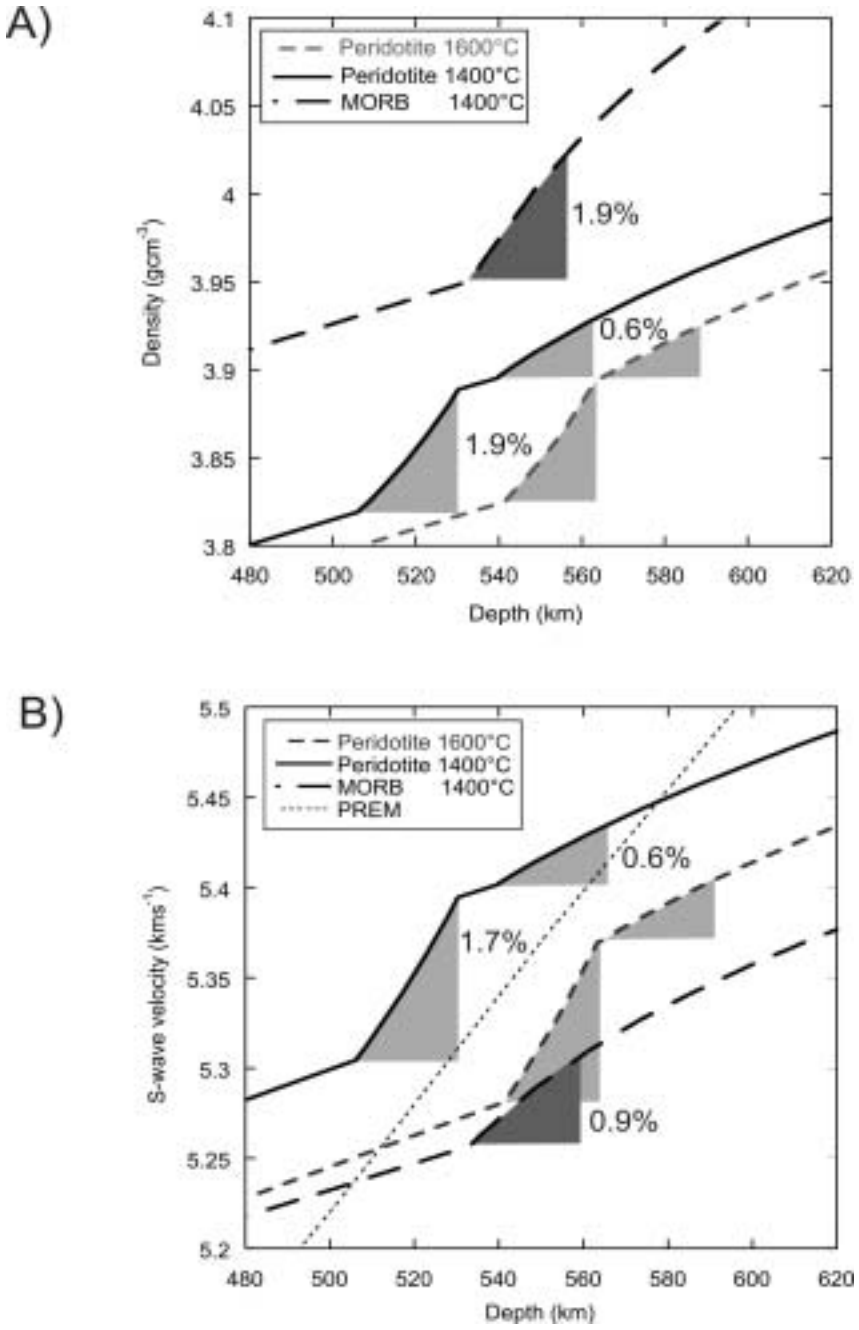

Figure. 2.13. (A) Density and **(B)** shear wave velocity calculated along isotherms for fertile peridotite composition and MORB compositions as a function of depth. The phase proportions are calculated using a thermodynamic model fit to the experimental data in addition to auxiliary thermodynamic data for the $(Mg,Fe)_2SiO_4$ β-γ phase transformation (Mastuzaka *et al*., 2000; Frost, 2003). For the peridotite composition, two shaded discontinuities can be observed resulting from the wadsleyite-ringwoodite (shallower) and the garnet-Ca-perovskite reaction. For the MORB composition only the Ca-perovskite reaction occurs. As the Ca-perovskite reaction is non-linear and its seismically observable depth interval is hard to assess, the shaded region is shown for the same depth interval as the β-γ transition for comparison. The percent density and S-wave velocity jumps resulting from both the β-γ and Ca-perovskite reactions are shown as calculated over the shaded regions. PREM S-wave velocities are also shown for comparison.

As the majority of observations of the 520 km discontinuity have been made with studies of long-period underside SS reflections (Shearer, 1990; Shearer, 1996; Deuss and Woodhouse, 2001), where the amplitude, i.e., the visibility of the reflected waves will depend on the S impedance contrast $\Delta(\rho V_s)$, where ρ is density and V_s is the shaer wave velocity. The wadsleyite-ringwoodite transition occurs over a depth interval of approximately 25 km with a $\Delta(\rho V_s)$ of 3.6 %. The seismically observable effective depth interval of the Ca-perovskite reaction is harder to determine and the reflectivity will vary with the frequency of seismic waves (Stixrude, 1997; Li *et al.*, 2006). However, we can make a simple comparison by calculating $\Delta(\rho V_s)$ over the same depth interval as the wadsleyite to ringwoodite transition which gives a value of 1.5 % for impedence contrast.. These impedance contrasts are in excellent agreement with those that have been proposed for the split 520 km discontinuities (Deuss and Woodhouse, 2001).

The regional variability in the appearance of a split and single 520 km discontinuity can be potentially explained by variations in mantle temperature. As a result of the effective Clapeyron slope of the wadsleyite-ringwoodite being steeper than that of the Ca-perovskite formatting reaction, the two transformations would merge to form an apparently single discontinuity at temperatures of approximately 1600°C. At lower temperatures (1400°C), on the other hand, two discontinuities would be observed. This may explain some of the observations but it is not completely consistent with the general behavior, which is that a discontinuity at approximately 520-530 km splits in some regions into a shallower (500 km) and a deeper (560 km) branch (Deuss and Woodhouse, 2001). If this were a result of temperature variation alone it would imply that the Clapeyron slope of the Ca-perovskite reaction is negative, whereas in fact both reactions have positive slopes (Fig 2.14). In addition, our results show that the two discontinuities would merge at a significantly greater depth (~560 km) than the ~520 km depth that is typically reported for a single discontinuity (Flanagan and Shearer, 1996).

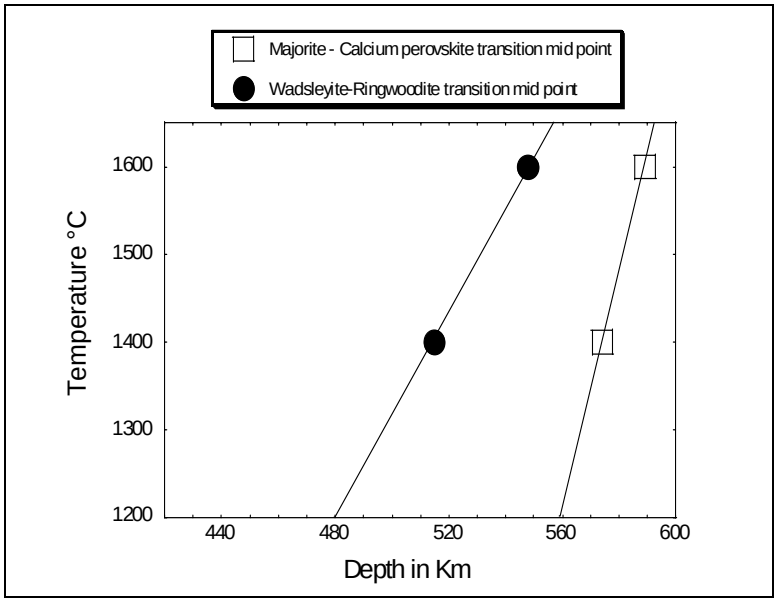

Figure. 2.14: Comparison of the transition pressure for wadsleyite-ringwoodite and majorite-Ca-perovskite as function of mantle temperatures of 1400°C and 1600°C showing positive Clapeyron slopes as represented by the solid lines for both the reaction**.** The closed circles are the transition mid points for wadsleyite-ringwoodite based on work of Frost, (2003) and the open squares are the transition mid points for the majorite to Ca-perovskite from the present experimental study.

A more consistent explanation is that in many regions where only a single 520 km discontinuity is observed the Ca-perovskite reaction is invisible because the Ca content of the mantle is too low i.e., the region has undergone partial melting at the surface at some point in its history and is depleted in a fertile component. A strong 560 reflection, on the other hand, would indicate the presence of fertile mantle or mantle that contains a significant component of recycled MORB crust. The impedance contrast for the Ca-perovskite reaction in MORB is 2.8 %. As no wadsleyite to ringwoodite transition occurs in MORB, mantle with an enriched recycled MORB component would have a weaker 510 discontinuity but a much stronger reflection at approximately 560 km, in line with some of the observations.

The 520 km discontinuity becomes uplifted to approximately 500 km as it splits, which based on the Clapeyron slope of the wadsleyite to ringwoodite transition implies local mantle temperatures that are cooler by at least 100°. As these regions also display a strong Ca-perovskite transition a good explanation for the splitting would be that it occurs in areas that contain significant amounts of subducted oceanic crust. If subducted slabs descend at high angle directly into the lower mantle these regions would not be expected to

be nearly as globally extensive as they appear to be. However, the widespread splitting of 520 would be easily explained if subducted material is accumulating at the base of the transition zone, as a result of either density or rheological contrast with the lower mantle (Christensen, 1997; Karason and van der Hilst, 2000), creating relatively cool flat-lying regions rich in oceanic crust.

2.6. Conclusions

Our experimental data support the hypothesis that the wadsleyite to ringwoodite transition and the Ca-perovskite forming reactions could produce two distinct discontinuities between 500 and 560 km. The presence and amplitude of a discontinuity at approximately 560 km will be sensitive to the Ca-content of the mantle and will consequently be an indicator for the presence of fertile mantle or mantle enriched in recycled oceanic crust. This is, therefore, the first mantle discontinuity to be identified that is sensitive to the main type of large-scale chemical heterogeneity expected in the Earth's mantle. The observed variability in 520 km seismic discontinuity splitting indicates that the mantle at this depth may be heterogeneous over quite extensive regions.

On considering the geographical distribution of the split 520 km seismic discontinuity, it is observed that Deuss and Woodhouse, (2001), in their seismological study reported the presence of a distinctly split 520 km seismic discontinuity from traces across North America, the East Pacific region, Indonesia and in the areas around the North African Shield. Like wise, Gilbert *et al*., (2003) also reported a split 520 km seismic discontinuity in areas beneath the Colorado Plateau, the Basin and Range province and the Rocky Mountains in the North Western United States. These regions are all undoubtedly sites of modern day or past subduction. Therefore, a correlation can be drawn supporting our idea of enrichment of Ca in the mantle by subduction of oceanic lithosphere beneath continental plates from the geographical distribution of the observed split 520 km seismic discontinuity. Further studies into the variability and splitting shown by the 520 km seismic discontinuity will provide key insights into the circulation of subducted crust and the lateral distribution of chemical heterogeneity in the transition zone.

Chapter 3

The compressibility of (Fe,Al)-bearing magnesium silicate perovskite determined by single-crystal X-ray diffraction: implications for lower mantle properties.

3.1 Introduction

The transformation of $(Mg,Fe)_2SiO_4$ ringwoodite to $(Mg,Fe)SiO_3$ perovskite and (Mg,Fe)O magnesiowüstite marks the beginning of the lower mantle. This transition is the likely cause of the 670 km seismic discontinuity (Ringwood and Major, 1967). At depths below 670 km, $(Mg,Fe)SiO_3$ perovskite becomes the dominant mantle constituent, accounting for approximately 80 volume percent of the Earth's lower mantle. Our understanding of the structure and temperature of the lower mantle is mainly based mainly on the comparison of seismic wave velocities with model calculations for wave velocities of mineral assemblages at lower mantle conditions. The reliability of such a comparison depends on the accuracy of experimental and theoretical estimates for mineral elastic properties at the conditions of the deep mantle. A complete knowledge of the elastic properties of $(Mg,Fe)SiO_3$ perovskite over the range of pressure, temperature and composition likely encompassed by the lower mantle is, therefore, a prerequisite for constraining the physical and chemical properties of the lower mantle. Because the lower mantle comprises the bulk of the silicate Earth, knowledge of its composition and temperature is vital to our understanding of the Earth's composition as a whole and mantle dynamics in general.

Perovskite-type compounds have ABX_3 stoichiometry and are characterised by a network of BX_6 corner-sharing octahedra. In the ideal perovskite structure the octahedral framework forms a cubic array and the A cations occupy the large 12-fold coordinated site.

This structure is cubic and has the space group $Pm\bar{3}m$. The majority of perovskite structures, however, including (Mg,Fe)SiO_3 perovskite, are distorted derivatives of the cubic structure. The most common type of distortion, as in the case of (Mg,Fe)SiO_3 perovskite, arises when the size of the A-cation is too small for the 12-fold site. To accommodate such cations the octahedra tilt about the pseudocubic axes, in this way the A-X bond-lengths are no longer all equal with a consequent change of the A-site coordination and reduction in symmetry from the cubic arystotype. Octahedral tilting in perovskite has been discussed in details by several authors (see for example Glazer, 1972, 1975; Megaw, 1973; Woodward 1997; Howard and Stokes, 1998). (Mg,Fe)SiO_3 perovskite has an orthorhombic symmetry (space group *Pbnm*) due to the tilting of the BO_6 framework which brings some oxygens closer to the A cations, resulting in a lowering of coordination of the A cations from [XII] to [VIII] fold (Fig. 3.1). The A site of (Mg,Fe)SiO_3 perovskite is mainly occupied by divalent Mg and Fe cations and the B site by Si. Divalent Fe substitutes for Mg up to approximately 25 % into the A site at conditions compatible with the top of the Earth's lower mantle, causing a slight expansion of the structure and a decrease in distortion (Ross and Hazen, 1989; Ross and Hazen, 1990; Hemley and Cohen, 1992).

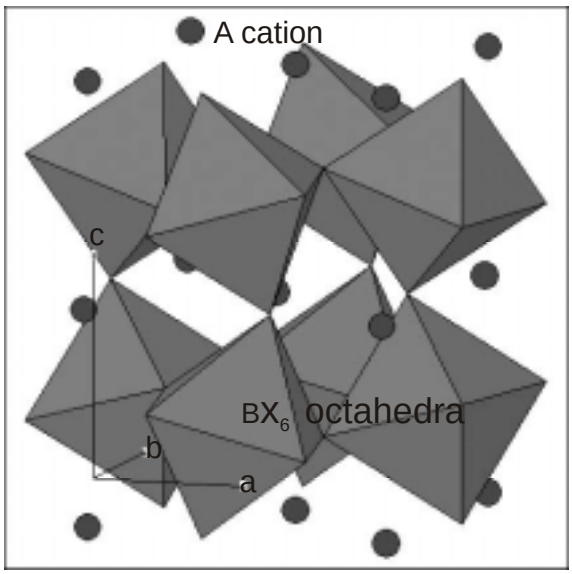

Figure. 3.1: Distorted orthorhombic $MgSiO_3$ perovskite structure, showing corner shared BX_6 octahedra with dodecahedral A cation site.

Octahedral tilt angles can be estimated using unit cell dimensions. For orthorhombic *Pbnm* perovskites, with no distortion of the BX_6 octahedra, three tilt angles can be defined (following the notation of Zhao *et al*., 1993a,b). These angles, θ, ϕ, and Φ represent rotations of the octahedra about the pseudo-cubic axes [110], [001] and [111] respectively and can be calculated according to the following equations:

$$\cos\theta = a/b \quad (1)$$

$$\cos\phi = \sqrt{2}a/c \quad (2)$$

$$\cos\Phi = \sqrt{2}a^2/bc \quad (3)$$

Although the unit cell dimension method normally underestimates the tilt angles, as real octahedra are typically slightly distorted, it is still very useful when the atomic coordinates of orthorhombic perovskites are not known.

Trivalent cations also substitute into $(Mg,Fe)SiO_3$ perovskite although the substitution mechanism may vary depending on the cation and on pressure and temperature. There is evidence, for example, that Al enters the structure through a coupled substitution onto both A and B sites (Stebbins *et al*., 2001). Other workers, however, have raised the possibility that Al may replace Si on the octahedral B site with charge balance provided by the creation of an oxygen vacancy (Navrosky, 1999). Certainly at pressures >30 GPa a coupled substitution seems to occur with up to 25 % substitution of an $AlAlO_3$ component being possible (Walter *et a.,* 2004). Al substitution causes the octahedral distortion to increase (Hemley and Cohen, 1993).

It was recently established experimentally that a significant portion of Fe in Al-bearing $(Mg,Fe)SiO_3$ perovskite is in the ferric (Fe^{3+}) state (McCammon, 1997). Support that this may also be the case in the lower mantle comes from the analyses of high ferric Fe contents in mineral inclusions trapped in diamonds that appear to have originally had the perovskite structure (Harte *et al.,* 1999). Experimental studies have also shown that the $Fe^{3+}/\sum Fe$ ratio in magnesium silicate perovskite is strongly correlated with Al content (Wood and Rubie, 1996; McCammon, 1997; Frost and Langenhorst, 2002; Lauterbach *et al*., 2000; McCammon *et al*., 2004). Such a strong coupling would imply that a coupled substitution takes place. Richmond and Brodholt, (1998) performed computer simulations to examine the energy associated with various trivalent cation substitution mechanisms i.e.,

$$Si^{4+}[VI] + Mg^{2+}[VIII] \leftrightarrow Al^{3+}[VI] + Fe^{3+}[VIII] \quad (4)$$

$$2Si^{4+}[VI] + O^{2-} \leftrightarrow 2Fe^{3+}[VI] + V_0 \quad (5)$$

$$2Si^{4+}[VI] + O^{2-} \leftrightarrow 2Al^{3+}[VI] + V_0 \quad (6)$$

These authors reported that the coupled substitution mechanism (4), where Al substitutions onto the Si site and Fe^{3+} onto the Mg site, is more energetically favourable than the oxygen vacancy mechanisms (5) and (6).

The incorporation of Al and the resulting stabilization of Fe^{3+} in the perovskite structure can potentially affect its elastic properties (Navrotsky *et al*., 2003). A number of observations of seismic anomalies in the lower mantle have been attributed to chemical heterogeneity (Trampert, 2004) and there are a number of possibilities as to how Al and Fe concentrations could vary in the lower mantle. In order to understanding the origin of seismic anomalies in the lower mantle a complete understanding of how cation substitutions influence the elastic properties of $(Mg,Fe,)SiO_3$ perovskite is required.

Values for the bulk modulus of end member $MgSiO_3$ perovskite determined using static compression and dynamic techniques such as Brillouin scattering, cover a range of 250-265 GPa with K' normally fixed at 4 (Andrault *et al.,* 2001; Daniel *et al*., 2001; Walter *et al.,* 2004; Yagi *et al*., 2004; Walter *et al*., 2006). Studies of $(Mg,Fe,)SiO_3$ perovskite indicate values in a similar range (Knittle and Jeanloz, 1987; Mao *et al.*, 1991).Studies on the effect of Al substitution on the elastic propoerties of $MgSiO_3$ perovskite, however, are far more inconclusive. A number of studies have shown that Al substitution causes a decrease in the bulk modulus of perovskite (Zhang and Weidner, 1999; Kubo *et al.*, 2000; Daniel *et al*., 2001; Yagi *et al*., 2004). Some studies indicate an increase in the bulk modulus (Andrault *et al*. 2001; Ono *et al*., 2004), while several others indicate that there is no change in the bulk modulus with Al incorporation (Yagi *et al*., 2004; Jackson *et al*., 2004; Li *et al*., 2005). This discrepancy observed in elastic property behaviour might be attributed to different substitution mechanisms operating over different pressure or Al concentration ranges. On the other hand it may result from partial amorphisation following sample synthesis or from the use of different measurement techniques. Aside from the discrepancies in these previous studies it is likely that in the Earth the presence of Fe^{3+} together with Al will affect quite differently the behaviour of perovskite in comparison

with Fe-free samples. To date there are no studies that have specifically examined the effect of varying perovskite Fe^{3+} content and bulk iron concentration on the elastic properties of Al-bearing (Mg,Fe,)SiO_3 perovskite.

In this study single-crystal X-ray diffraction experiments have been performed at room temperature in a diamond anvil cell (DAC) to determine the equation of state parameters of well-characterized samples of Fe and Al-bearing perovskite, with different Fe^{3+} contents.

3.2 Experimental details

3.2.1 Starting materials

Three starting compositions were employed for the synthesis of perovskite single crystals in this study (Table 3.1). The alumina contents of these compositions were fixed to a value of 5 wt %, considered to be typical for perovskite in the lower mantle, while the bulk Fe concentration was varied.

Table 3.1 The glass starting compositions in wt % oxide and cation proportion used for Fe and Al-bearing perovskite synthesis. Cation proportions are calculated based on 3 oxygens per formula unit.

No.	SiO_2	MgO	FeO	Al_2O_3	Total	Si	Mg	Fe	Al	Total	X Fe
1	54.58	36.64	3.63	5.15	100	0.929	0.935	0.052	0.103	2.019	0.05
2	52.96	35.13	6.76	5.17	100.02	0.916	0.911	0.097	0.105	2.031	0.1
3	52.8	32.07	10.09	5.1	100.06	0.925	0.843	0.147	0.1052	2.021	0.15

Starting powders of high-purity SiO_2, MgO, Al_2O_3 and Fe_2O_3 were ground together in the proportions indicated in Table 3.1, then placed in a Pt crucible and fused in air at 1600°C for 15 minutes. The crucible was than rapidly quenched in water to produce a silicate glass. The glass was ground to a powder, then pelletised and reduced in a CO_2-H_2 gas-mixing furnace maintained at an fO_2 of approximately 2 log units above the iron-wüstite buffer at 650°C for 24 hours. The low temperatures prevented the glass from crystallizing. Compositional characterization of the glasses was performed using an electron microprobe. The analysis conditions were the same as listed in Chapter 2 section

2.3. Mössbauer analysis on the glass powders confirmed the complete reduction of Fe_2O_3 to FeO.

3.2.2 Multianvil synthesis experiments

The glasses were transformed to perovskite using a multi-anvil press at 25 GPa and 1800-2000°C. Multi-anvil experiments were performed using a pressure medium of Cr_2O_3 doped MgO octahedra of 8 mm edge length in combination with tungsten carbide cubes with 3 mm truncation edge lengths. The pressure assembly employed in this study is as shown in Fig. 3.2. The reduced glass powders were packed into Re or Au gold foil capsules of 2 mm length and 1 mm diameter. The heating duration of the experiments was varied from an hour to ten minutes and experiments were quenched by cutting the power supply. No thermocouple was employed in the experiments but instead a previous calibration of temperature versus power was used to provide an estimate of the temperature. It has been found that in many experiments where a thermocouple was employed, it has led to leakage of partial melt from the capsule and failure of the experiment due to damage caused by compaction of the capsule by the hard Al_2O_3 thermocouple sleeve. The presence of small degree partial melts is key to the growth of large single crystals. In experiment H2369, melting occurred due to the high temperatures and high Fe content, while in run H2438, H_2O was added to flux melting (See Appendix B Table B.1 for run details).

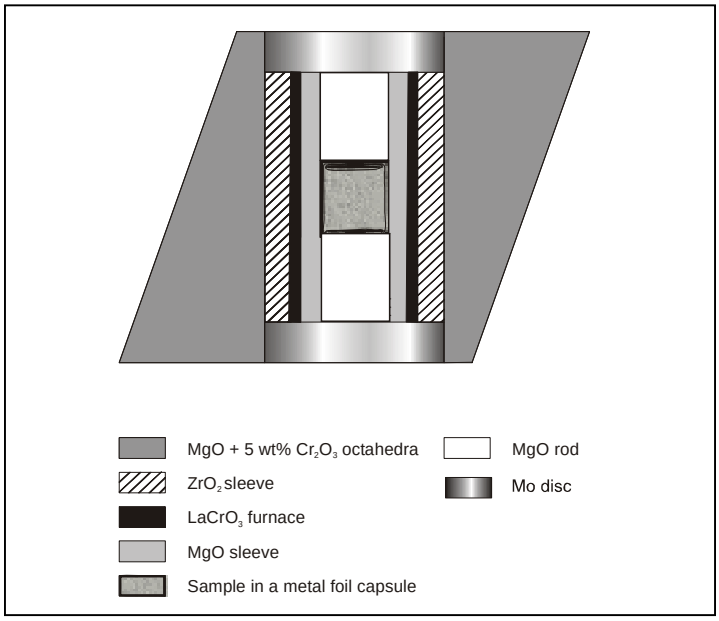

Figure 3.2: The 8/3 multianvil pressure assembly used for multianvil synthesis experiments (not to scale) as described in the text.

For the crystals of the compositions with X_{Fe} = 0.10 (**Crystal 1, Run no. H2369)** and 0.15 (**Crystal 2, Run no. H2438**) we recovered single crystals of size up to a maximum of 150 microns in length on decompression of the experiment as shown in Fig. 3.3 (A) and (B). As H_2O was used as flux in the synthesis of Crystal 1, FTIR (Fourier transform infra red) spectroscopic measurements were carried out on these perovskite crystals to check for the presence of water. No evidence for the incorporation of OH^- in the perovskite sample was detected, in accordance with previous measurements (Bolfan-Casanova *et al.,* 2000).

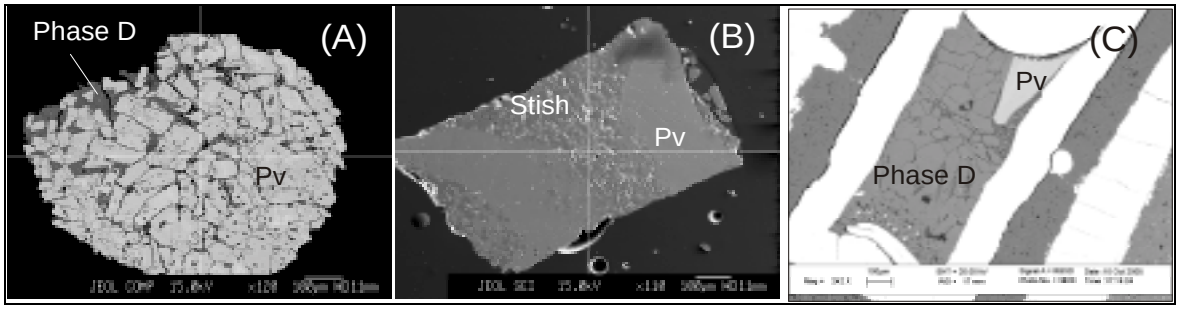

Figure. 3.3 Back-scattered and secondary electron image of the three crystals used for this diamond anvil cell compression study: (A) Perovskite (Crystal 1) coexisting with Phase-D; (B) Perovskite (Crystal 2) coexisting with stishovite and (C) A single crystal of perovskite (Crystal 3) coexisting with Phase D.

A number of attempts were made to synthesis large perovskite crystals using bulk composition No. 1 (X_{Fe} = 0.05) in Table 3.1. Although a number of perovskite samples were synthesised e.g., **Crystal 4**, the size and quality of all crystals were unsuitable for single crystal X-ray diffraction analysis in the diamond anvil cell (see Appendix B Table B.1). In most cases this composition produced only tiny crystal aggregates (< 20 μm). H_2O was employed as a flux in a number of such experiments, but had little effect. Experimental temperatures were varied between 1500-2000°C; at higher temperatures, however, the furnace of the experiment would become unstable possibly due to interaction with H_2 lost from the H_2O-bearing sample. The duration of the experiments was also varied from 10 minutes to more than hour to allow time for crystal growth. In some experiments temperatures were initially raised to ensure significant melting of the sample and then cooled over a duration of half an hour to promote growth of a small number of nucleated crystals. From such experiments several crystals of approximately 80 to 90 microns in length were recovered. However, they presented only weak and broad reflection profiles when analysed by X-ray diffraction and were, therefore, inadequate for DAC experiments. It was, however, possible to characterize the iron content of these crystals by Mössbauer spectroscopy and analyze their composition by electron microprobe.

The perovskite **Crystal 3** (Fig. 3.3, (C) upper right corner in grey) was produced in another study performed to synthesize hydrous Phase D (Frost, 2006). The starting composition was an oxide mixture of $Mg(OH)_2$, $Al(OH)_3$, Fe_2O_3 and SiO_2 in the stoichiometric proportion required for the Phase D $\{(Mg,Fe)(Si,Al)_2O_6H_2\}$ composition. A 7/3 multi-anvil pressure assembly was used for the experiment with a Pt capsule. The experiment was perfromed at 25 GPa and 1100°C for 2 hours. The run product contained a

single perovskite crystal of approximately 250 microns in length and smaller crystals of Phase D.

Recovered sample capsules were cut open using a razor blade and the crystal assemblage was examined under a binocular microscope in order to identify crystals of a suitable size. Once appropriate crystals were identified and separated, half of the remaining sample was embedded in epoxy for compositional analysis. The compositions of the crystals (Table 3.2) were determined by electron microprobe analysis with conditions and standards as reported in Chapter 2 (section 2.3).

Table 3.2 The cation proportion of perovskite crystal compositions as determined using EPMA based on 3 oxygen per formula unit. The $Fe^{3+}/\Sigma Fe$ ratios were determined by Mössbauer spectroscopy and Electron energy loss spectroscopy measurements (see section 3.2.3).

Crystal	Mg	Fe	Al	Si	Total	$Fe^{3+}/\Sigma Fe$
1	0.968	0.074	0.045	0.936	2.024	0.48
2	0.872	0.131	0.113	0.892	2.007	0.68
3	0.758	0.233	0.162	0.836	1.989	0.8
4	0.925	0.040	0.096	0.926	2.014	0.58

3.2.3 Quantification of perovskite $Fe^{3+}/\sum Fe$ ratios

Mössbauer spectroscopy

After microprobe analysis the perovskite crystal aggregates representative of **Crystals 1, 2 and 4** were analyzed by Mössbauer spectroscopy to determine the $Fe^{3+}/\sum Fe$ ratios using the milliprobe technique. This technique allows spectra to be collected from spot sizes of the order of 100 μm (McCammon, 1998). The epoxy resin mounts containing the samples were thinned down into disks with a thickness of 150 μm, which corresponds to an absorber thickness of ~5mg Fe/cm^2. The perovskite aggregates were masked with a Ta foil of 25 μm thickness with a 500 μm hole.

Mössbauer spectra were collected at room temperature over one to three days duration in transmission mode on a constant acceleration Mössbauer spectrometer using a nominal 370 -MBq ^{57}Co high specific activity source in a 12 μm Rh matrix point source. The velocity scale calibration was performed relative to 25 μm α-Fe foil using the positions certified by the National Bureau of Standards standard reference material

no.1541. The commercially available fitting program NORMOS written by R.A. Brand (distributed by Wissenschaftliche Elektronik GmbH, Germany) was used to fit the collected spectra to Lorentzian lineshapes. The values for $Fe^{3+}/\sum Fe$ were calculated based on relative area ratios corrected for thickness effects and differences in the recoil free fraction. The fitted spectrum for Crystal 2 is shown in Fig. 3.4.

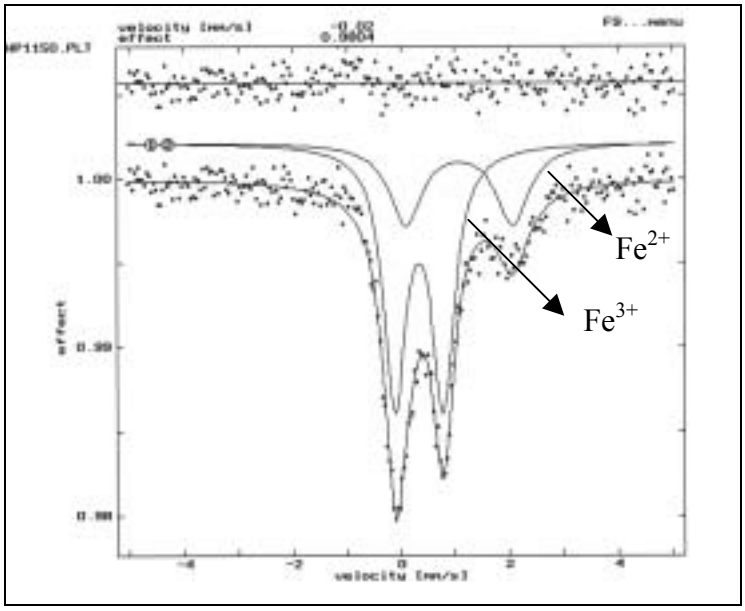

Figure.3.4: Mössbauer spectra showing relative intensity ratios of Fe^{3+} and Fe^{2+} in crystal 2.The doublet near the 1 mm/sec (1) is the one for Fe^{3+} and the other doublet is for Fe^{2}+. $Fe^{3+}/\sum Fe$ is determined based on the relative areas of Fe^{3+} doublet.

Transmission electron microscopy

A chip of **Crystal 3** was examined using a transmission electron microscope (TEM) principally to determine the $Fe^{3+}/\sum Fe$ ratio using electron energy loss spectroscopy (EELS). The crystal chip was mounted on a glass slide using dissolvable glue and polished down to a thickness of 13μm. After dissolving the glue, the crystal was then picked from the glass slide using a needle and placed on a Mo mesh (Fig. 3.5 A). Thinning of the sample was performed using an Ar^{+} ion beam in a Gatan dual ion mill model 600, at an angle of 13° with a 4 kV acceleration voltage and 1 mA beam current. At the end of thinning process the acceleration voltage was reduced to 3.5 kV and incidence angle to 11°

to reduce beam damage. The sample was cooled throughout this process using liquid nitrogen, in order to avoid beam damage. Thirty hours were required to thin the sample to electron transparency, with a thickness of approximately 10 nm (Fig. 3.5 C). The sample was than coated with 5 nm of amorphous carbon to prevent charging on the surface using a BAL-TEC, ME020 coating system.

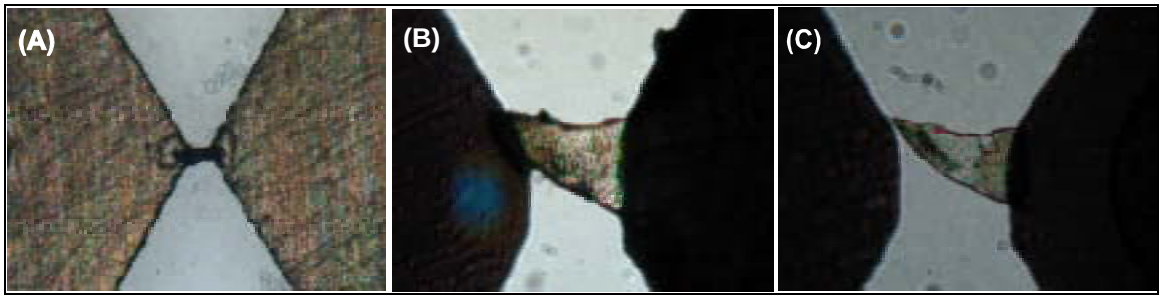

Figure. 3.5: Optical microscope images of crystal 3 during Ar ion thinning on a Mo mesh: (A) Crystal before Ar thinning (B) during Ar thinning and (C) after Ar thinning.

TEM imaging and EELS measurements were performed using a Philips CM-20FEG analytical transmission electron microscope operating at 200 kV, equipped with a parallel electron energy loss spectrometer (PEELS Gatan 666) and an energy dispersive x-ray spectrometer (NORAN Vantage EDX system). A stationary unfocussed beam of 5 nm spot size was used for EDX and EELS. To reduce beam damage during irradiation the sample was cooled to liquid nitrogen temperatures using a Gatan cooling stage. ELNES (electron energy-loss near-edge structure) spectra of the Fe $L_{2,3}$ edge were collected in diffraction mode with convergence and collection semi-angles of α = 8 mrad and β = 2.7 mrad and an energy dispersion of 0.1ev per channel. A typical Fe-$L_{2,3}$-edge ELNES spectra of Crystal 3 is shown in Fig. 3.6. The width of the zero loss peak at half height was ca. 0.8 eV. Quantification of the spectra was performed following the method of van Aken *et al*., (1998) using an empirically calibrated universal curve. EDXS spectra were collected with 100 sec live times and were quantified according to the procedure of van Cappellen and Doukhan (1994).

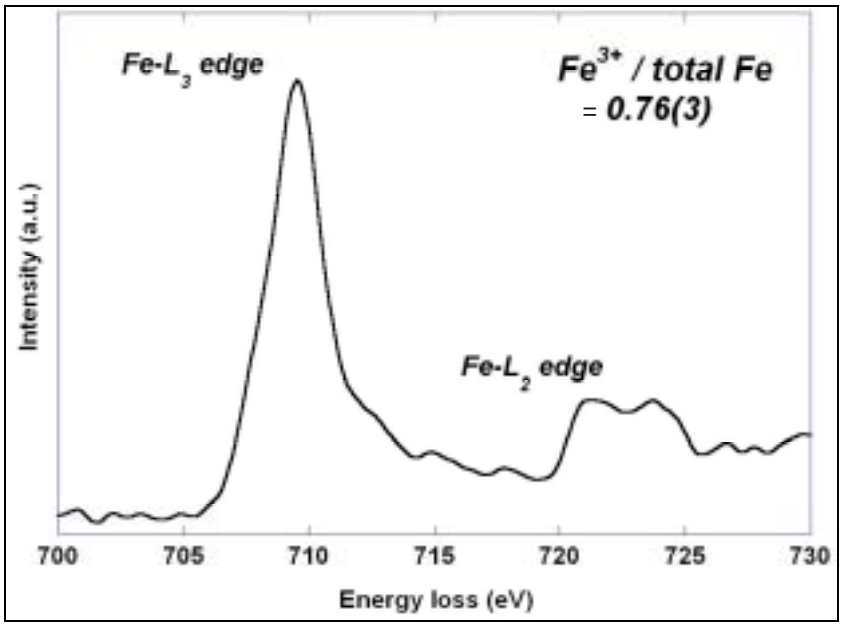

Figure. 3.6: A typical Fe-L $_{2,3}$-edge ELNES of Crystal 3. The spectrum has been gain normalized, background subtracted and deconvoluted using the low-loss spectra. The $Fe^{3+}/\sum Fe$ ratio was determined using the technique described by van Aken *et al.,* (1998).

3.2.4 Crystal compositions

The exact crystal compositions accounting for the $Fe^{3+}/\sum Fe$ ratio and normalizing to two cations are:

Crystal 1:

$(Mg^{2+}_{0.95},Fe^{3+}_{0.03},Fe^{2+}_{0.03})(Si^{4+}_{0.93},Al^{3+}_{0.045})O_{2.97}$

Crystal 2:

$(Mg^{2+}_{0.86},Fe^{3+}_{0.08},Fe^{2+}_{0.04})(Si^{4+}_{0.89},Al^{3+}_{0.11})O_3$

Crystal 3:

$(Mg^{2+}_{0.76},Fe^{3+}_{0.17},Fe^{2+}_{0.05})(Si^{4+}_{0.85},Al^{3+}_{0.16})O_3$

Crystal 4:

$(Mg^{2+}_{0.94},Fe^{3+}_{0.02},Fe^{2+}_{0.02})(Si^{4+}_{0.92},Al^{3+}_{0.09})O_{2.98}$

A linear increase in $Fe^{3+}/\Sigma Fe$ with increasing Al content can be observed for the crystals used in this study as shown in Fig. 3.7. This translates to a slightly non-linear increase in Fe^{3+} formula units with Al, as observed in the study of Frost and Langenhorst, (2002). It is important to note that while both Fe^{3+} and Fe^{2+}contents increase with the Al content of the crystals, the increase in Fe^{2+} is relatively minor. The $Fe^{3+}/\Sigma Fe$ ratio is not strongly correlated with the total Fe iron content. Iron oxidation state does not seem to be affected by oxygen fugacity as we had used different capsule materials such as Au, Pt and Re and water as a flux in two of our runs, which would have imposed different redox conditions.

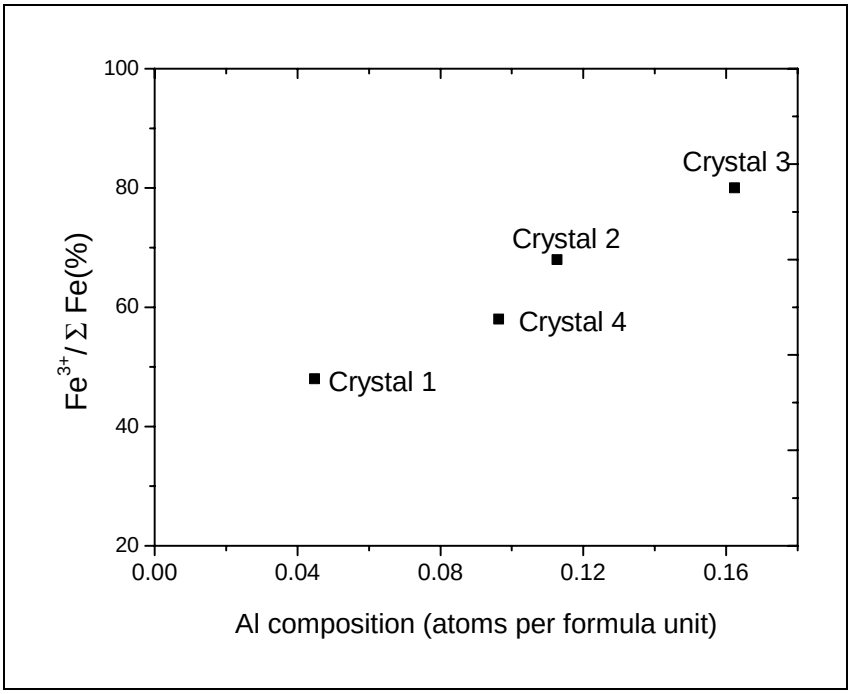

Figure. 3.7: Relation between Al content and $Fe^{3+}/\Sigma Fe$ ratio for (Fe,Al)-$MgSiO_3$ perovskites synthesized in this study. $Fe^{3+}/\Sigma Fe$ ratios were determined using Mössbauer spectroscopy and Electron energy loss spectroscopy at room temperature and liquid nitrogen temperature respectively.

The three trivalent cation substitution mechanisms for silicate perovskite are shown in the ternary diagram of Fig. 3.8, on which the 4 perovskite crystal compositions of the present study have been plotted. The oxygen vacancy and the coupled substitution mechanisms are described by equations (5), (6) and (4). The third mechanism, for which

there is little evidence, would produce an oxygen excess composition due to Fe^{3+} or Al^{3+} substitution for Mg^{2+} or Fe^{2+}. As can be seen in Fig. 3.8, crystals 2 and 3 plot along the charge coupled substitution mechanism join. Crystals 1 and 4, however, which have the lowest trivalent cation contents, plot between the charge coupled and the oxygen vacancy join. Oxygen vacancies are also indicated by the formulas for these perovskite crystals that contain less than 3 oxygens when normalized to 2 cations.

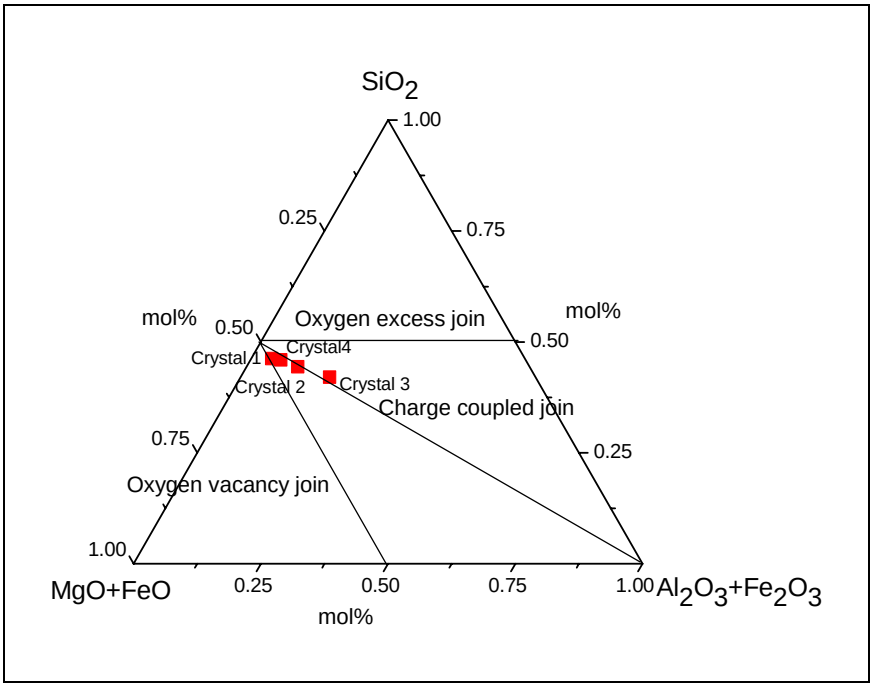

Figure. 3.8: A ternary concentration plot with the axes MgO + FeO, Al_2O_3+Fe_2O_3 and SiO_2 showing the compositions of the (Fe,Al) $MgSiO_3$crystals used in the present study in relation to different possible substitution mechanisms.

3.3 Diamond anvil cell compression experiments

3.3.1 Basics of diamond anvil cell single crystal compression technique

In this study, a BGI-design diamond anvil cell (Allan *et al*., 1996) has been employed to perform static compression experiments. For the high-pressure experiments a single crystal is placed in a hole drilled through a hardened metal foil (gasket), which is indented

between two opposed diamond anvils with flat parallel faces. This produces a pressure chamber as shown in Fig.3.9. A pressure calibrant is placed along side the sample for pressure determination within the chamber and the free volume in the pressure chamber is filled with a pressure-transmitting fluid for maintaining hydrostatic conditions. Pressure is applied to the sample by mechanically pressing the diamonds together and single crystal diffraction lines are recorded using a 4-circle diffractometer. Details of the technique can be found in Miletich *et al.*, (2000) and Miletich, (2005).

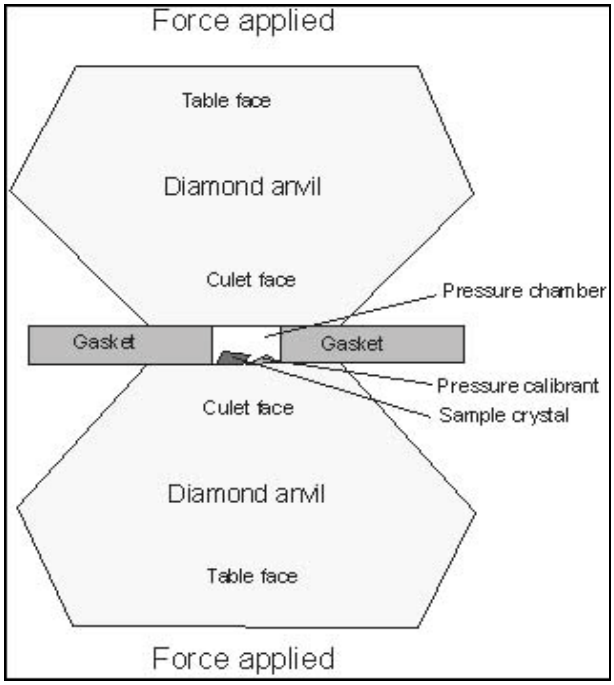

Figure. 3.9: A schematic sectional view of diamond anvil cell as is used for our compression study.

3.3.2 Compression experiments:

Single crystals with well-defined habits were selected by careful observation under an optical microscope. Most crystals were too opaque to base this selection on extinction and transparency. The final selection of the crystals was performed by checking the reflection intensity and peak profiles using a Huber single crystal diffractometer.

Single crystals with dimensions of approximately 120 μm x 80μm x 20 μm (**Crystal 1**), 130 μm x 100 μm x 50 μm (**Crystal 2**), and 120 μm x 90μm x 30 μm

(**Crystal 3**) were loaded into a diamond anvil cell sample chamber drilled into a steel (T301) plate gasket pre-indented down to 90 μm depth. Diamonds with 600 μm culets were employed and the sample chamber was 300 μm in diameter. Quartz was used as an internal pressure calibrant and a 4:1 mixture of methanol:ethanol was used as the pressure transmitting medium for our study. The unit cell parameters were determined at ambient temperature at various pressures up to 9.16 GPa for Crystal 1, 7.10 GPa for Crystal 2 and 6.97 GPa for Crystal 3 on a Huber four-circle diffractometer (non-monochromatised MoK_{α} radiation) using the 8-position centring procedure according to King and Finger (1979) and Angel *et al.,* (2000). The maximum pressure reached during each experiment was determined by failure of the gasket and consequent loss of the perovskite single-crystals, therefore it was not possible to collect data during decompression. The centring procedure and vector least square refinement of the unit cell constants were performed by SINGLE04 software according to the protocol of Ralph and Finger, (1982) and Angel *et al.,* (2000). The unit cell data at different pressures are tabulated in Table 3.3.

Table 3.3. Unit-cell lattice parameters for (Fe, Al)- $MgSiO_3$ single crystals. Standard deviations are in parentheses in terms of least units cited.

P (GPa)	*a*(Å)	*b*(Å)	*c*(Å)	V((Å)
Crystal 1				
0.00010(1)	4.78638(19)	4.94261(16)	6.9188(4)	163.680(12)
0.295(6)	4.7844(2)	4.94052(19)	6.9161(5)	163.479(15)
1.063(6)	4.77899(18)	4.93630(15)	6.9085(4)	162.976(12)
1.982(7)	4.7732(2)	4.9310(2)	6.8995(6)	162.392(17)
2.818(9)	4.7674(2)	4.9265(3)	6.8916(6)	161.860(18)
3.991(11)	4.7595(2)	4.9198(3)	6.8800(8)	161.10(2)
4.611(11)	4.7558(2)	4.9165(2)	6.8748(6)	160.747(19)
6.501(10)	4.7441(2)	4.9066(2)	6.8574(7)	159.62(2)
7.944(10)	4.73509(18)	4.89956(16)	6.8453(5)	158.810(14)
8.785(18)	4.7306(4)	4.8953(4)	6.8376(10)	158.34(3)
9.16(2)	4.7284(4)	4.8934(3)	6.8342(9)	158.13(3)
Crystal 2				
0.00010(1)	4.79239(14)	4.95152(11)	6.9343(4)	164.548(11)
0.350(5)	4.79005(15)	4.94953(11)	6.9311(5)	164.327(13)

0.681(5)	4.78789(16)	4.9480(2)	6.9278(6)	164.123(16)
1.204(4)	4.78423(18)	4.94443(15)	6.9222(6)	163.747(15)
1.685(4)	4.78099(14)	4.94197(15)	6.9179(6)	163.455(14)
2.455(5)	4.77571(15)	4.93737(15)	6.9100(5)	162.933(13)
3.491(6)	4.76913(11)	4.93217(14)	6.9005(5)	162.315(12)
4.728(7)	4.76121(16)	4.92566(17)	6.8893(6)	161.568(15)
5.420(6)	4.75672(9)	4.92167(9)	6.8825(4)	161.127(9)
6.429(9)	4.75072(12)	4.91680(10)	6.8734(4)	160.552(10)
6.910(8)	4.74773(9)	4.91416(9)	6.8695(3)	160.272(9)
7.101(9)	4.74647(13)	4.91332(12)	6.8682(4)	160.173(12)
Crystal 3				
In air	4.79977(10)	4.97947(9)	6.98054(11)	166.837(5)
0.00010(1)	4.79978(10)	4.97961(11)	6.9799(3)	166.826(10)
0.396(4)	4.79701(11)	4.97753(13)	6.9756(4)	166.558(11)
0.513(5)	4.79639(12)	4.97699(14)	6.9745(4)	166.492(11)
0.745(5)	4.79465(14)	4.97563(16)	6.9718(5)	166.321(14)
1.176(5)	4.79181(13)	4.97311(16)	6.9671(4)	166.029(13)
1.510(5)	4.78929(17)	4.97096(18)	6.9634(6)	165.781(17)
1.943(5)	4.78665(14)	4.96852(16)	6.9591(5)	165.504(14)
2.334(5)	4.78420(13)	4.96607(14)	6.9545(4)	165.231(12)
2.756(7)	4.78122(13)	4.96370(16)	6.9502(4)	164.950(12)
3.302(7)	4.77772(13)	4.96071(13)	6.9447(4)	164.596(11)
4.285(7)	4.77151(11)	4.95556(12)	6.9346(4)	163.973(10)
4.540(8)	4.76976(12)	4.95431(12)	6.9323(4)	163.817(10)
4.930(7)	4.76740(12)	4.95202(13)	6.9283(4)	163.566(11)
5.463(7)	4.76404(11)	4.94915(13)	6.9231(4)	163.232(11)
5.969(9)	4.76110(18)	4.9465(2)	6.9188(6)	162.942(17)
6.423(8)	4.75831(12)	4.94434(13)	6.9145(4)	162.674(11)
6.729(8)	4.75623(13)	4.94286(14)	6.9115(4)	162.486(12)
6.968(8)	4.7550(2)	4.9420(3)	6.9089(8)	162.36(2)

3.4 Equation of state results

3.4.1. Theoretical background

The incompressibility of a material is expressed in terms of its bulk modulus K, which is defined as $K = -V(\delta P/\delta V)$. The bulk modulus is also a function of pressure and can be described by the pressure derivative $K' = \delta K/\delta P$ and potentially also $K'' = \delta^2 K/\delta P^2$. Static compression measurements are performed at constant temperature and are therefore described using the isothermal bulk modulus K_0. Compression in the Earth, however, is not isothermal but adiabatic and is therefore described using the adiabatic bulk modulus (K_S). The relationship between the isothermal and adiabatic bulk moduli is

$$K_S = K_0 (1+\alpha\gamma T) \qquad (7)$$

where γ is the Gruneisen parameter and α is the thermal expansion coefficient.

The relationship between volume and pressure is described using an equation of state (EoS). A number of EoS formulations exist (Angel, 2000; Duffy and Wang, 2000) but the most commonly used, particularly to describe experimental data on the compression of minerals, is the Birch–Murnaghan equation of state (Birch, 1947). This is based on the assumption that the strain energy of a solid undergoing compression can be expressed as a Taylor expansion of the Eulerian strain $f_E = [(V_0/V)^{2/3}-1]/2$. Expansion to the fourth-order in f_E gives the Birch-Murnaghan EoS:

$$P = 3K_0 f_E (1+2f_E)^{5/2}\{1+3/2(K' -4)f_E +3/2\{K_0K'' + (K'- 4)(K' -3)+35/9\} f_E^{\,2}\} \qquad (8)$$

However, for most type of materials this EoS is truncated at the second order in strain, which requires K' to be fixed to 4 or at the third-order in strain which requires the coefficient of f_E^2 to be zero with an implied value of $K'' = -1/K_0(3- K')(4- K')+35/9\}$ (Anderson, 1995).

3.4.2 Unit cell lattice parameter variations with pressure

The changes in unit cell volume as a function of pressure for all three crystals are shown in Fig.3.10, where the relative volume (V/V_0) is the volume normalized to the ambient pressure volume. The maximum pressure of each experiment is constrained by the point where the gasket starts to fail and diffraction lines are broadened. This occurred at slightly different pressures in each of the three experiments with crystal 1 achieving the highest pressure of just above 9 GPa. For comparison, data for pure $MgSiO_3$ perovskite (Vanpeteghem *et al*., 2006) and $MgSiO_3$ perovskite with 5-mol% Al_2O_3 (Zhang and Weidner, 1999) are also plotted in Fig. 3.10.

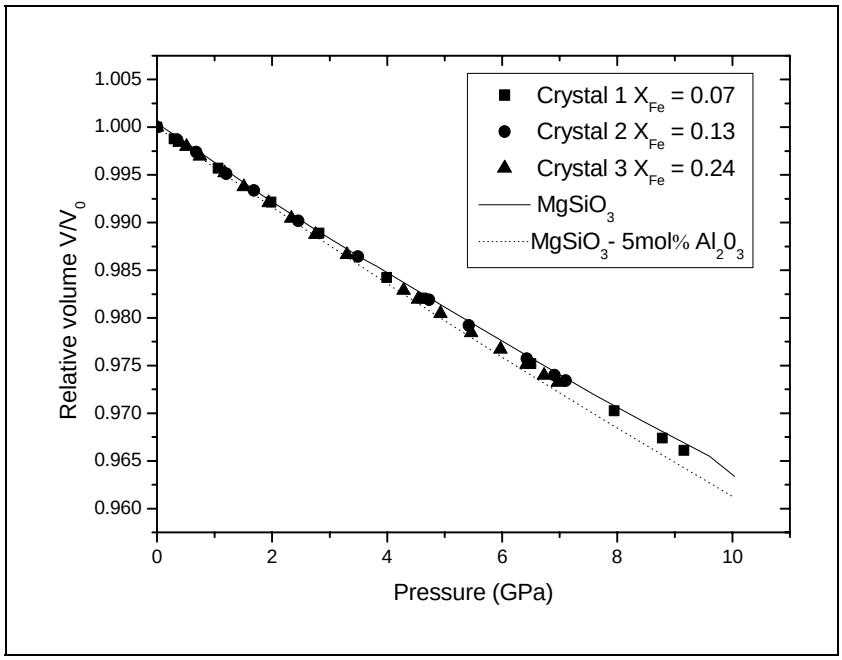

Figure. 3.10:Unit cell volume variation of (Fe,Al)-$MgSiO_3$ single crystals as a function of pressure for the 3 crystals of present study. The solid curve represents the volume variation of pure $MgSiO_3$ of Vanpeteghem *et al*., (2006) and the dotted curve has been calculated using the EoS parameters reported for a $MgSiO_3$ perovskite with 5-mol % Al_2O_3 by Zhang and Weidner, (1999).

Although the differences between the *P-V* data collected in this study and those of $MgSiO_3$ perovskite (Vanpeteghem *et al*., 2006) are very small, there is a slight increase in compressibility with increasing Fe content. In addition, the Fe and Al-bearing perovskites

synthesised in this study are less compressible than the Fe-free Al-bearing perovskite studied by Zhang and Weidner, (1999).

The axial compressibilities a/a_0, b/b_0, c/c_0 of all the three crystals as a function of pressure are shown in Fig. 3.11. The axial compression is anisotropic with the **b**-axis being the least compressible. For Crystal 1 (X_{Fe} = 0.07) and Crystal 2 (X_{Fe} = 0.13) the axial compressibilities of the **a** and **c** axes are virtually identical and are very close to those of pure $MgSiO_3$ perovskite (Vanpeteghem *et al*., 2006). For Crystal 3 (X_{Fe} = 0.24) the difference in compressibility between the **a** and **c** axes is larger, with **a**-axis being less compressible than **c**-axis. As a consequence, the axial ratio *c*/*a* remains constant for Crystal 1 at 1.445 and for Crystal 2 at 1.446, whereas it decreases with pressure for Crystal 3. The *b*/*a* axial ratio instead increases with pressure for all three crystals. The axial compressibilities reported for the Fe-free Al bearing perovskites by Zhang and Weidner (1999) show the **a**-axis to be slightly more compressible than the **c**-axis. This suggests that there is a different mechanism by which Al is substituted into the perovskite structure in the absence or in the presence of Fe.

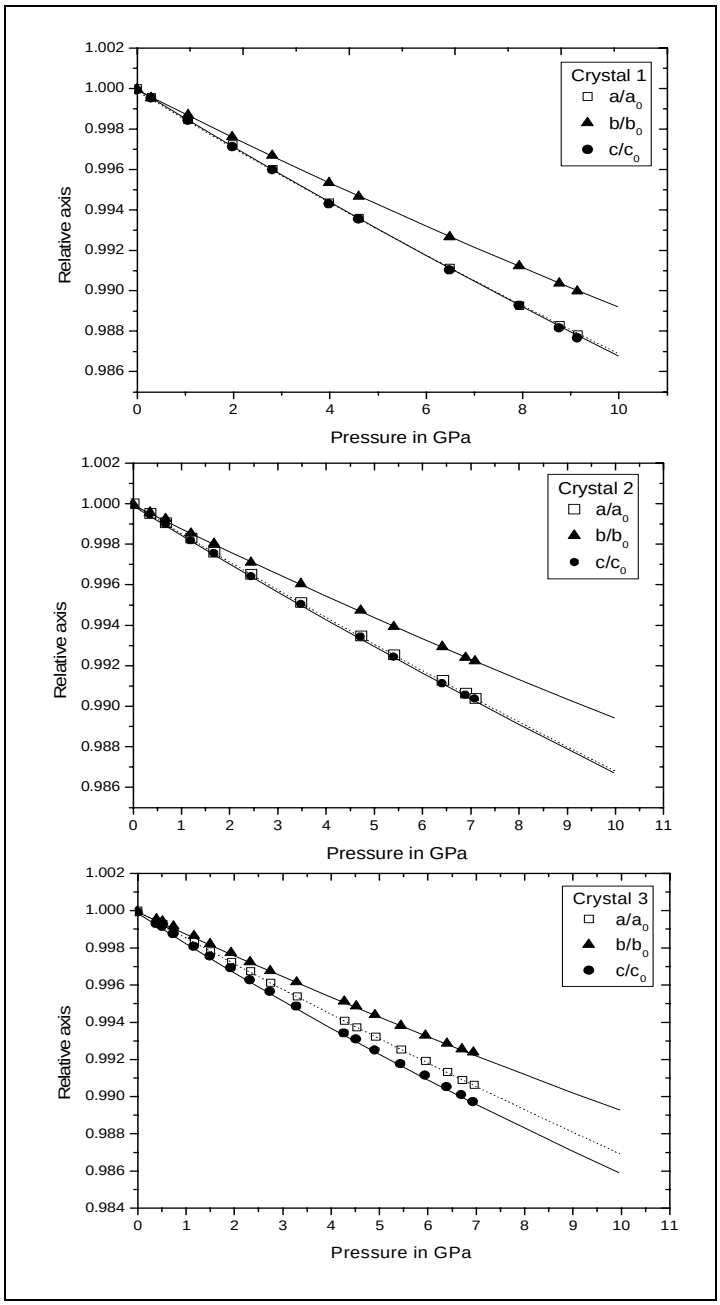

Figure 3.11. Axial compressibilities of the (Fe,Al)-$MgSiO_3$ perovskite single crystals. The solid curves are the 3rd-order Birch Murnaghan EoS fits to the data: (a) Crystal 1, X_{Fe} = 0.07 (b) Crystal 2, X_{Fe} = 0.13 and (c) Crystal 3, X_{Fe} = 0.24.

3.4.3 F_E-f_E plots and EoS parameters

A normalised stress, defined as $F_E = P/3f_E (1+2 f_E)^{5/2}$ has been plotted versus the Eulerian strain f_E for each crystal (Fig. 3.12) in order to have a visual assessment of the order of the Birch-Murnaghan EoS required to fit the compression data (Angel, 2000).

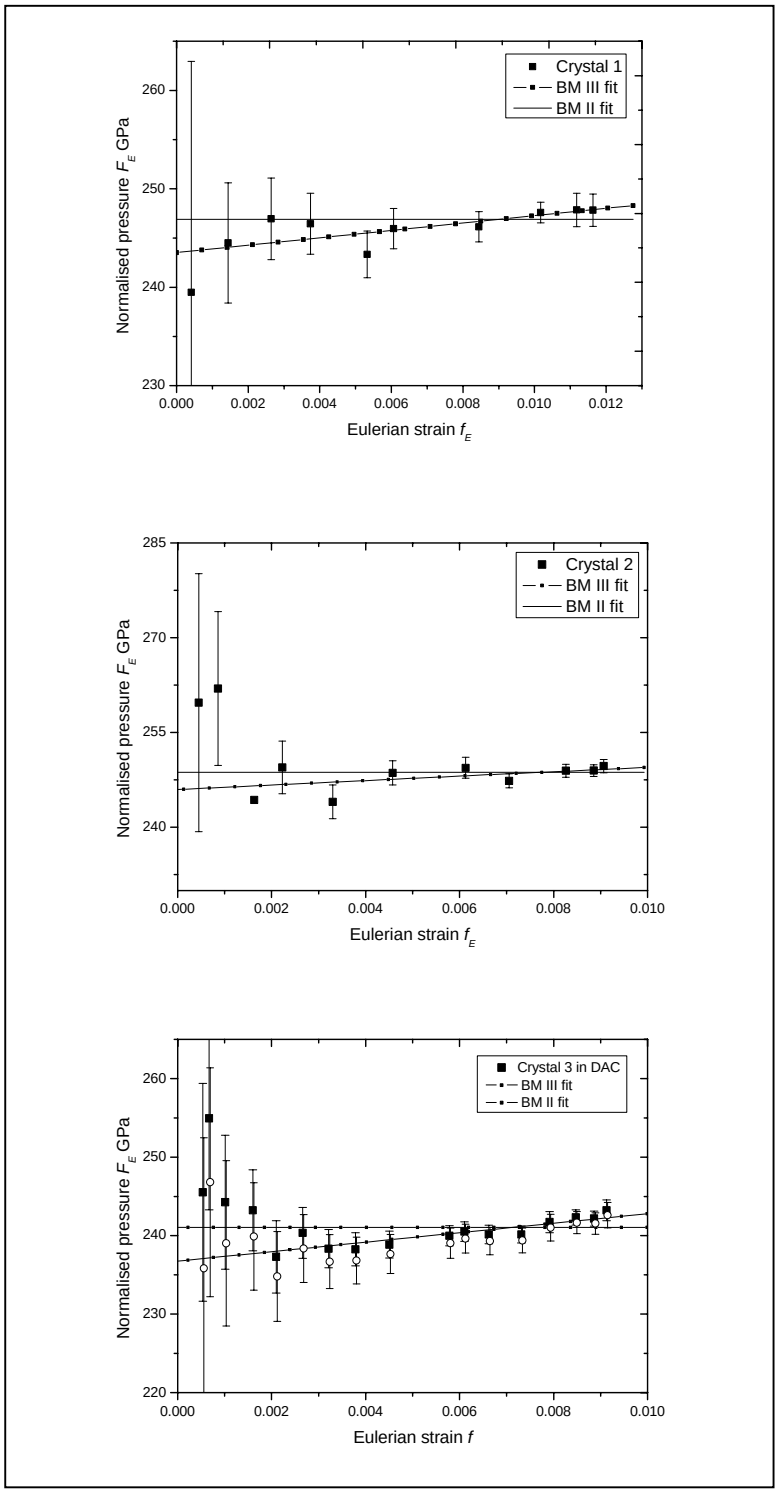

Figure. 3.12 F_E-f_E plots based on the Birch-Murnaghan EoS for (Fe,Al)-$MgSiO_3$ perovskite single crystals. The values of V_0 used to calculate the finite strain are those measured at 1 bar. The open circles shown in the F_E-f_E plot of Crystal 3, are the finite strain values calculated with volume of the crystal determined in air (Equations for the weighted fits are mentioned in the text).

Weighted linear fits to data points for the three crystals indicate a positive slope, which implies that K' is greater than 4. For comparison, weighted horizontal linear fits (implying K' = 4) also are shown in Fig. 3.12, although in this case we observe an increase of the chi-square. In the case of Crystal 3 the F_E-f_E data do not define a straight line, suggesting that a fourth-order truncation of the Birch-Murnaghan EoS might be considered. However, it has been shown (Angel, 2000) that such curvature for small strains, i.e., for data collected at low pressures, is often due to a wrong value of V_0 being used in the calculation of the Eulerian strain. If the value of the volume measured with crystal 3 glued on a glass fibre (i.e., in air, Table 3.3), instead of that measured with the same crystal in the DAC is used to calculate the *F-f* plot, linear behaviour is obtained (Fig. 3.12, Crystal 3 open circles). Moreover, the intercept on the *F* axis is equal to the bulk modulus, K_0, value and can hence be used to assess the goodness of the EoS fit procedure. *F-f* plots have been calculated also for the individual crystal axes and are shown in Fig. 3.13 indicating positive slope. Since the F_E-f_E plots (Fig. 3.12) suggest that K' is larger than 4 for all three crystals, the *P-V* data have been fitted with a 3rd order Birch–Murnaghan EoS using the Eosfit52 program (Angel, 2000). However, for comparison with data present in the literature, fitted practically uniquely with K' fixed to the value of 4, a 2nd order Birch–Murnaghan EoS has also been used. A linearised Birch-Murnaghan EoS (implemented in the Eosfit52 software) in which the cube of a unit-cell axis is used instead of the volume has been used to fit the unit cell *a*, *b* and *c* parameters of the three crystals. The bulk moduli so obtained are $K_0 = 1/3\beta_0$, where β_0 is the axial compressibility. The resulting equation of state parameters are reported in Table 3.4. The values obtained are in good agreement with those obtained from the linear fits of the F_E-f_E plots.

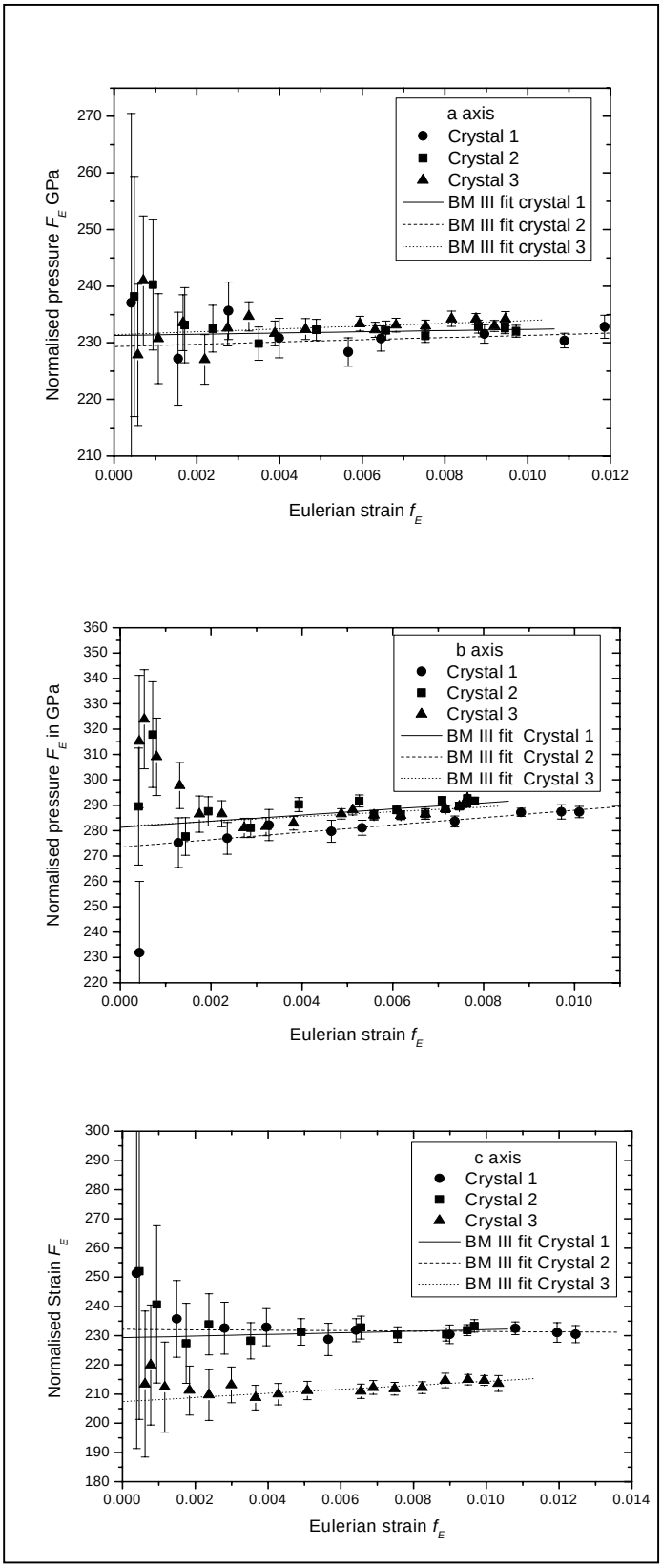

Figure. 3.13 F_E-f_E plots based on the Birch-Murnaghan EoS for individual crystal axes of the three (Fe,Al)-$MgSiO_3$ perovskite single crystals of the present study. Equations for the weighted fits are mentioned in text below.

Equations for the weighted fits shown in the F_E-f_E plots of volumes and crystal axes for crystal 1, 2 and 3 in Figs. 3.12 and 3.13 are as follows:

Crystal 1

For volume data $F_E = 243(2) + 375(243)\ f_E$
Horizontal line $F_E = 246.9(6)$

a-axis F_E(a) = 230(3) + 124(294) f_E (a)
b-axis F_E(b) = 274(4) + 1470(513) f_E(b)
c-axis F_E(c) = 231(5) + 20(522) f_E (c)

Crystal 2

For volume data $F_E = 245(2) + 352(272)\ f_E$
Horizontal line $F_E = 248.7(5)$

a-axis F_E (a) = 231(2) + 107(262) f_E (a)
b-axis F_E (b) = 283(3) + 1025(436) f_E (b)
c-axis F_E (c) = 229(5) + 275(583) f_E (c)

Crystal 3

For volume data $F_E = 237(1) + 604(211)\ f_E$
Horizontal line $F_E = 241.0(4)$

a-axis F_E (a) = 231(2) + 250(204) f_E (a)
b-axis F_E (b) = 281(3) + 953(408) f_E (b)
c-axis F_E (c) = 212(1) + 65(196) f_E (c)

Table 3.4: Birch-Murnaghan equation of state parameters for (Fe,Al)-$MgSiO_3$ perovskite single crystals of present study. (Abbreviations: BM II = Birch-Murnaghan 2nd order equation of state and BM III = Birch-Murnaghan 3rd order equation of state.)

	Crystal 1	Crystal 2	Crystal 3
		BM II (*K'* fixed to 4)	
a_0 (Å)	4.78637(10)	4.79241(7)	4.79974(5)
$K_0(a)$ GPa	231.1(9)	232.0(6)	233.6(5)
b_0 *(Å)*	4.94233(10)	4.95143(10)	4.97963(9)
$K_0(b)$ GPa	291(1)	288(1)	287(1)
c_0 *(Å)*	6.9189(3)	6.9343(2)	6.98035(11)
$K_0(c)$ GPa	231(1)	232(1)	210.9(8)
V_0 (Å^3)	163.673(7)	164.547(7)	166.831(5)
K_0 (GPa)	247.4(7)	248.8(7)	240.6(6)
		BM III	
a_0(Å)	4.78643(13)	4.79247(10)	4.79979(7)
$K_0(a)$GPa	229(3)	229(2)	231(2)
K'	4.6(7)	4.7(7)	4.7(6)
b_0*(Å)*	4.94251(12)	4.95156(11)	4.97976(10)
$K_0(b)$GPa	276(4)	282(5)	278(4)
K'	7(1)	7(1)	7(1)
c_0*(Å)*	6.9189(3)	6.9345(3)	6.98051(10)
$K_0(c)$GPa	231(6)	227(6)	200(3)
K'	4(1)	5(1)	8(1)
V_0(Å^3)	163.681(9)	163.688(9)	166.840(4)
K_0(GPa)	243(3)	240(2)	234(2)
K'	5.0(7)	6.1(6)	6.5(5)

.

The results reported in Table 3.4 are consistent with an increase in compressibility of the perovskite structure with increasing Fe and Al content as already shown in Fig. 3.10. This increase is due to softening in the **c** direction. A major difference between the results presented in this study and those reported in the literature is the indication that, at least for Fe-Al-bearing perovskite, K' is larger than 4 and increases with increasing Fe and Al content. A comparison between the bulk moduli obtained in this study and those reported

in the literature for Al- and Fe-bearing $MgSiO_3$ perovskites is shown in Fig. 3.14. There is a clear discrepancy among all these data, which may be attributed to the different techniques and different synthesis conditions used.

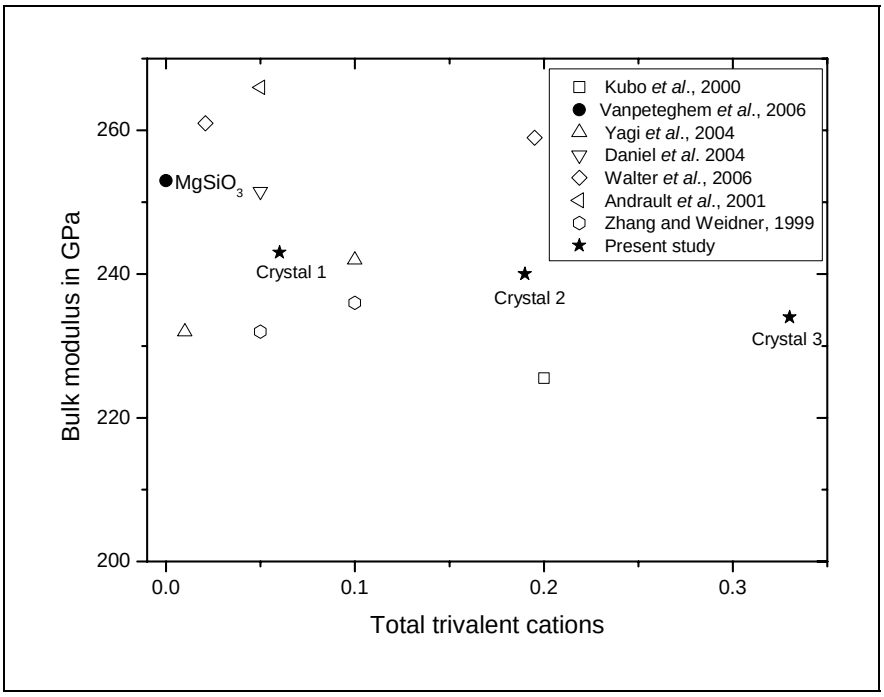

Figure. 3.14 Comparison of bulk moduli of Al- and Fe-bearing perovskite plotted as a function of total trivalent cation (Al and Fe) content. Open data points are for Fe-free Al-rich samples; filled circle is for pure $MgSiO_3$ perovskite; stars are for the crystals of this study containing both Fe^{3+} and Al^{3+}.

In particular, the results of this study are in contrast to the only other study on the compressibility of (Al,Fe)-bearing $MgSiO_3$ perovskite (Andrault *et al*., 2001), which reports a stiffening of the perovskite structure with the incorporation of Al and Fe. However, Andrault *et al*., (2001) annealed their powdered sample by laser heating between data collections, so one cannot exclude that such annealing could have changed the chemical or physical state of the sample between measurements. The softening observed for our samples cannot be ascribed to the presence of oxygen vacancies, because only crystal 1 requires a very small concentration of vacancies for charge balance. This suggests that Al and Fe substitution modifies the deformation mechanism of the A and B sites of $MgSiO_3$ perovskite, causing an increase in the polyhedral compressibility. However, accurate structural data obtained at high-pressure are required to confirm this hypothesis.

3.4.4 Octahedral tilting

The variations of the octahedral tilting θ, ϕ, and Φ with pressure have been calculated from the unit cell lattice parameters according to equations (1-3) and are reported in Figs. 3.15-17. The θ angle (Fig. 3.15) shows a clear dependence on composition, suggesting that distortion around the pseudocubic [110] axis increases with increasing Fe content. However, it also increases uniformly with pressure independently of the crystal composition. The tilting angle ϕ (the distortion around the pseudocubic [001] axis) shows a similar dependence on composition at room pressure; the angle remains almost constant with increasing pressure for pure $MgSiO_3$ and for very low amounts of Fe and Al substitution (Crystal 1 and 2), whereas it decreases with increasing pressure for crystal 3 (Fig. 3.16). This supports the suggestion that there is a change in the deformation mechanism of the A and B sites of the perovskite structure in order to accommodate significant amounts of Fe and Al.

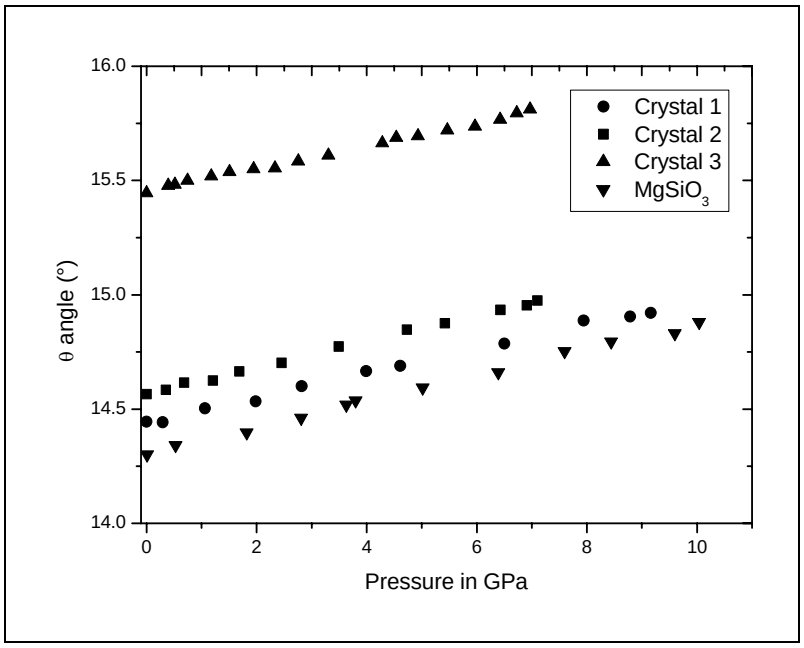

Figure. 3.15: Variation of θ tilting angle as a function of Fe content in (Fe,Al)-$MgSiO_3$ perovskites with pressure. $MgSiO_3$ data are from Vanpeteghem *et al.*, (2006).

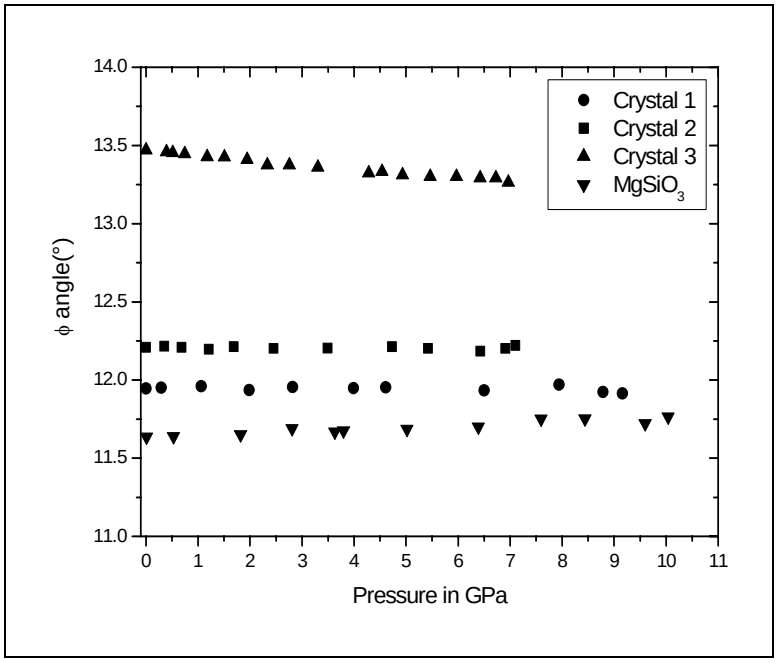

Figure. 3.16. Effect of pressure and Fe content on the octahedral tilting ϕ in (Fe,Al)-$MgSiO_3$ perovskites. $MgSiO_3$ data are from Vanpeteghen *et al*., (2006).

The tilting angle Φ (the distortion around the pseudocubic [111] axis) increases with increasing Fe content and with increasing pressure (Fig. 3.17). However, due to the combined effect of the other tilting angle, the slope as a function of pressure of crystal 3 is shallower than for pure $MgSiO_3$ perovskite and for crystals 1 and 2. From these results we can conclude that, at lower mantle conditions perovskite will continue to be in the distorted orthorhombic structure even after incorporation of Fe and Al.

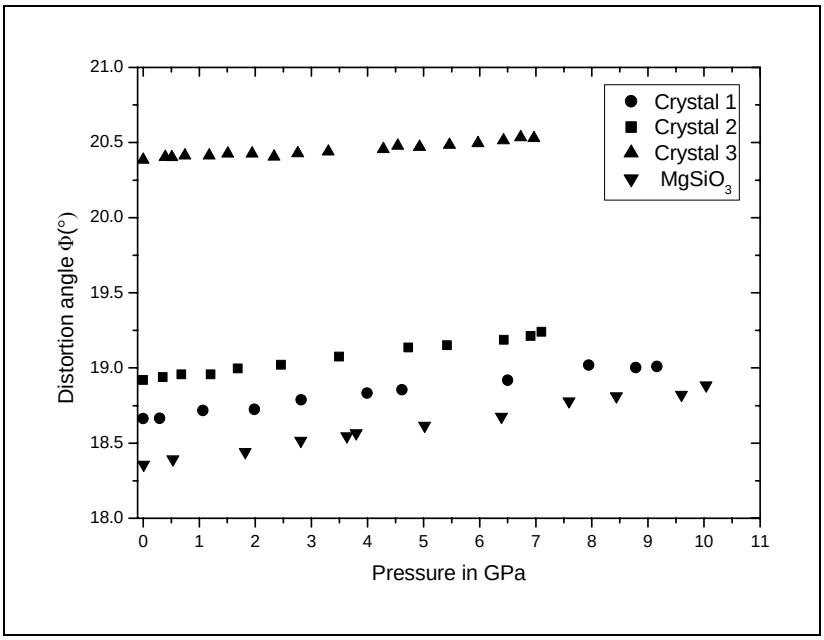

Figure 3.17: Distortion angle Φ for (Fe,Al)-$MgSiO_3$ perovskites as a function of composition and pressure. The orthorhombic distortion is found to increase with increasing pressure for all compositions. Pure $MgSiO_3$ data are also plotted for a comparison from Vanpeteghem *et al*., (2006).

3.5.Discussion

3.5.1 The Elasticity of the Earth's lower mantle

Assuming a pyrolite bulk mantle composition, the Earth's lower mantle should be composed of approximately 80-volume % magnesium silicate perovskite coexisting with magnesiowüstite and calcium silicate perovskite. Comparison of seismically-inferred properties for the lower mantle with model properties based on measured bulk and shear moduli for such a mantle assemblage provides the best test for the composition and temperature of the lower mantle.

The elasticity data determined from single crystal compression experiments have been combined with existing thermoelastic data in order to calculate the variation in density and bulk modulus over the depth range of 670–2571 km, which covers the entire lower mantle excluding the D'' low velocity zone. A number of studies have reported thermoelastic properties for silicate perovskite from experiments conducted at simultaneous high pressure and temperature (Mao *et al.,* 1991; Yeganeh–Haeri, 1991;

Wang *et al*., 1994; Utsumi *et .al,* 1995; Funamori *et al*., 1996; Fiquet *et al*., 1998; Fiquet *et al*., 2000). For these calculations we have used the high temperature properties from the data set of Funamori *et al.,* (1996) [$K_{0,T}$ = 261 GPa, $K'_{0,T}$ = 4, $(dK/dT)_P$ =-0.028 Gpa K^{-1} , α_0 = 1.98*10^{-5} K^{-1}, α_1 = 0.82*10^{-8} K^{-2} and α_2 = -0.47(K)] which were determined for $MgSiO_3$ perovskite. The room pressure volume (V_0) at high temperature was calculated using thermal expansion coefficients and the equation

$$V_{0,T} = V_{T,0} \exp \int_{298}^{T} \alpha_{T,0} dT \qquad (9)$$

In view of the lack of high-temperature elastic property data for Al-bearing perovskites and the limited data for Fe-bearing perovskites, we have no option but to assume that they are the same as for the $MgSiO_3$ end member. Mao *et al.,* (1991) proposed that thermal expansivitites of pure and Fe-bearing perovskite were similar, but that the temperature dependence of the bulk modulus of Fe-bearing perovskite was greater, i.e., $(dK/dT)_P$ = -6.3*10^{-2} Gpa K^{-1}. In order to examine this proposal we have also made calculations assuming the value of $(dK/dT)_P$ reported by Mao *et al*., (1991). Almost all previous studies on elastic properties of $MgSiO_3$ perovskite have fitted the experimental data assuming a second order Birch-Murnaghan equation of state, i.e., with K' fixed at 4. Our data, however, provide strong evidence that, at higher Al and Fe concentrations a third-order Birch-Murnaghan equation of state is required with a K' higher than 4. To obtain an overview of how fixing K' to 4 and K' > 4 can effect calculated lower mantle properties; calculations have been performed using both 2nd and 3rd order fits to our data set. All the calculations were performed along the adiabatic geotherm of Brown and Shankland, (1981) fixed at 1873 K for a depth of 670 km.

Densities calculated along an adiabatic temperature gradient for the three crystals are shown as a function of pressure in the mantle in Fig. 3.18. When K' is fixed at 4 and $(dk/dT)_P$ = -0.028 GPa K^{-1} (Funamori *et al.,* 1996), there is a clear increase in density with increasing Fe and Al concentration at lower mantle conditions. Densities for Crystals 1 and 2 are only slightly larger than those calculated for $MgSiO_3$ perovskite throughout most of the lower mantle. However, the slightly lower bulk moduli of Crystals 1 and 2 means that their densities become smaller than $MgSiO_3$ perovskite close to the core mantle boundary. The difference in densities between Crystals 1 and 2 also decreases throughout the lower mantle due to the minor differences in their bulk moduli. The density of Crystal 3, which

has the highest Fe content remains significantly larger than the other two crystals throughout the lower mantle even though it has a lower bulk modulus. When $(dK/dT)_P$ = -0.063 GPa/K, as proposed by Mao *et al*., (1991), is employed for this calculation, the effect of Fe and Al on densities in the lower mantle becomes much stronger as a result of the bulk moduli being lower. The Preliminary Reference Earth Model (PREM), (Dziewonski and Anderson, 1981), density curve is quite consistent with a monomineralic perovskite lower mantle, but a perfect match would only be obtained if the lower mantle increased in Fe content towards the base. Based on similar comparisons, previous studies have argued that the lower mantle may have a higher Si/Mg ratio than the upper mantle and therefore be composed mostly of perovskite (Anderson *et al.,* 1995). Large payoffs exist, however, between the value of $(dK/dT)_P$ used and the proportion of coexisting magnesiowüstite in the modelled assemblage (Fiquet *et al*., 1998).

As discussed previously, the compression data reported in this chapter are actually consistent with values of K' >4 for Fe and Al bearing perovskite, and K' was also found to increase with increasing Fe content. In the lower panel of Fig. 3.18 density calculations have been performed using the results of the 3rd order Birch-Murnaghan equation of state fits. The result is a much smaller change in density in the lower mantle, compared to room pressure, as a result of Fe and Al substitution, due to the higher values of K' which make Fe-rich perovskites less compressible at lower mantle conditions. Very large changes in Fe concentration in the lower portion of the lower mantle would be required to match the changing slope of the PREM density curve when K' > 4.

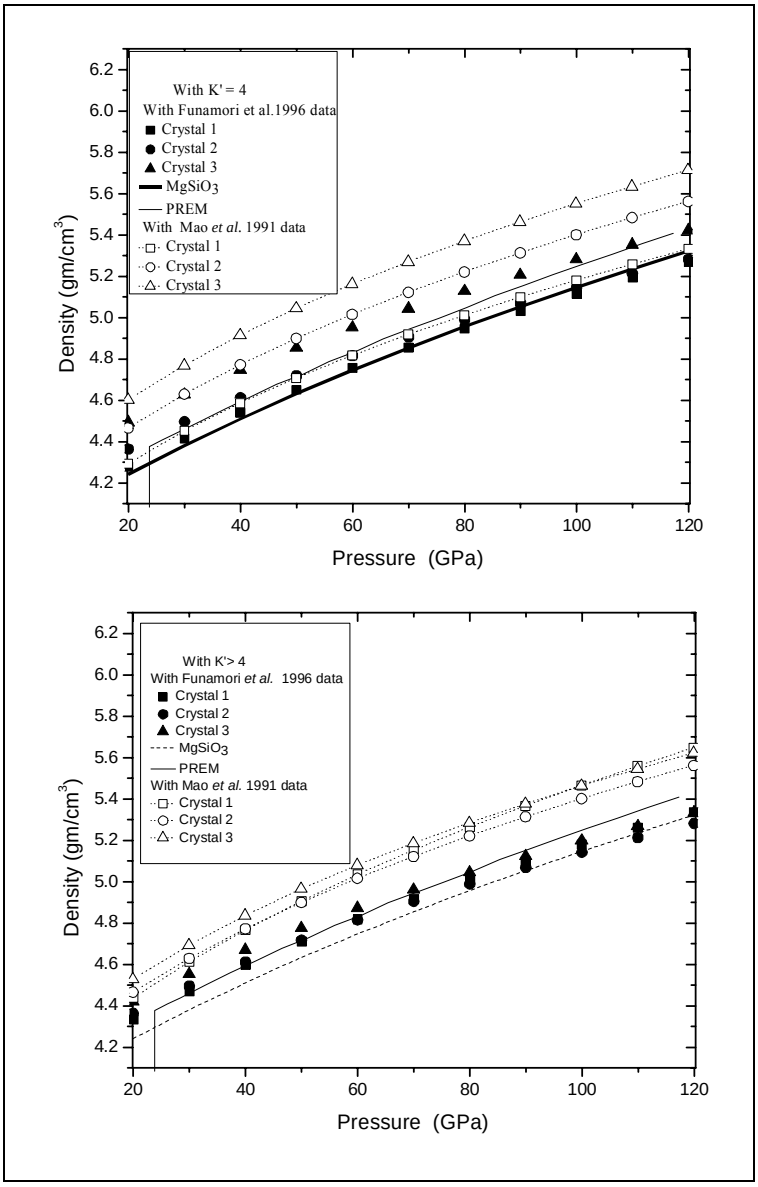

Figure 3.18: Density profiles calculated for the three crystals with K' = 4 and > 4 as determined from the compression data of this study. Two $(dk/dT)_P$ values were used for comparison as stated in the text. PREM data of Dziewonski and Anderson, (1981) and pure $MgSiO_3$ density calculated based on compression data of Vanpeteghem *et al.,* (2006), are also plotted for comparison.

We have also calculated K_T, the bulk modulus at pressure and temperature, for the three crystals of this study, using the equation:

$$K_{T,0} = K_{298,0} + (dK_{T,0}/dT)_P(T-298) \quad (10)$$

where, $K_{T,0}$ is the bulk modulus at temperature, $K_{298,0}$ is the bulk modulus at ambient conditions and $(dK_{T,0}/dT)_P$ is the temperature derivative of the bulk modulus, taken from either Funamori *et al.*, (1996) or Mao *et al*., (1991), and the equation

$$K_T = K_{T,0} + (dK_{T,0}/dP)_T P \quad (11)$$

where $(dK_{T,0}/dP)_T$ is the pressure derivative of the bulk modulus. An estimate for the value of K_T for the lower mantle can be obtained from PREM K_S (the adiabatic bulk modulus) estimates using the equation:

$$K_T = K_S/(1+\alpha\gamma T) \quad (12)$$

where, α is the thermal expansivity and γ is the gruneisen parameter, values of which are tabulated for the lower mantle in Brown and Shankland, (1981).

Regardless of the value of $(dK_{T,0}/dT)_P$ employed, K_T curves calculated for perovskite samples assuming K' > 4 display a much greater divergence as a function of composition than when K' is assumed to be 4 (Fig. 3.19). This is the opposite behaviour from that observed for densities, where the greatest effect of Fe content occurs for K' = 4. Very large changes in Fe content would be required, on the other hand, to influence K_T in the lower mantle if K' = 4. In addition, the slope of the PREM value of K_T is shallower than those calculated for the three crystals of this study if K' > 4, which means that Fe contents would have to decrease in the lower portion of the lower mantle to be consistent with the PREM slope. Again this is the opposite conclusion to that obtained based on density. K_T determinations with K' > 4 are much higher at the base of the mantle compared with PREM and provide a poor fit to the observations compared to when K' = 4. The addition of magnesiowüstite to the model assemblage would reduce K_T but not by more than 10 % (Fiquet *et al.,* 1998). Under these circumstances, values of K' = 4 and $(dk/dT)_P$ = -0.028 GPa K^{-1} give the best agreement with the PREM value of K_T for lower mantle.

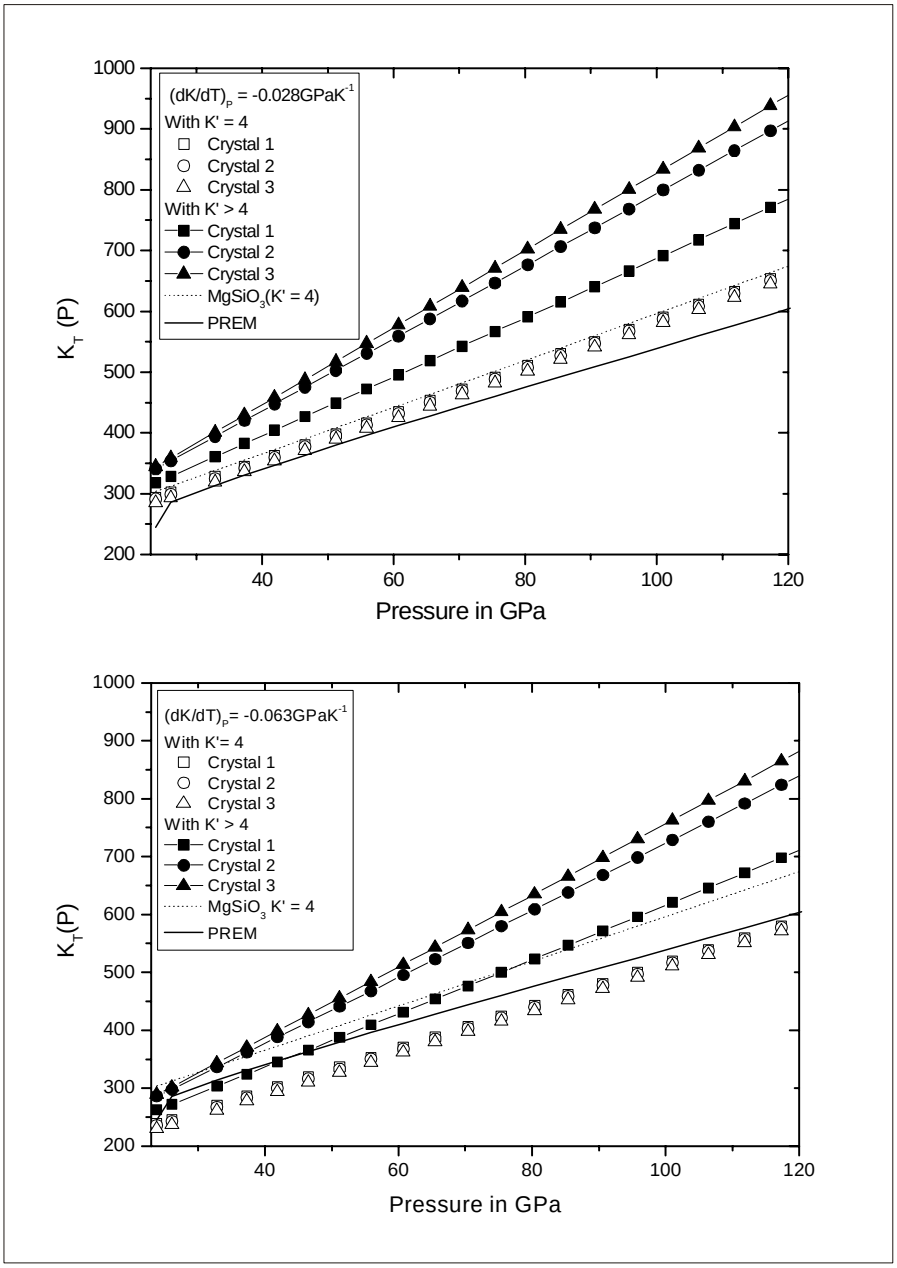

Figure 3.19: Comparison of bulk modulus $K_T(P)$ profiles along with PREM lower mantle model (Dziewonski and Anderson, 1981) along the temperature profile of Brown and Shankland, (1981). Bulk modulus of $MgSiO_3$ is also plotted for a comparison based on data of Vanpeteghem *et al.,* (2006). K_T profile for the three crystals calculated using $(dk/dT)_P$ of –0.028 GPa K^{-1} and -0.063 GPa K^{-1} values as reported by Funamori *et al.,* (1996) for a $MgSiO_3$ composition and Mao *et al.,* (1991) for a Fe-bearing $MgSiO_3$ composition both for a K' of 4 and K' > 4 as obtained in this study by 3rd order Birch-Murnaghan fit.

3.5.2 The effect of pressure on $Fe^{3+}_{VIII}Al^{3+}_{VI}O_3$ perovskite substitution.

Experimental observations indicate (Frost *et al*., 2004) that even at the lowest plausible oxygen fugacity for the lower mantle, $(Fe,Mg)(Al,Si)O_3$ perovskite contains a significant Fe^{3+} content ($Fe^{3+}/\sum Fe > 0.5$). As the upper mantle has a very low $Fe^{3+}/\sum Fe$ ratio (<0.03) two possible scenarios for the redox state of the lower mantle can be proposed: either the lower mantle is more oxidized than the upper mantle or at lower mantle conditions Fe^{2+} is oxidised to Fe^{3+} by some agent also present in the bulk mantle. Evidence for whole mantle convection contradicts the first possibility, as it would have been impossible to maintain a low $Fe^{3+}/\sum Fe$ ratio in the upper mantle if it were mixed through geologic time with a highly oxidised lower mantle reservoir. Although the second possibility is therefore more likely, none of the oxidising agents active in the upper mantle (e.g., CO_2, SO_2) are abundant enough to produce the required Fe^{3+} contents. In the absence of such an agent, disproportionation of FeO i.e.,

$$3FeO = Fe+Fe_2O_3. \quad (13)$$

becomes the only mechanism capable of producing Fe^{3+} in sufficient abundance. Frost *et al*., (2004) showed experimentally that about 1 wt % of Fe metal would be required to balance the Fe^{3+} requirement of perovskite at 25 GPa within a pyrolitic lower mantle bulk composition.

The equilibrium between $(Fe,Mg)(Al,Si)O_3$ perovskite and Fe metal can be described by the equation:

$$AlAlO_3 + 3FeO = Fe + 2AlFeO_3 \quad (14)$$
$$\text{Perovskite} \quad \text{Mw} \quad \text{Metal} \quad \text{Perovskite}$$

where, Mw is magnesiowüstite. Frost *et al*., (2004) measured high concentrations of the $AlFeO_3$ component in perovskite in equilibrium with metallic Fe and concluded that this equilibrium must be shifted strongly to the right at conditions compatible with the top of

the lower mantle. By assessing the effect of $Al^{3+}_{VIII}Al^{3+}_{VI}O_3$ ($Al^{3+}_{VIII} + Al^{3+}_{VI} \leftrightarrow Mg^{2+}_{VIII} + Si^{4+}_{VI}$), $Fe^{3+}_{VIII}Al^{3+}_{VI}O_3$ ($Fe^{3+}_{VIII} + Al^{3+}_{VI} \leftrightarrow Mg^{2+}_{VIII} + Si^{4+}_{VI}$) and $Fe^{2+}_{VIII}Si^{4+}_{VI}O_3$ ($Fe^{2+}_{VIII} \leftrightarrow Mg^{2+}_{VIII}$) substitutions on the volume of (Fe,Mg)(Al,Si)O_3 perovskite, it should be possible to determine whether disproportionation of FeO will be favoured at the higher-pressure conditions of the deep lower mantle. The volume and compression results presented in this chapter provide data that help to understand the likely volume effect.

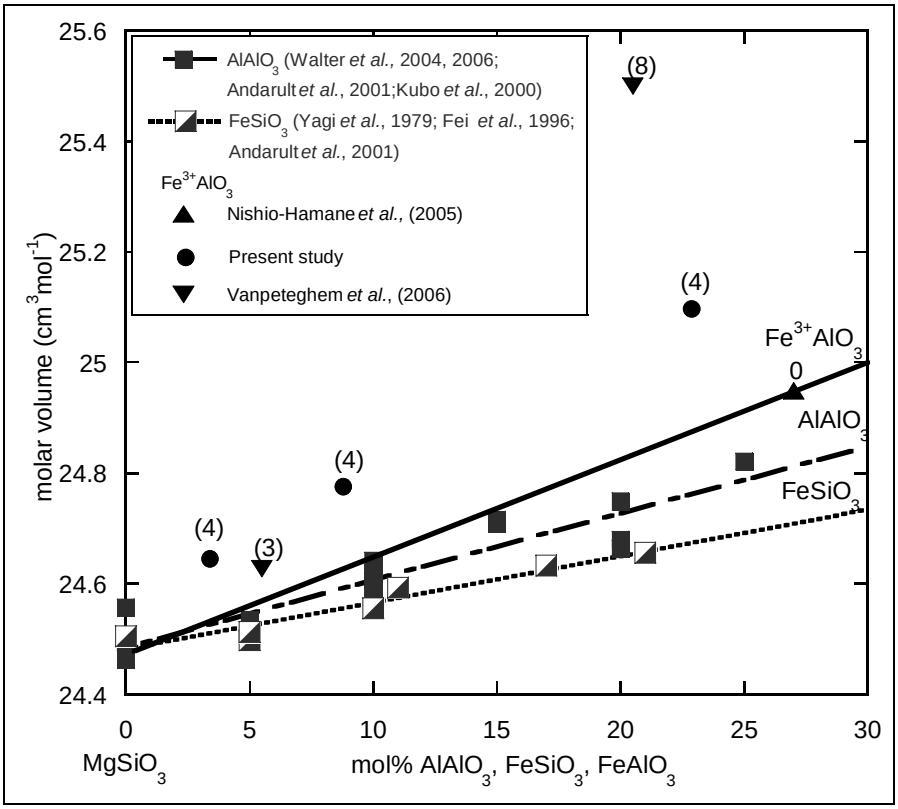

Figure 3.20. Effect of $Fe^{2+}_{VIII}Si^{4+}_{VI}O_3$, $Al^{3+}_{VIII}Al^{3+}_{VI}O_3$, $Fe^{3+}_{VIII}Al^{3+}_{VI}O_3$ substitutions on the molar volume of magnesium silicate perovskite.

Fig. 3.20 shows the change in molar volume of $MgSiO_3$ perovskite as a function of possible substitution mechanisms determined using room pressure volume data from this and previous studies. The addition of $Al^{3+}_{VIII}Al^{3+}_{VI}O_3$ and $Fe^{2+}_{VIII}Si^{4+}_{VI}O_3$ components have similar effects on the molar volume of perovskite with the former having a slightly greater effect.

Chapter 3: Discussion

Although the perovskite samples synthesised in this study have high $Fe^{3+}/\Sigma Fe$ ratios, all samples contain Fe^{2+} and therefore do not lie on a compositional join between $MgSiO_3$ and $Fe^{3+}_{VIII}Al^{3+}_{VI}O_3$. All single crystals synthesised in this study also contain 4-mol % of $Fe^{2+}_{VIII}Si^{4+}_{VI}O_3$, which is indicated by the figure in brackets next to each data point. These data show that in comparison to $Al^{3+}_{VIII}Al^{3+}_{VI}O_3$ and $Fe^{2+}_{VIII}Si^{4+}_{VI}O_3$ substitutions the $(Fe,Mg)(Al,Si)O_3$ perovskites have larger molar volumes. The only sample with a composition on the $MgSiO_3$- $Fe^{3+}_{VIII}Al^{3+}_{VI}O_3$ join is that synthesised by Nishio-Hamane *et al.*, (2005) at approximately 50 GPa in a diamond anvil cell. Although the Fe^{3+} content was not independently confirmed, it was assumed to be the same as that of the staring composition. The volume of this sample is smaller than the sample synthesised in our study at a similar $Fe^{3+}_{VIII}Al^{3+}_{VI}O_3$ content and a trend starts to emerge particularly when the volumes and $Fe^{2+}_{VIII}Si^{4+}_{VI}O_3$ contents of $(Fe,Mg)(Al,Si)O_3$ perovskite samples synthesised by Vanpeteghem *et al.*, (2006) are also considered. Increasing the $Fe^{2+}_{VIII}Si^{4+}_{VI}O_3$ content of $(Fe,Mg)(Al,Si)O_3$ perovskite samples increases their molar volumes dramatically. In other words, the substitution of $Fe^{2+}_{VIII}Si^{4+}_{VI}O_3$ into Al-free perovskite has a smaller effect on molar volume than when it substitutes into Al-bearing perovsktie. As perovskite must contain Al in the lower mantle the large effect on the molar volume should make Fe^{2+} substitution in perovskite unfavourable with increasing pressure.

Using data in Fig. 3.20 and compression data from this study and the literature (Fei, 1996; Walter *et al.*, 2004) the molar volume change of the equilibrium (eq. 14), at pressures of the lower mantle is calculated to be approximately –2 cm^3/mol. This implies that disproportionation of FeO should be favoured with increasing pressure and therefore is likely to take place throughout the perovskite-bearing region of the lower mantle. In addition, however, the large effect on the perovskite molar volume of $Fe^{2+}_{VIII}Si^{4+}_{VI}O_3$ substitution into $(Fe,Mg)(Al,Si)O_3$ perovskite should drive Fe^{2+} out of perovskite with increasing pressure and into magnesiowüstite. This should cause perovskite to decrease in total Fe content with pressure but to become more Fe^{3+} rich. Some support of this can be found in the fact that while in this study it was not possible to synthesise pure Fe^{3+} bearing perovskite at 25 GPa, as attempted in the synthesis of crystal

3 which contained only Fe^{3+} in the starting composition, this was possible in the study of Nishio-Hamane *et al*., (2005) performed at approximately 50 GPa.

3.6 Conclusions

The substitution Al and Fe^{3+} into $MgSiO_3$ perovskite occurs by a coupled substitution mechanism with the possibility that small concentrations of oxygen vacancies are present only at low trivalent cation concentrations.

Static compression measurements show that the substitution of Al and Fe into $MgSiO_3$ perovskite increases the compressibility. The axial compression is anisotropic with the **b** axis being the least compressible, and **a** and **c** axes having virtually identical compressibilities. Axial compressibilities of Fe-free Al-bearing perovskites (Zhang and Weidner, 1999) show the **a** axis to be slightly more compressible than the **c** axis implying that there is a different mechanism by which Al is substituted into the perovskite structure in the absence or in the presence of Fe.

Fitting the data to a 2nd order Birch-Murnaghan EoS (K' = 4) gives values for the bulk modulus that decrease from 247 to 240 GPa as the Fe content increases from 0.12 to 0.22 formula units. These values are lower than the value of 253 GPa reported for $MgSiO_3$ perovskite (Vanpeteghem *et al*., 2006) based on single crystal determinations. However, *f-F* plot analyses indicate that a 3rd order Birch- Murnaghan fit to the data is statistically justified. These fits indicate a larger drop in bulk modulus with Fe and Al substitution from 243 to 234 GPa and an increase in K' from 5 to 6.5. The decrease in bulk modulus likely arises from an increase in polyhedral compressibility.

Combining these data with thermoelastic data from the literature indicates that perovskite densities calculated along a lower mantle geotherm are insensitive to Fe-Al substitution if the 3rd order Birch- Murnaghan fit to the data is employed. The resulting values of K' from this fit which are >4 provide a poor fit to the estimated bulk modulus of the lower mantle. If on the other hand the 2nd order Birch- Murnaghan fit is employed the calculated densities when compared to PREM are consistent with an increase in Fe-Al substitution in the lower portions of the lower mantle.

Chapter 3: Conclusions

Substitution of $Al^{3+}_{VIII}Al^{3+}_{VI}O_3$ and $Fe^{2+}_{VIII}Si^{4+}_{VI}O_3$ components into perovskite cause smaller changes in volume than $Fe^{3+}_{VIII}Al^{3+}_{VI}O_3$ substitution. However, the volume data presented in this chapter indicate that $Fe^{2+}_{VIII}Si^{4+}_{VI}O_3$ substitution into an Al-bearing perovskite has a much greater influence on perovskite volume than when perovskite is Al-free. Such a mechanism will make Fe^{2+} substitution into perovskite less favourable with increasing pressure.

Using density and compression data from this chapter in addition to literature data the volume change for the FeO disproportionation reaction,

$$\underset{\text{Perovskite}}{AlAlO_3} + \underset{\text{Mw}}{3FeO} = \underset{\text{Metal}}{Fe} + \underset{\text{Perovskite}}{2AlFeO_3}.$$

is calculated to be –2 cm^3/mol. This implies that the formation of metallic Fe through disproportionation should remain energetically favourable throughout the perovskite-bearing region of the lower mantle.

Chapter 4

A calorimetric study of the $Mg_3(Mg,Si)Si_3O_{12}$(majorite)-$Mg_3Al_2Si_3O_{12}$(pyrope) garnet solid solution

4.1 Introduction

A significant number of experimental studies have been performed to determine the pressures and temperatures of mineral transformations in the mantle in order for them to be compared with seismic velocity observations. However, at pressures greater than 10 GPa most phase equilibria studies suffer from a lack of both precision and accuracy in pressure and temperature determination. In addition, at temperatures compatible with large regions of the mantle the attainment of chemical equilibrium in phase equilibria studies can be difficult if not impossible on realistic time scales. The thermodynamic description of a mineral transformation is, therefore, very important as it can be used to extrapolate experimental data over wide ranges of conditions with good theoretical justification. An effective approach is to fit phase boundaries determined in phase equilibria studies using thermodynamic equations describing the stability of the transforming phases (Akaogi *et al*., 1987; Akaogi *et al.*, 1999). The thermodynamic data that are refined in such a fit are not, however, uniquely determined from a single reaction boundary and the uncertainties in the fitting can be reduced if thermodynamic parameters can be independently determined. Calorimetry is a vital technique for providing independent determinations of thermodynamic parameters, particularly enthalpies and heat capacities. For transformations involving multi-component solid solutions this becomes even more

important because non-ideality of mixing becomes an additional parameter to constrain, that can impart fine topology to phase boundaries. Such topology is on the limit of what can be determined in phase equilibria studies but is still important for the interpretation of seismic reflection data (Stixrude, 1997).

Garnet is a major constituent of the upper mantle, transition zone and the top region of the lower mantle. Over this range of stability, spanning from 2-28 GPa, garnet compositions change significantly as a result of reactions between other phases of the mantle. At shallow upper mantle conditions, garnet is a solid solution with major element substitutions that are described by the formula $(Mg,Fe,Ca)_3Al_2Si_3O_{12}$. However, above approximately 4 GPa substitution of Mg, Fe and Si onto the octahedrally-coordinated Al site occurs causing $MgSiO_3$ and $FeSiO_3$ pyroxene components to dissolve into the garnet structure as majorite components (Ringwood, 1967; Akaogi and Akimoto, 1977; Ringwood, 1991). These transitions can be described by the garnet systems $Mg_3Al_2Si_3O_{12}$-$Mg_4Si_4O_{12}$ and $Fe_3Al_2Si_3O_{12}$-$Fe_4Si_4O_{12}$. There is no evidence that Ca enters the Al site. Ordering of Mg and Si on the octahedral sites leads to a symmetry breaking transition from cubic to tetragonal for garnets with molar $Mg_4Si_4O_{12}$ contents of >80%. Tetragonal garnets are unlikely to exist in the Earth, as Al contents in most mantle rocks are too high; in addition it has been proposed that the ordering transition may occur during temperature quenching, while at mantle temperatures cubic symmetry is attained (Hatch and Ghose, 1989; Heinemann *et al*., 1996).

Thermodynamic data for the garnet-majorite solid solution are particularly important as reaction rates involving garnet are extremely slow (Kubo *et al*., 2002) and equilibrium is therefore very difficult to achieve in phase equilibria experiments. In addition because the pyroxene to garnet transition is smeared out over a large pressure range, thermodynamic parameters describing non-ideality of the garnet solid solution become strongly correlated with volumetric properties describing the effect of pressure on garnet stability. An independent determination of non-ideality of the $Mg_3Al_2Si_3O_{12}$(pyrope)-$Mg_4Si_4O_{12}$(majorite) solid solution by calorimetry would greatly aid the separation of these effects. An important parameter for calculations of the garnet solid solution stability is the enthalpy of the fictive cubic $Mg_4Si_4O_{12}$ garnet end member, which can be obtained if solid solution data on cubic garnets can be extrapolated in composition beyond the cubic-tetragonal transition to the Al-free axis. Currently, however

calorimetric data are insufficient particularly near the cubic-tetragonal transition, to perform this extrapolation reliably.

Previous studies to determine thermodynamic properties of the $Mg_3Al_2Si_3O_{12}$-$Mg_4Si_4O_{12}$ garnet solid solution can be divided into calorimetric studies (Akaogi *et al*., 1987; Yusa *et al*., 1993; Akaogi and Ito, 1999), atomistic calculations (Vinograd *et al*, 2006a; Vinogard *et al*., 2006b) and thermodynamic assessments of phase equilibria data (Gasaprik 2003; Fabrichanaya, 2004). Akaogi *et al*., (1987) and Yusa *et al*., (1993) reported 5 enthalpies of dissolution for $Mg_3Al_2Si_3O_{12}$-$Mg_4Si_4O_{12}$ garnets including both end members using drop calorimetry. These data show the solid solution enthalpies to exhibit nearly ideal behavior and extrapolation to the cubic $Mg_4Si_4O_{12}$ garnet end member gives a solution enthalpy of 1±7 kJ/mol, which is lower than the measured value for the tetragonal end member 20.4±5 kJ/mol. In the recent atomistic study of Vinograd *et al.*, (2006a), however, significant excess properties are reported with large deviations from ideality similar in magnitude to those reported for $Mg_3Al_2Si_3O_{12}$-$Ca_3Al_2Si_3O_{12}$ garnets (Haselton and Newton, 1980). The long range ordering was shown to be a high-temperature feature with disordered $Mg_4Si_4O_{12}$ cubic garnet predicted to be stable only above 3500 K.

In this study we have measured the enthalpy of dissolution of garnet solid solutions in the system $Mg_3(Mg,Si)Si_3O_{12}$-$Mg_3Al_2Si_3O_{12}$ by lead borate drop solution calorimetry under controlled oxygen fugacity. Samples were synthesized using a large volume 5000-ton multianvil press so that large sample volumes ensured that a number of calorimetric drop measurements could be performed on each sample. We use these data to assess the ideality of this solid solution and estimate the enthalpy of solution of the fictive cubic $Mg_4Si_4O_{12}$ garnet end member.

4.2 Starting material synthesis

Glasses of $Mg_4Si_4O_{12}$ and $Mg_3Al_2Si_3O_{12}$ composition were fabricated from mixtures of reagent grade SiO_2, MgO and Al_2O_3 by fusing them in a Pt crucible placed in a 1-atmosphere furnace at 1600-1700°C for durations of 15-30 minutes. The recovered liquids were quenched rapidly by placing the crucible in water. Glasses were then reground and refused to ensure homogeneity, which was checked by analyzing mounted chips using the

electron microprobe. By grinding these two glass compositions in varying proportions seven more glass-starting compositions with 10, 15, 20, 30, 40, and 80 mol% pyrope were prepared.

4.2.1.Piston-cylinder synthesis experiment

$Mg_3Al_2Si_3O_{12}$ pyrope was synthesized at 3 GPa and 1200°C using a piston cylinder apparatus (Boyd and England, 1960). A 1/2-inch talc–pyrex pressure assembly was used for the experiment (Fig. 4.1). This assembly consists of a talc sleeve surrounding a pyrex tube, which acts as the pressure-transmitting medium, and an inner graphite furnace for resistive heating. Finely ground glass powder of pyrope composition was loaded into a platinum capsule that had been previously welded closed at one end, along with 1-mol % water. After loading, the capsule was carefully closed at the other end by welding. The capsule was placed inside the furnace in a sintered Al_2O_3 sleeve with extra space above and below the capsule filled by Al_2O_3 plugs as shown in Fig. 4.1. The assembly was inserted into the pressure chamber of the piston cylinder bomb with a steel piston ring at its base. On the top of the assembly a steel plug was inserted within a pyrophyllite sleeve. A hole in the plug allowed a thermocouple inside an alumina sleeve to be inserted for temperature monitoring. Temperature was measured using WRe75-W3Re type B thermocouple. After the bomb was placed inside the press, pressure was increased to a value 10% below the desired value before the sample was heated to 1200°C. After the final temperature was attained the pressure was raised to 3 GPa. Experiments were heated for durations of 24 hours and quenched by cutting the power to the furnace.

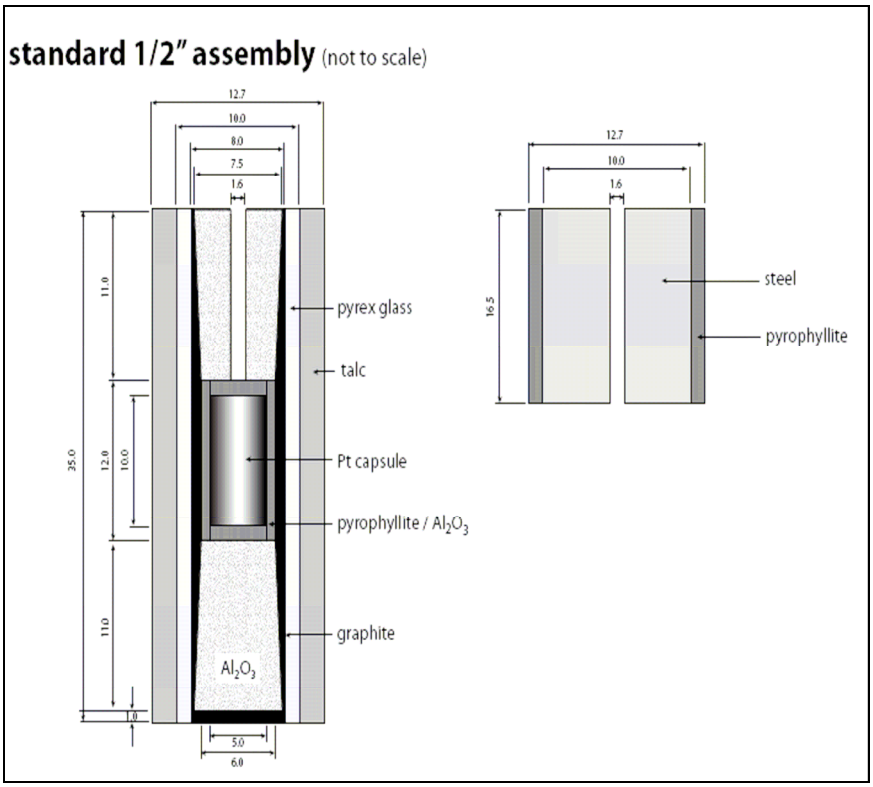

Figure. 4.1: A schematic diagram of ½ inch talc-pyrex piston cylinder assembly (left) and steel pulg (right) used in this study.

4.2.2 Multianvil synthesis experiment

Majoritic garnet compositions were synthesized from glass starting mixtures using a large volume multianvil in conjunction with a 5000-ton press. The specially designed multianvil employs eight 54 mm edge length tungsten carbide anvils, which are compressed with a series of outer hard steel anvils in a split cylinder configuration (Frost *et al*., 2004). 18 mm edge length Cr_2O_3-doped MgO octahedra were used as pressure media with anvil truncations of either 11 mm or 8 mm depending on the pressure range. A box furnace assembly was designed to maximize the sample volume. A schematic diagram of this assembly is shown in Fig. 4.2. The garnet glass powders were packed into Re foil capsules of 3 mm diameter and 3 mm long. Capsules were placed at the center of a cylindrical $LaCr_2O_3$ furnace inside an MgO sleeve. The capsule filled almost the entire length of the furnace with additional disks of $LaCr_2O_3$ closing the furnace top and bottom. The furnace occupies only the central third of the assembly and makes electrical contact with the cubes via cylindrical molybdenum electrodes. A W3%Re-W25%Re thermocouple inside an

MgO ceramic is inserted from one side of the assembly through the molybdenum electrode, so that the junction is located just above the sample. Synthesis experiments were performed between 17-20 GPa and 1000-1600°C (Table 4.1). The pressure calibration curves of Frost *et al*., (2004) were adopted for determination of pressure in our experiments. The heating duration varied from one to three hours and samples were quenched by cutting the power supply to the furnace.

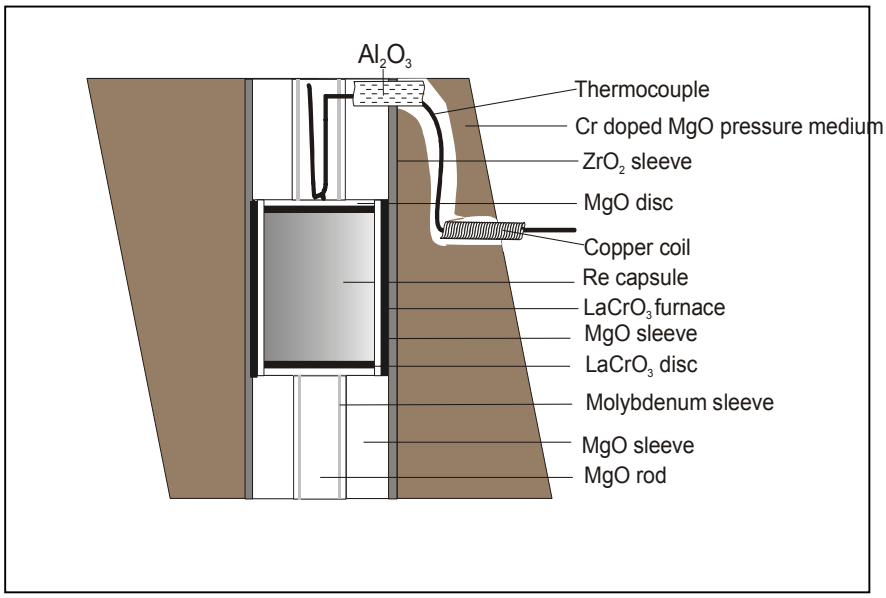

Figure. 4.2: A diagrammatic representation of the box furnace assembly is shown here. The sample was contained in a Re capsule as shown surrounded by a MgO sleeve and a $LaCr_2O_3$ furnace. The molybdenum tubes serve as contacts for heating. This set up ensures low thermal gradient in the large sample volume.

Table 4.1: Synthesis conditions for calorimetric samples used in this study. Piston cylinder and a multianvil press were used to synthesise them. The unit cell parameters determined by powder X-ray diffraction (as discussed later in this section), for garnets are also listed here. Garnets with cubic symmetry have a=b=c and for tetragonal symmetry have a = b ≠ c where a, b, c are crystal axes so, as a and b axes are equal, only, a and c are listed here.

Run no.	Composition	Pressure assembly	Pressure GPa	Temperature °C	Unit cell parameters (in Å units) a-axis	c-axis
Z493	Py 40	18/8	19	1000	11.476	
Z494	Py 20	18/8	19	1600	11.483	
Z496	Py 10	18/8	18	1600	11.497	11.457
Z501	Py 30	18/8	17	1600	11.484	
Z507	Majorite	18/8	19.5	1750	11.517	11.433
Z508	Py 80	18/11	17.5	1200	11.463	
Z525	Py 15	18/8	18	1400	11.482	
PC	Pyrope	1/2inch	3	1200	11.460	

Small chips of the recovered samples were embedded in epoxy resin for quantitative chemical analysis using a JEOL JXA-8200 WD/ED electron microprobe operating in wavelength dispersive mode with a point beam at 15 nA current and 15 kV. Standards employed were andradite for Si, spinel for Al and enstatite for Mg (for details on operating conditions see Table 2.3 of Chapter 2). The determined compositions are listed in Table 4.2.

Table 4.2: The cation composition of the garnet starting materials as analyzed by electron microprobe calculated based on 12 oxygen per formula unit. Abbreviation Maj. (majorite) and Pyr. (pyrope).

Composition	Si	Mg	Al	Total	Maj. content	Pyr. content
Pyrope	3.007	2.974	2.007	7.989	0.007	0.993
Pyrope 80	3.224	3.133	1.611	7.970	0.224	0.776
Pyrope 40	3.606	3.548	0.827	7.980	0.605	0.394
Pyrope 30	3.677	3.689	0.638	8.004	0.677	0.323
Pyrope 20	3.755	3.828	0.442	8.024	0.755	0.245
Pyrope 15	3.867	3.783	0.321	7.972	0.867	0.133
Pyrope 10	3.897	3.846	0.240	7.983	0.897	0.103
Majorite	4.025	3.95	0	7.974	1.025	0

The remaining portion of each sample was ground to a powder and a portion of this powder, which is presumed to have been representative of the entire sample, was characterized by X-ray powder diffraction. The samples were mixed with a small amount of Si as an internal standard (NBS standard number 640b). X-ray diffraction was performed using a Philips X'Pert Pro X–ray diffractometer operating in reflection mode; using Co Kα radiation with an wavelength of 1.78892 Å selected using a focused monochromator. The diffraction conditions were set to a step size of 0.2°, a step time of 1000s with scan speed of 0.0002°/sec with a rotating platform rotating at 1 rotation per second. The data were collected over a 2θ range of 20-120°. Cell parameter refinements were performed using the GSAS software package (see Table 4.1). Obtained Cell parameters are plotted in Fig. 4.3. No phases other than cubic or tetragonal garnet were

detected. The cubic to tetragonal garnet transition was observed at slightly lower pyrope contents (< 13 %) than in the study of Heinemann *et al*., (1997).

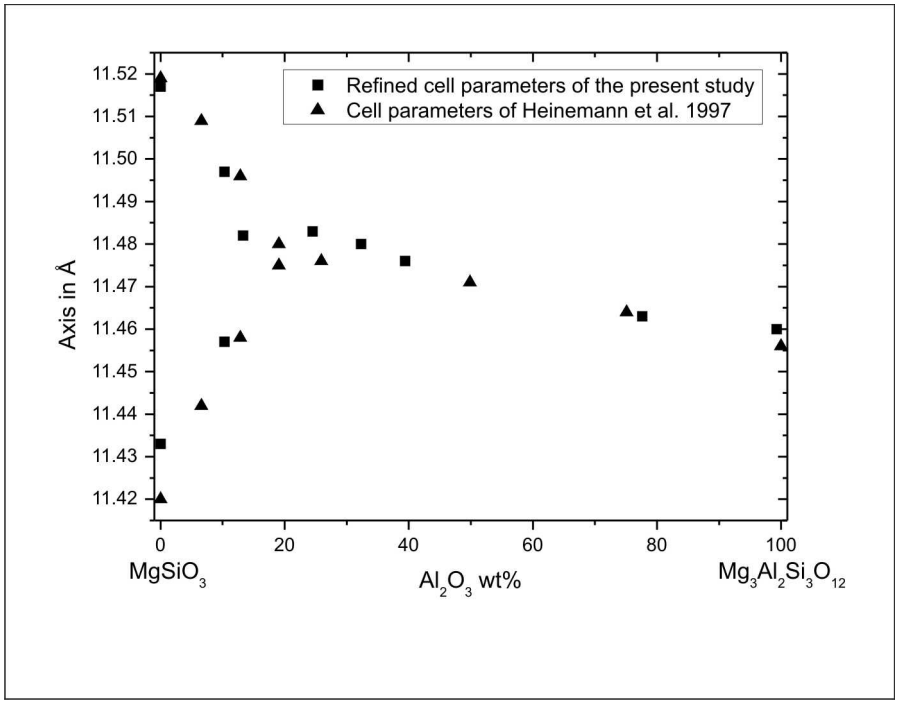

Figure 4.3: Refined cell parameters of the garnet compositions in the majorite–pyrope join after synthesis in multi-anvil and piston cylinder (filled squares). The cell parameters as reported by Heinemann *et al*., 1997 along the majorite–pyrope join are plotted (solid triangles) for comparison. They reported the stability field of tetragonal garnets to commence from the Maj $_{80}$ composition; however our Maj $_{0.867}$ still appears to be a cubic garnet. This discrepancy may be attributed to differences in the synthesis conditions.

4.3 Calorimetric measurements

4.3.1 Basic principals

A calorimeter measures the change in heat associated with the change of state of a sample. A number of calorimetric methods have been employed in Earth sciences to provide basic thermodynamic data. Thermophysical measurements such as low temperature adiabatic calorimetry or differential scanning calorimetry (Akaogi, 1990; Navrotsky, 1997; Navrotsky, 2004) are used to determine heat capacities as a function of temperature, which are also required to determine the standard entropy of a phase. Thermochemical or reaction calorimetry, on the other hand, provides a measurement of the enthalpy of a reaction, which can be combined with other reaction enthalpies to give the heat of formation of a

compound. A widely used type of reaction calorimetry is to measure the heat of dissolution as a sample dissolves in a solvent, either an acid or an oxide melt, to infinite dilution. There are two methods by which this can be accomplished, which deviate with respect to the initial temperature of the sample. In solution calorimetry the initial temperature of the sample is identical to that of the solvent before dissolution. In drop solution calorimetry the sample is initially at room temperature and is dropped into the high-temperature solvent. In this study drop solution calorimetry using an oxide melt was employed. This was deemed more suitable because the recovered metastable high-pressure phases could potentially breakdown during the high temperature equilibration stage (at ~700°C) of solution calorimetry. It should be noted, however, that in previous studies solution calorimenty has been extensively employed to measure solution enthalpies of high-pressure phases (Akaogi *et al*., 1987; Yusa *et al.,* 1993; Akaogi and Ito, 1999).

4.3.2 Enthalpy measurements

A twin calvet type microcalorimeter, based on the design described by Kleppa, (1976), installed at Gakushuin University, Tokyo, was used for our calorimetric measurements. It consisted of two sample chambers each of which was surrounded by a thermopile of Pt-Pt10Rh thermocouples. The thermopiles were connected in opposition inside a massive kanthal block. The block was maintained at 978 K by heaters situated outside of the block (Fig. 4.4). The e.m.f. from the thermopile after amplification was recorded using an electronic integretar, which gave a graphical representation of the heat flow of the experiment (see Fig. 4.6) and a numerical value of the area under calorimetric peak after processing.

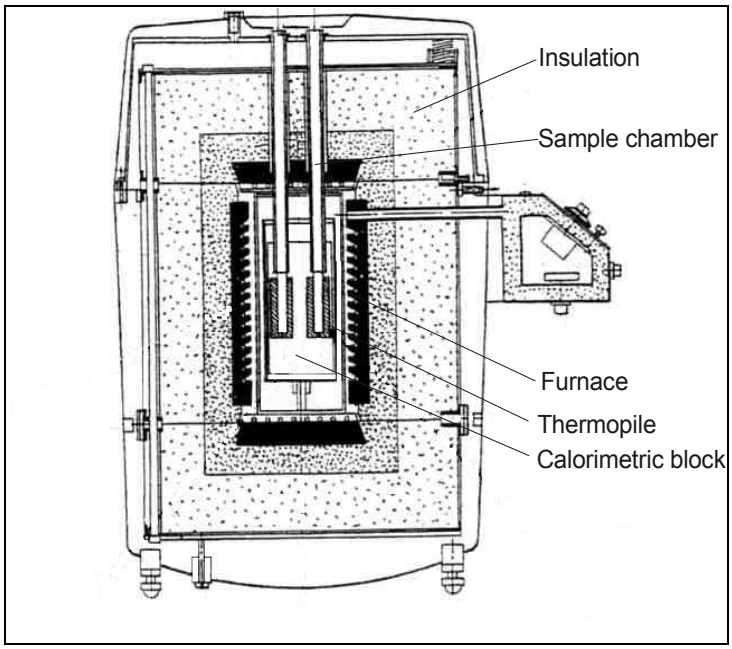

Figure. 4.4 A Twin Calvet type microcaloirmeter of the type described by Kleppa, (1976) as used in this study.

$2PbO.B_2O_3$ was used as the solvent in our experiments. A single batch of solvent was made by mixing PbO and H_3BO_3 in a 1:1 molar proportion. The mixture was initially heated in a 1-atmosphere furnace at 1073 K for 30 minutes. The quenched glass was rehomogenised by grinding and remelted at 1323 K for one and half hours to ensure dehydration (Charlu *et al*., 1975).

For each experiment 5 grams of $2PbO.B_2O_3$ glass were measured into each of two Pt tubes, one for each sample chamber of the calorimeter, and melted in a furnace at 700°C for an hour. Each tube was placed into one of the calorimeter sample chambers housed in a second Pt tube jacketed by a silica glass tube inside an inconel tube. The inconel tube was inserted into the calorimeter prior to the beginning of each experiment and was allowed to reach thermal equilibrium as indicated by a stable base line from the thermopiles. Ar gas was bubbled through the solvent at a flow rate of 5 cm^3/minute in order to hasten dissolution by stirring as shown in Fig. 4.5. The sample pellets of about 3 mg weight were made using a miniature pellet press and were dropped from room temperature into the $2PbO.B_2O_3$ solvent at 978 K. Drops were alternated between the two samples chambers. Heat was either absorbed or liberated during the reaction and the thermopiles detected the change of temperature between the sample chamber and the kanthal block. The liberated

heat gives rise to a calorimetric peak, which dies out exponentially to the original baseline with time as heat is transferred from the sample chamber to the block (Fig. 4.6). The recorded heat change is equal to the heat content of the sample plus the enthalpy of solution at the temperature of the calorimeter. The pyrope-rich samples were dissolved within an hour of dropping into the solvent; however, the majorite rich compositions required approximately 1.5 hours for complete dissolution. When the calorimetric peak dies out and gets back to the original base line the sample is considered to be totally dissolved.

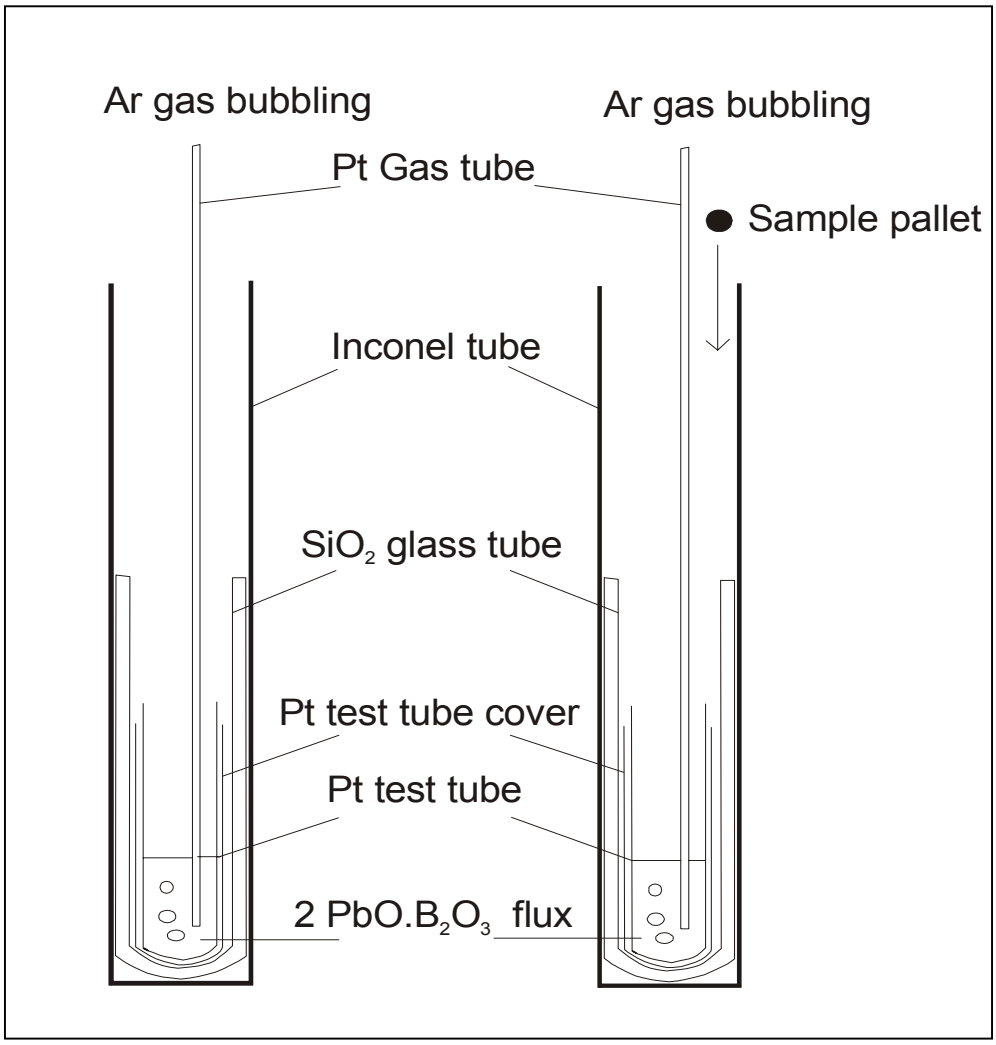

Figure 4.5: A schematic diagram showing the set of the sample chambers used for drop solution calorimetric technique. Ar gas was bubbled through the sample chambers for hastening dissolution.

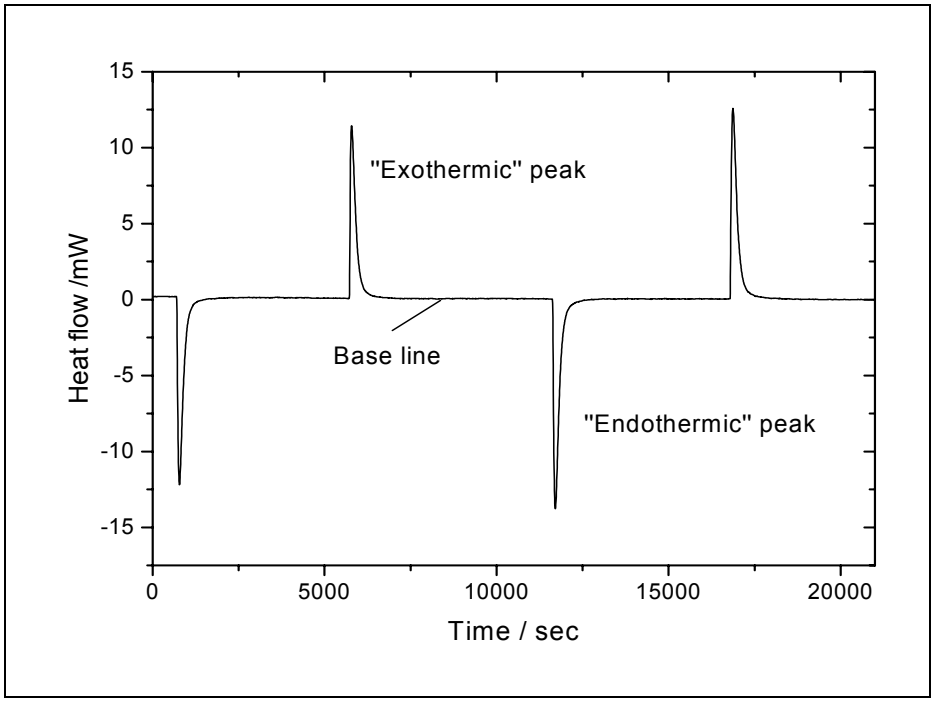

Figure 4.6. A drop solution calorimetric curve of the pyrope composition showing the evolving heat of dissolution as a function of time. Each peak represents a drop solution run and are marked exothermic and endothermic peaks for distinction of heat flow values obtained from left and right sample chambers of the calorimeter (see Fig. 4.4). By integrating the area under the peaks, heat of dissolution associated with each run is determined.

The heat effect is proportional to the area under the calorimetric peak but the proportionality factor must be calibrated. This calibration factor was determined for each sample chamber using Al_2O_3 as a known standard. Pellets of Al_2O_3 of approximately 3 mg were dropped into 5 gm of lead borate solvent. The integrated heat content of Al_2O_3 dissolution was compared with the standard $\Delta H^{d\text{-}sol}$ of Al_2O_3 of 106.73 kJ/mol to give calibration factors of 0.875 $\pm$ 0.01 J/mol for the left-side and 0.896 $\pm$ 0.01 J/mol for the right-side sample chambers (Table 4.3).

Table 4.3: Calibration factor calculation using Al_2O_3 pellets. (Abbreviations: observed H is the observed heat, ΔH is the enthalpy of solution and S is the calibration factor).

Left Side

Run No.	Al_2O_3 mass / g	Al_2O_3 /mol	Observed H / J	Observed H/ KJ	ΔH of Al_2O_3 / KJ.mol^{-1}	S
1	0.003253333	3.1908E-05	3.0124	0.0030124	94.41003578	**0.884568873**
2	0.003303333	3.2398E-05	3.0242	0.0030242	93.34524406	**0.874592374**
3	0.00337	3.3052E-05	3.0815	0.0030815	93.23229125	**0.87353407**
4	0.003186667	3.1254E-05	2.9089	0.0029089	93.07354171	**0.872046676**
5	0.00346	3.3935E-05	3.1445	0.0031445	92.66368916	**0.868206588**
6	0.003286667	3.2235E-05	3.0253	0.0030253	93.8527221	**0.879347157**
7	0.003333333	3.2692E-05	3.1171	0.0031171	95.34678993	**0.893345732**
8	0.0034	3.3346E-05	3.061	0.003061	91.79488853	**0.860066416**
					Average calibration factor	**0.875713486**

Right side

Run No.	Al_2O_3 mass / g	Al_2O_3 /mol	Observed H / J	Observed H/ KJ	ΔH of Al_2O_3 / KJ.mol^{-1}	S
1	0.00325	3.1875E-05	3.0643	0.0030643	96.13510532	**0.900731803**
2	0.003526667	3.4588E-05	3.3203	0.0033203	95.99464319	**0.899415752**
3	0.003216667	3.1548E-05	3.0454	0.0030454	96.53223712	**0.904452704**
4	0.003353333	3.2888E-05	3.1942	0.0031942	97.12241338	**0.909982323**
5	0.00328	3.2169E-05	3.0046	0.0030046	93.40000628	**0.875105465**
6	0.00344	3.3738E-05	3.2499	0.0032499	96.32646916	**0.902524774**
7	0.00339	3.3248E-05	3.2332	0.0032332	97.24492779	**0.911130214**
8	0.003306667	3.2431E-05	3.0598	0.0030598	94.34887131	**0.883995796**
9	0.00325	3.1875E-05	3.0179	0.0030179	94.67941597	**0.887092813**
10	0.00316	3.0992E-05	2.9567	0.0029567	95.40129389	**0.893856403**
					Average calibration factor	**0.896828805**

4.4 Results

The measured drop solution enthalpies ($\Delta H^{d\text{-}sol}$) of majorite-pyrope garnets are reported in Table 4.4. Due to the size of the synthesized samples a number of drops of approximately 3 mg each could be performed for each sample and the final $\Delta H^{d\text{-}sol}$ is therefore the average of between 3-6 drops.

Table 4.4: Drop solution enthalpies of $Mg_3(Mg,Si)Si_3O_{12}$ (majorite)-$Mg_3Al_2Si_3O_{12}$ (pyrope) solid solution join in $2PbO.B_2O_3$ at 978K, where Py_x is the pyrope composition determined from electromicrprobe, $\Delta H^{d\text{-}sol}$ is the enthalpy of dissolution.

Mass (g)	**$\Delta H^{d\text{-}sol}$ (kJ /mol)**	**Mass (g)**	**$\Delta H^{d\text{-}sol}$ (kJ /mol)**
$Py_{0.993}$		$Py_{0.776}$	
0.00270	406.6921	0.00259	344.5220
0.00251	420.5045	0.00278	344.6312
0.00296	396.3194	0.00282	358.7211
0.00253	388.5248		
0.00313	400.6793		
0.00281	405.9892		
	Av. 403.118 ± 8.085		Av. 349.291 ± 8.166
$Py_{0.394}$		$Py_{0.323}$	
0.00296	307.8711	0.00262	290.4055
0.00287	308.38	0.00255	286.598
0.00273	308.292	0.00281	292.6601
0.00261	292.6617	0.00270	303.6652
0.00273	291.9788	0.00289	294.4718
0.00273	301.6067		
	Av. 301.798 ± 5.796		Av. 293.472 ± 5.083

Mass (g)	**$\Delta H^{d\text{-}sol}$ (kJ /mol)**	**Mass (g)**	**$\Delta H^{d\text{-}sol}$ (kJ /mol)**
$Py_{0.245}$		$Py_{0.133}$	
0.00261	214.3883	0.00299	252.4929
0.00256	230.8846	0.00268	241.8
0.00256	222.8271	0.00260	237.4546
0.00264	232.6677	0.00258	247.6614
0.00253	221.0675		
	Av. 224.3688 ± 5.989		Av. 245.8522 ± 7.131
$Py_{0.103}$		Maj	
0.00257	281.2224	0.00257	244.5810
0.00261	265.012	0.00261	245.6691
0.00276	260.9722	0.00276	234.0641
0.00289	260.8478	0.00279	254.2783
0.00283	266.1986	0.00283	212.1408
	Av. 266.251 ± 6.881		Av. 238.146 ± 12.968

The enthalpies of dissolution are plotted in Fig 4.7. The data show a negative deviation from a straight line joining the two end members. This implies that the mixing properties of the solid solution deviate positively from ideality. From the pyrope end member the

enthalpies decrease non linearly with decreasing pyrope content, however, between a pyrope content of 0.32 and 0.24 a strong break in slope occurs and enthalpies start to increase before a final decrease occurs at the majorite end member.

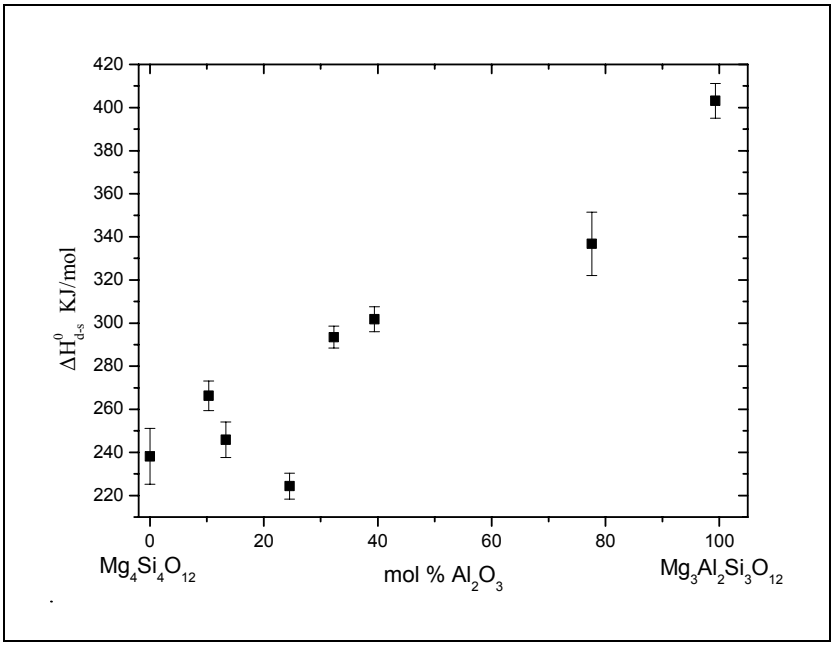

Figure. 4.7: Enthalpies of dissolution of $Mg_3(Mg,Si)Si_3O_{12}$-$Mg_3Al_2Si_3O_{12}$ garnets in $2PbO.B_2O_3$ solvent at 978K.

The drop dissolution enthalpy ($\Delta H^{d\text{-}sol}$) can be written as,

$$\Delta H^{d-sol} = \Delta H^{sol} + \int_{298}^{978} Cp.dt \qquad (1)$$

where, ΔH^{sol} is the enthalpy of solution and the integral term accounts for the change in heat required to raise the temperature of the sample from room temperature to that of the solvent. Values for the integral term are 298 kJ/mol for pyrope (Robie *et al*., 1978) and 297 kJ/mol for majorite (Yusa *et al*., 1993) and it is assumed that this value varies linearly across the solid solution. The uncertainty in this correction is of the order of 1 kJ/mol. Values of ΔH^{sol} are more useful for comparing with previous measurements and for calculating enthalpy changes for mineral reactions.

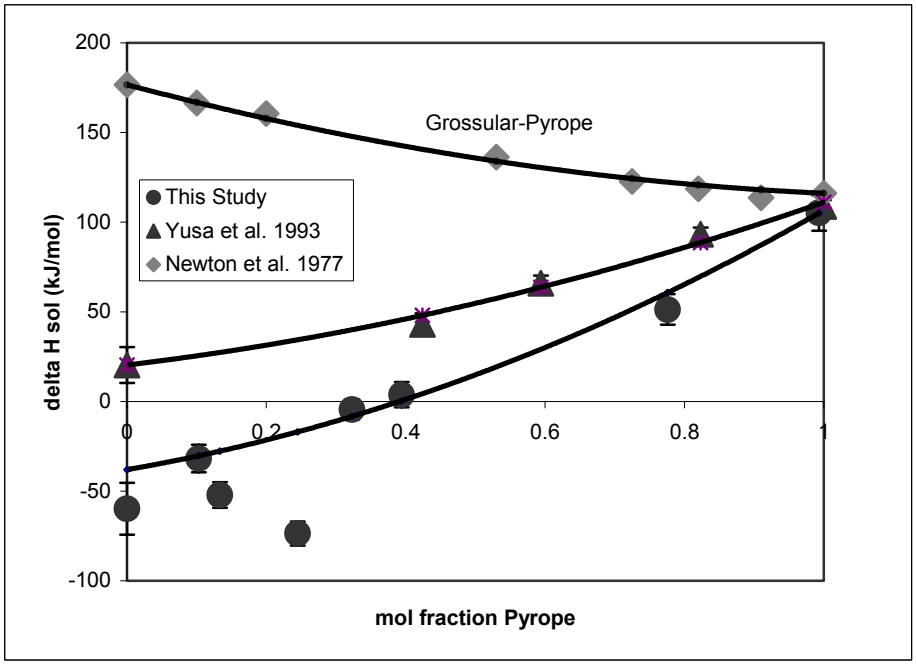

Figure 4.8: The ΔH^{sol} of $Mg_3(Mg,Si)Si_3O_{12}$-$Mg_3Al_2Si_3O_{12}$ garnets determined in this study compared with the results of Yusa *et al*., (1993) for the same solid solutions and results of Newton *et al*., (1977) for the $Ca_3Al_2Si_3O_{12}$-$Mg_3Al_2Si_3O_{12}$ (grossular-pyrope) solid solution. Symmetric solution fits have been made to all data, excluding data with X pyrope <0.3 for this study.

Fig. 4.8 shows ΔH^{sol} at 978 K calculated from values of $\Delta H^{d\text{-}sol}$ using equation (1). Also shown are data on the same solid solution from Yusa *et al., (*1993), for which solution calorimetry was employed, and data on the $Ca_3Al_2Si_3O_{12}$-$Mg_3Al_2Si_3O_{12}$ grossular-pyrope solid solution from Newton *et al*., (1977) that also employed solution calorimetry. The data from this study deviate significantly from values reported by Yusa *et al.,* (1993). Although values determined for the pyrope endmember are in excellent agreement, with decreasing pyrope content the enthalpies decrease much more strongly in this study and values for the majorite end member are approximately 80 kJ/mol lower.

4.5 Discussion

The strong change in slope exhibited by the data at pyrope contents < 30 % may be related to the cubic/tetragonal phase transformation and therefore to long range ordering of Si and

Mg on the octahedral site. However, there tetragonal symmetry was not detected in the X-ray diffraction analyses of the 25 % pyrope sample and in fact clear tetragonal splitting was observed only in the sample with 10 % pyrope. The 25 % pyrope sample appears to be particularly anomalous and one possibility is that the sample contained some contaminant. However, all samples were ground entirely and, while only a portion of the powder was then analyzed with x-ray diffraction, this powder should have been representative of the entire sample and no peaks corresponding to a contaminant were detected. Interestingly, the most likely contaminant, pyroxene, would have driven the enthalpies in the opposite direction. Although further study is required it seems likely that the changes in slope at pyrope contents <30 % results from different states of order in the recovered samples. As the samples were synthesized at different conditions variations in the state of order may have occurred. In addition because large multianvil assemblies were used to produce significant sample volumes the cooling rates during quenching could have been slower compared with those in smaller assemblies used by Yusa *et al.,* (1993).

The data at pyrope contents >30% fall on a single curve even through they were also synthesized over a range of conditions. It seems unlikely that the deviation between these data and those of Yusa *et al*., (1993) also results from ordering, as the proportion of Si and Mg cations on the octahedral sites is small and pyrope concentrations are far away from the cubic tetragonal transition. A further possibility is that the deviation from the data of Yusa *et al.,* (1993) results from their use of solution calorimetry where the sample is first equilibrated at 978 K for many hours before dropping it into the solvent. Back reaction or amphorphisation during this stage would have raised the determined enthalpies. Without further study, however, this is hard to demonstrate conclusively.

The excess enthalpy of mixing H^{xs} can be calculated using Thompson's (1967) symmetric regular solution model for the garnet solid solutions in the system $Mg_3(Mg,Fe)Si_3O_{12}$-$Mg_3Al_2Si_3O_{12}$.

We have,

$$\Delta H_{d-s}^{calc} = \Delta H_{sol}^{ideal} - \Delta H^{XS} \qquad (2)$$

where, $H^{XS} = 2W_H X_{Maj}(1-X_{Maj})$ (3)

and

$$\Delta H_{d-s}^{ideal} = X_{maj}\Delta H_{sol}^{Maj} + (1 - X_{Maj})\Delta H_{sol}^{Pyr} \quad (4)$$

where, X_B is the mole fraction of the pyrope component and W_H is the interaction parameter for mixing on one cation site i.e., (Mg,Si)↔ Al and ΔH_{Sol}^{Pyrope} and ΔH_{Sol}^{Maj} are the enthalpies of drop solution of the pyrope garnet and the majorite garnet respectively. Fitting the Yusa *et al*., (1993) data in this way and refining ΔH_{Sol}^{Maj} and W_H gives values of 20 kJ/mol and 22 kJ/mol respectively. The fitting of data from our study can be performed in a number of ways, depending on assumptions made ΔH_{Sol}^{Maj} for the value of ΔH_{Sol}^{Maj}. If only data with pyrope contents >30 % are employed and both and W_H are refined, values of 3 and 88 kJ/mol are obtained respectively, while if we assume the measured ΔH_{Sol}^{Maj} from this study of –59 kJ/mol and refine only W_H we obtain a value of 11 kJ/mol for the later. However, with this second approach the fit to the data at >30% pyrope is quite poor as all curvature is removed. These two fits demonstrate the two possible conclusions that either $Mg_3(Mg,Si)Si_3O_{12}$-$Mg_3Al_2Si_3O_{12}$ garnet enthalpies deviate strongly from ideality or that the enthalpy of the fictive cubic $Mg_3(Mg,Si)Si_3O_{12}$ garnet is much lower than previously estimated. The first conclusion provides a much better fit to the data and a compromise between the two conclusions can be obtained by refining W_H for the highest value of ΔH_{Sol}^{Maj} that still fits within the error bars of all data with pyrope contents >30 %. This fit, shown in Fig. 4.8 results in values for ΔH_{Sol}^{Maj} and W_H of –37 kJ/mol and 38 kJ/mol respectively. For comparison the grossular-pyrope solid solution that is often considered one of the more non-ideal garnet solid solutions has a single site W_H of 14 kJ/mol. Fig. 4.9 shows excess enthalpies from this study compared with the fit shown in Fig. 4.8 and the fit for the data of Yusa *et al*., (1993).

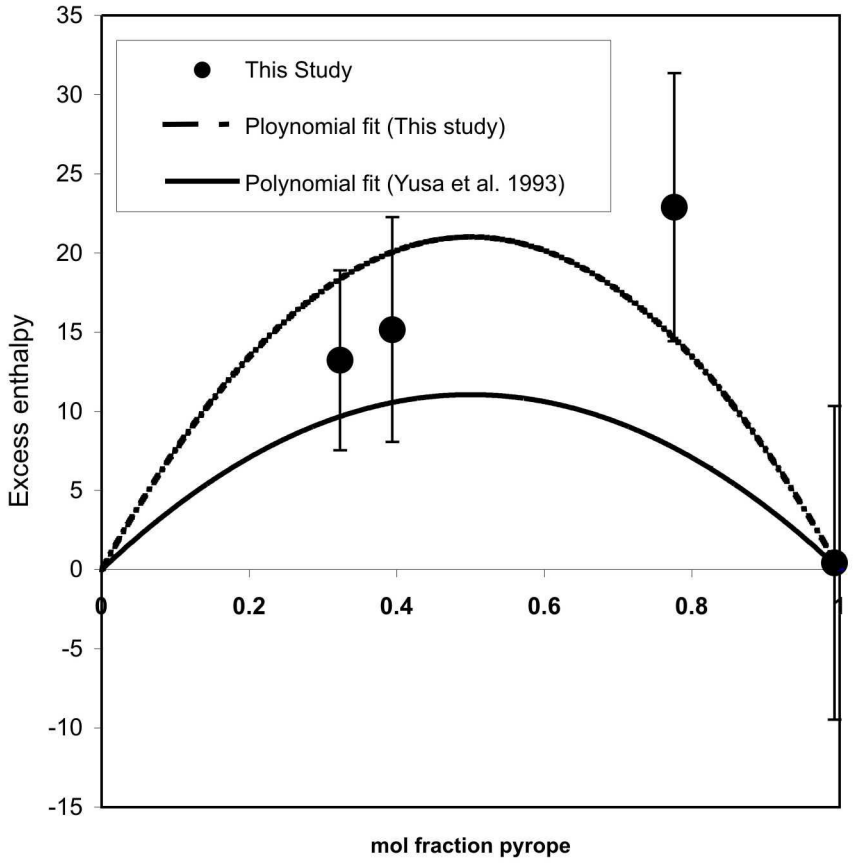

Figure 4.9: Excess enthalpies of mixing for garnet solid solutions. Polynomial fit shown for this study is the same as that indicated in Fig 4.8 with W_H = 38 kJ/mol and a solution enthalpy of the fictive cubic $Mg_4Si_4O_{12}$ garnet of –37 kJ/mol. The best polynomial fit through the Yusa *et al*., (1993) data are shown for comparison.

4.6 Conclusions

In this chapter enthalpies of drop solution have been measured for $Mg_3(Mg,Si)Si_3O_{12}$-$Mg_3Al_2Si_3O_{12}$ garnets which have been found to be substantially lower than estimates from previous studies. Scatter in the data for garnets with low pyrope contents (<30 %) may result from varying states of Mg, Si ordering in the synthesized samples. However not all variations can be explained in this manner and the data imply that there is either a large positive enthalpy of mixing in this solid solution or that the enthalpy of the fictive $Mg_4Si_4O_{12}$ cubic garnet end member is substantially lower than previously determined. The first possibility provides a better fit to the experimental data although a compromise

between these two possibilities is more likely. Significant deviations from ideality for $Mg_3(Mg,Si)Si_3O_{12}$-$Mg_3Al_2Si_3O_{12}$ garnets have been proposed based on atomistic calculations (Vinograd *et al*., 2006) and the possibility that previous solution calorimetry measurements suffered from thermal relaxation or back reaction (Yusa *et al*., 1993) makes this a realistic possibility. Aside from performing more measurements to verify these results, to employ these data at mantle temperatures requires information on the excess entropy term W_S because $W_G = W_H - TW_S$. In the past W_S has been considered to be ideal for this solid solution, however deviations from ideality observed for W_H are most likely also reflected in W_S, which can be determined from heat capacity measurements on $Mg_3(Mg,Si)Si_3O_{12}$-$Mg_3Al_2Si_3O_{12}$ garnets.

Chapter 5

Conclusions

The work in this thesis has been performed in order to interpret seismic observations of the mantle and understand them in terms of possible chemical variations. For this purpose a number of mantle properties have been studied as a function of plausible chemical variation. In the Earth's transition zone such variation may result from the accumulation of subducted oceanic crustal material causing Ca and Al enrichments. In the lower mantle, primordial material may be Fe rich or subducted material may form magnesium silicate perovskite, which is Fe and Al rich. By studying the effects of chemical variation on phase stabilities and elastic properties we can compare synthetic models based on the results with seismic data for sound velocities or seismic discontinuity depths.

In this thesis it has been demonstrated that the formation of Ca-perovskite may cause a high-pressure branch to be observable in the 520 km seismic discontinuity, which is normally associated with the wadsleyite to ringwoodite transition. Significant constraints can, therefore, be placed on mantle composition by studying the formation reaction of Ca-perovskite from majorite garnet in high-pressure and high-temperature experiments using various bulk mantle compositions. A thermodynamic approach was adopted to model this reaction in order to extrapolate our experimental results over the entire range of plausible mantle temperatures and compositions. The experimental and thermodynamic modeling results show that the formation of Ca-perovskite from majorite garnet occurs as a non-linear function of depth. Therefore, a significant amount of calcium perovskite will be formed over a narrow depth interval in the mantle. Calculation of the sound velocities for

this exsolution reaction at mid-transition zone conditions, using mineral physics data, show that the impedance contrast for the initial perovskite exsolution is of a suitable magnitude to cause a discontinuity. Therefore, coupled with the wadsleyite-ringwoodite transition, two discontinuities are, possible and are consistent with the observed split in the 520 km seismic discontinuity. However, why the discontinuity should appear split in some regions of the Earth and not in others is shown not to be a function of temperature. Although temperature would tend to merge the two discontinuities together it would do so only at depths much deeper than where a single discontinuity is actually observed. What is more likely is that a single discontinuity is observed in regions where the Ca content of the mantle is low but in regions rich in Ca, such as those containing significant recycled oceanic crust, two discontinuities would be observed. Our findings allow regional seismic observations of this splitting in the 520 km discontinuity to be used as a probe for this major type of mantle heterogeneity in the mantle. This study is, therefore, the first report of a deep mantle seismic discontinuity, which can be used as a sensitive indicator of mantle chemical heterogeneity.

Changes in the elastic properties of magnesium silicate perovskite have been examined as a function of the incorporation of ferric Fe and Al in the structure, using diamond anvil cell compression and single-crystal X-ray diffraction techniques. Compression experiments on Al-and Fe-bearing magnesium silicate perovskites show that Fe and Al incorporation makes the magnesium silicate perovskite structure more compressible. The Al^{3+} and Fe^{3+} substitution in magnesium perovskite will mostly occur via a coupled substitution mechanism at mantle conditions; however at low trivalent cation concentrations a small proportion of oxygen vacancies may form. A third order Birch–Murnaghan fit of the compression data yields a bulk modulus which decreases from 243 to 234 GPa with increasing Fe and Al content with a rise in K' from 5 to 6.5, which can be attributed to an increase in polyhedral compressibility. On consideration of the effects of possible substitution mechanisms on molar volumes of Al-and Fe-bearing magnesium silicate perovskite, it has been observed that in magnesium silicate perovskites existing at lower mantle conditions the substitution of the $Fe^{2+}_{VIII}Si^{4+}_{VI}O_3$ component will be energetically less favoured. Our results show that disproportionation of Fe is energetically favorable in the lower mantle conditions which would result in the enrichment of Fe^{3+} at lower mantle conditions.

Slow kinetics of silicate reactions inhibits the attainment of equilibrium under feasible experimental conditions at lower temperatures. Consequently, the experimental results are generally extrapolated to lower temperatures using suitable thermodynamic models. Uncertainties in such models can be reduced considerably, if thermodynamic parameters used for such fits are independently determined as has been done in our study of the pyrope-majorite solid solution using the drop solution calorimetric technique. Enthalpies of solution along the majorite–pyrope join obtained from drop solution calorimetry show a significant deviation from ideality. The enthalpy of dissolution decreases non-linearly for compositions below 30mol% pyrope due to a symmetry change from cubic to tetragonal. The values of drop solution enthalpies on majorite–pyrope join are significantly lower than previous estimates. An estimation of the excess properties using a symmetric regular solution model gives a value of W_H {interaction parameter of mixing on one cation site in garnet i.e., (Mg,Si)↔Al} of 38 kJ/mol and a solution enthalpy of the fictive cubic majorite garnet of –37 kJ/mol. This would mean a large positive enthalpy of mixing along this solid solution join.

This thesis work emphasizes how a combination of complimentary experimental techniques can lead to a robust assessment of the deep interior of the Earth and contributes to a better understanding of the evolution of the Earth.

Further work

During the course of this thesis a number of points have become obvious where further experimental studies would benefit our understanding of the silicate perovskite forming reactions.

A correlation was observed between the seismically determined geographical distribution of the split 520 km discontinuity with modern and past subduction zones as mentioned in chapter 2. This supports our idea of Ca-enrichment in the mantle via subduction of oceanic crust, which would lead to the formation of Ca-perovskite causing the second discontinuity in the 520 km region. So, further geophysical studies into the splitting and variability of the 520 km seismic discontinuity combined with our interpretation will allow us to scale lateral distribution of mantle heterogeneity on a variety of scales and will provide significant insights into the circulation of subducted oceanic lithosphere in the mantle. Furthermore as the oceanic basalt bulk compositions are rich in

the SiO_2 component, additional phase equilibria studies involving the formation of Ca-perovskite from Ca_2SiO_4 and $CaSi_2O_5$ will lead to better constraints on the thermodynamic modeling of the Ca-perovskite forming reaction. As very little thermodynamic data exist for calcium silicate perovskite, another important aspect will be to collect high quality calorimetric data on Ca_2SiO_4 and $CaSi_2O_5$ to aid in the calculation of calcium perovskite thermodynamic properties from its formation reaction.

Our study of the equation of state of Al- and Fe-bearing magnesium silicate perovskite single crystals was performed at ambient temperature up to pressures of 10 GPa. It was observed in our study that even though a K' value greater than 4 was obtained from our results, a calculation of K_T for lower mantle conditions with a K' = 4, provides a better fit to the predicted lower mantle bulk modulus. Given this discrepancy, it is necessary to extend the equation of state study to pressure-temperature range relevant for mantle conditions in order to better quantify the changes in elastic property at those conditions due to Al and Fe incorporation in the magnesium silicate structure. This will be possible, using a gas loading of the diamond anvil cell for compression experiments, which would provide hydrostatic conditions to higher pressures. In addition, a powder x-ray diffraction equation of state study could be carried out using a high intensity synchrotron X-ray source, in case of failure in producing suitable single crystals. Another important objective would be to carry out crystal structural refinement studies using single crystal X-ray diffraction, provided we can synthesize single crystals of suitable size possibly twin-free, for a better understanding of the substitution mechanism of cations in different crystal structural sites.

For the calorimetric measurements on the pyrope–majorite join, it will be important to reproduce the heat of dissolution data for the majorite-rich compositions, where a strong scatter in data has been observed by our study, in order to confirm whether there is an effect of ordering of Mg and Si on the octahedral site related to synthesis conditions. A thorough assessment of the ordering of Mg and Si for the majorite-rich compositions can be carried out using a Raman spectroscopic study or a ^{27}Al-NMR study on these majorite-rich compositions. In addition, in order to employ our thermodynamic data at mantle temperatures, information on the excess entropy term will be required. This can be determined by heat capacity measurements along the majorite–pyrope join by employing differential scanning calorimetry or the recently-devised PPMS (Physical Properties Measurement System) calorimetric technique.

Appendix A

Table A.1: Details of run numbers and phases observed. Abbreviations: Pd (peridotitic composition), Baslt (basaltic composition), Pyr (pyrope composition), Fo (forsterite composition), Pd gt (perdotitic garnet), Baslt gt. (basaltic garnet), Pyr gt (pyrope garnet), Maj gt (majoritic garnet), Ca-Pv (calcium perovskite), Al–phase (a non-stoichometric unknown phase with Al), Ring (ringwoodite), Mw (magnesiowüstite), Stish (stishovite), Oliv (olivine), Pyrx.(pyroxene), Peri (periclase),Wad (wadsleyite), Pd (peridotite), Pv (perovskite),Ca-Pd ,Ca-Baslt, (all Ca bearing reversal compositions), Ca-Pd gt, Ca-baslt Gt.(reversal phases with Ca)

Run no.	Pressure (GPa)	Starting compositions	Phases observed
1400°C			
H2375	17.9	Pd, Baslt, Pyr, Fo_{20}	Pd gt + Ca-Pv, Baslt gt +Ca-Pv, Pyr gt + Ca-Pv, Ring + Mw + Stish.
S3611	18.1	Pd, Baslt, Pyr, Fo_{20}	Pd gt + Ca-Pv, Baslt gt +Ca-Pv, Pyr gt + Ca-Pv, Ring + Mw + Stish
S3614	18.6	Pd, Baslt, Pyr, Fo_{20}	Pd gt + Ca-Pv, Baslt gt +Ca-Pv, Pyr gt + Ca-Pv, Ring + Mw + Stish
H2370	19.5	Pd, Baslt, Pyr, Fo_{20}	Pd gt + Ca-Pv, Baslt gt +Ca-Pv, Pyr gt + Ca-Pv, Ring + Mw + Stish
H2241	19.6	Pd, Baslt, Pyr, Fo_{20}	Pd gt + Ca-Pv, Baslt gt +Ca-Pv, Pyr gt + Ca-Pv, Ring + Mw + Stish
1600°C			
S3460	18.	Pd, Baslt, Maj, Fo_{90}	Pd gt + Ca-Pv, Baslt gt, Maj gt + Ca-Pv, Wad
S3470	18.8	Pd, Baslt, Pyr, Fo_{30}	Pd gt + Ca-Pv, Baslt gt + Ca-Pv Pyx + Wad
S3550	19.2	Pd, Baslt, Pyr, Fo_{30}	Pd gt + Ca-Pv, Baslt gt + Ca-Pv Pyr Gt + Ca-Pv, Ring + Mw + Stish
S3548	19.5	Pd, Baslt, Fo_{30}	Pd gt + Ca-Pv, Baslt gt + Ca-Pv, Ring + Mw + Stish
S3547	19.5	Pd, Baslt, Fo_{30}	Pd gt + Ca-Pv, Baslt gt + Ca- Pv, Ring + Mw + Stish
S3549	19.9	Pd, Baslt, Pyr, Fo_{30}	Pd gt + Ca-Pv, Baslt gt + Ca-Pv Pyr Gt, Ring + Mw + Stish
S3657	19.9	Baslt, $F0_{90}$ + Baslt, Fo_{30}	Baslt gt + Ca-Pv, Baslt gt + Ca-Pv + Oliv, Mw + Pyrx + Stish + Wad
S3655	19.9	Baslt, $F0_{90}$ + Baslt	Baslt gt + Ca-Pv, Baslt gt + Ca-Pv + Oliv.
S3551	20.4	Pd, Baslt, Pyr, Fo_{30}	Pd gt + Ca-Pv, Baslt gt + Ca-Pv Pyr Gt + Ca-Pv, Ring + Mw + Stish
S3757	20.7	Pd, Baslt, Fo_{30}; Fo_{50}	Pd gt + Ca-Pv, Baslt gt + Ca-Pv,

			Ring + Mw + Stish, Ring + Mw + stish
S3480	22.1	Pd, Baslt, Pyr, Fo_{30}	Pd gt+ Ca-Pv +Al –Phase, Baslt gt, + Ca-Pv + Al phase, Ring +Stish
S3764	21.2	Pd, Baslt, Fo_{30}	Pd gt + Ca-Pv, Baslt gt + Ca-Pv, Ring + Mw + Stish
S3498	21.4	Pd, Baslt, Pyr, Fo_{30}	Pd gt + Ca-Pv, Baslt gt + Ca-Pv Pyr gt + Al phase+ Ca-Pv, Ring + Mw + Stish
S3783	22.3	Pd, Baslt, Maj, Fo_{70}	Pd gt +Ca-Pv, Baslt gt + Ca-Pv, Ring + Mw + Stish + Pyrx.
S3484	22.3	Pd, Ca-Baslt, Pyr, Fo_{30}	Pd gt +Ca-Pv + Peri, Ca-Baslt gt + Ca-Pv, Pyr gt + Ca-Pv, Ring + Mw
S3475	22.6	Pd, Baslt, Pyr, Maj	Pd gt + Ca-Pv, Baslt gt + Ca-Pv, Pyr Gt + Ca-Pv, Maj gt + Ca-Pv
S3478	23	Pd, Baslt, Fo_{30}	Pd gt + Ca-Pv, Baslt gt + Ca- Pv, + Gt + Ca-Pv, Pv + Mw + Stish
S3784	23.5	Pd, Ca-Baslt, Fo_{70}, Pd	Pd gt +Ca-Pv, Ca-Baslt gt + Ca-Pv Mw + Pv, Stish + Mw +Pv + Cor

Reversals (1600°C)

S3538	17.95	Baslt, Ca Baslt, Fo_{30}	Baslt gt + Pyx, Ca-Pd gt + Ca-Pv, Pyx + Wad
S3543	18.4	Baslt, Ca Baslt, Fo_{30}	Baslt gt + Pyx, Ca-Pd gt + Ca-Pv Pyx +Wad +Mw
S3515	19.8	Baslt, Ca Baslt, Fo_{30}, Fo_{98}	Baslt gt + Ca-Pv, Ca-Baslt gt + Ca-Pv, Ring +Wad + Mw, Wad
S3521	20.7	Pd, Ca Pd, Fo_{30}	Pd gt +Ca-Pv, Ca-Pd gt + Ca-Pv Ring + Mw
S3523	20.8	Pd, Ca-Pd, Ca-Baslt, Fo_{30}	Pd gt + Ca-Pv + Al-phase +Ca-Pd gt + Ca-Pv, Ring +Stish
S3784	23.5	Pd, Ca-Baslt, Fo_{70}, Pd	Pd gt +Ca-Pv, Ca-Baslt gt + Ca-Pv, Mw + Pv, Stish + Mw +Pv + Cor

Table A.2: Electron microprobe data of the perovskites crystallized from the pressure calibrants in multi anvil experiments calculated based on 3 oxygens per formula unit. Fo30 (Forsterite 30), Fo70 (Forsterite 70)

Run no.	Pressure calibrant	Pressure	Si	Mg	Fe	Total
S3478	Fo30	23 GPa	0.961	0.763	0.310	2.034
S3784	Fo70	23.5 GPa	0.962	0.899	0.171	2.031

Table A.3: Electron microprobe data for all the experimental runs before processing of data. All the concentrations are in wt% oxide. (A) for experiments at 1600°C, (B) for experiments at 1400°C and (C) for reversal experiments. Results are listed as peridotite, basalt, pyrope and majorite based on the different garnet starting compositions as listed in table 2.1. (Abbreviation Pd gt–peridotitic garnet, Ca-Pv-calcium perovskite, Baslt gt-basaltic garnet, Maj gt –majoritic garnet, Pyr gt- pyrope garnet, Fo_{90}-forsterite 90 composition, Fo_{50}-forsterite 50 composition, Fo_{30}-forsterite 30 composition, (Mg,Fe)O-magnesiowüstite, SiO_2-stishovite,

(A) Runs at 1600°C.

(Run no.	Composition	Phases observed	SiO_2	MgO	FeO	CaO	Al_2O_3	Total
S3460	**Peridotite**	**Pd gt**	52.92	24.96	1.71	11.10	7.82	98.49
		Ca-Pv	59.54	10.71	0.77	16.88	3.12	91.03
	Basalt	**Baslt gt**	49.31	21.02	0.83	14.81	12.70	98.66
	Majorite	**Maj gt**	54.51	28.92	1.68	8.36	5.79	99.26
		Ca -Pv	47.89	0.09	0.00	44.03	0.01	92.02
	Fo 90	**Olivine**	42.18	56.04	2.32	0.02	0.10	100.66
S3470	**Peridotite**	**Pd gt**	53.26	25.98	1.12	11.21	8.26	99.82
		Ca-Pv	49.25	6.34	0.58	38.21	1.74	96.13
	Basalt	**Baslt gt**	49.17	22.74	0.55	14.09	13.23	99.77
	Pyrope	**Pyr gt**	46.97	19.24	0.82	16.16	16.30	99.48
		Ca-Pv	49.68	0.75	0.03	43.66	0.58	94.71
	Fo 90	**Olivine**	42.08	56.53	1.71	0.00	0.10	100.43
S3550	**Peridotite**	**Pd gt**	50.26	23.90	3.67	11.91	8.26	98.01
		Ca-Pv	50.08	0.17	0.10	47.33	0.08	97.77
	Basalt	**Baslt gt**	45.55	17.47	2.95	16.70	16.06	98.73
		Ca-Pv	47.57	2.16	0.42	43.91	1.84	95.89
	Pyrope	**Pyr gt**	47.39	20.84	3.49	14.30	12.83	98.84
		Ca-Pv	49.34	0.78	0.23	46.39	0.55	97.29
	Fo30	**olivine**	32.87	17.17	51.65	0.01	0.05	101.76
		(Mg,Fe)O	1.22	3.34	89.81	0.07	0.30	94.74
		SiO_2	98.20	0.27	2.06	0.01	0.21	100.75
S3548	**Peridotite**	**Pd gt**	51.49	27.95	3.90	7.95	8.33	99.62
		Ca-Pv	49.20	0.20	0.10	46.98	0.07	96.56
	Basalt	**Baslt gt**	47.90	24.00	5.07	9.83	12.45	99.25

	Fo30	**olivine**	33.86	17.88	49.40	0.02	0.05	101.21
		(Mg,Fe)O	3.68	8.78	85.02	0.02	0.04	97.54
		SiO_2	98.83	0.63	2.40	0.01	0.08	101.95
S3547	**Peridotite**	**Pd gt**	51.11	27.53	2.87	8.44	9.38	99.32
		Ca-Pv	50.24	0.13	0.06	47.51	0.07	98.00
	Basalt	**Baslt gt**	48.58	24.21	3.56	9.72	12.46	98.55
		Ca-Pv	46.68	0.62	0.24	46.01	0.57	94.12
	Fo30	**olivine**	33.66	18.91	49.39	0.00	0.05	102.02
		(Mg,Fe)O	2.93	9.40	87.59	0.00	0.07	99.98
		SiO_2	96.86	0.18	1.62	0.01	0.19	98.87
S3549	**Peridotite**	**Pd gt**	50.47	28.51	1.81	7.08	9.17	97.04
		Ca-Pv	45.78	1.70	0.22	44.84	0.84	93.38
	Basalt	**Baslt gt**	47.46	25.27	2.70	8.55	13.60	97.58
		Ca-Pv	48.52	0.36	0.10	46.44	0.10	95.52
	Pyrope	**Pyr gt**	44.08	20.65	2.82	11.52	17.84	96.91
	Fo30	**olivine**	33.65	21.30	45.37	0.00	0.06	100.39
		(Mg,Fe)O	1.08	7.40	87.90	0.02	0.17	96.57
		SiO_2	95.05	0.39	3.64	0.01	0.03	99.11
S3657	**Basalt**	**Basltic maj**	43.46	12.43	34.93	2.89	4.52	100.36
		Ca-Pv	48.27	0.35	0.30	46.38	0.33	95.62
	Fe+ basalt	**Baslt gt**	46.85	24.20	7.38	8.28	11.92	98.63
		Ca-Pv	48.04	0.19	0.12	46.26	0.32	94.93
	Fo30	**olivine**	33.67	21.25	45.76	0.00	0.06	100.75
		(Mg,Fe)O	2.84	4.62	86.96	0.06	0.38	94.87
		SiO_2	72.70	5.19	17.46	0.01	0.08	95.44
S3655	**Fe+ basallt**	**Baslt gt**	44.01	21.00	6.10	7.59	13.97	92.67
	Basalt	**Baslt gt**	48.48	26.19	4.02	7.73	12.57	98.99
		Ca-Pv	47.90	1.78	0.61	45.29	0.11	97.02
	Fo30	**olivine**	37.05	32.64	30.89	0.00	0.03	100.61
		(Mg,Fe)O						
		SiO_2	99.07	0.08	0.72	0.00	0.02	99.89
S3551	**Peridotite**	**Pd gt**	50.14	27.43	4.46	5.82	10.48	98.33
		Ca-Pv	48.22	0.23	0.16	46.70	0.57	95.88
	Basalt	**Baslt gt**	46.41	27.00	1.73	7.95	14.18	97.27

		Ca-Pv	39.42	0.92	0.24	43.37	3.69	87.64
	Pyrope	**Pyr gt**	45.03	21.99	3.80	9.54	18.46	98.82
		Ca-Pv	50.29	0.50	0.16	47.27	0.67	98.89
	Fo30	**olivine**	34.64	24.08	42.60	0.01	0.06	101.38
		(Mg,Fe)O	5.32	5.44	82.80	0.04	0.37	93.96
		SiO_2	94.77	1.42	4.41	0.02	0.06	100.67
S3480	**Peridotite**	**Pd gt**	53.91	28.18	4.23	4.92	8.64	99.88
		Ca-pv	51.35	0.07	0.03	50.05	0.03	101.53
	Basalt	**Baslt gt**	50.82	25.90	4.62	5.35	13.73	100.42
		Ca-Pv	50.85	0.09	0.09	49.40	0.05	100.48
	Pyrope	**Pyr gt**	46.51	19.56	8.61	8.77	16.70	100.15
		Ca-Pv	50.21	0.18	0.34	49.42	0.43	100.58
	Fo 50	**Olivine**	37.98	29.59	32.44	0.00	0.07	100.07
		SiO_2	101.54	0.05	0.54	0.02	0.03	102.17
S3498	**Peridotite**	**Pd gt**	53.22	32.12	5.44	0.71	9.53	101.02
		Ca-pv	51.29	0.70	0.18	45.56	0.26	97.98
	Basalt	**Baslt gt**	48.00	27.10	4.76	4.66	15.64	100.16
		Ca-Pv	50.54	0.31	0.11	45.32	0.22	96.50
	Pyrope	**Pyr gt**	45.16	24.71	3.95	5.38	21.49	100.68
		Ca-Pv	50.52	0.20	0.09	45.82	0.10	96.73
	Fo 50	**Olivine**	38.72	37.48	26.17	0.00	0.08	102.46
		(Mg,Fe)O	6.21	12.41	70.20	0.14	0.73	89.69
S3484	**Peridotite**	**Pd gt**	52.31	33.49	3.00	0.89	9.24	98.93
		Ca-pv	53.01	1.76	0.12	42.10	0.49	97.48
	Basalt	**Baslt gt**	47.63	28.78	3.44	2.38	16.66	98.88
		Ca-Pv	51.29	0.23	0.09	46.93	0.09	98.63
	Pyrope	**Pyr gt**	44.03	25.42	3.84	2.04	23.32	98.64
		Ca-Pv	49.31	1.60	0.33	45.24	1.43	97.91
	Fo 50	**Olivine**	37.01	30.79	31.97	0.00	0.09	99.87
		(Mg;Fe)O	0.71	21.41	75.89	0.00	0.12	98.13
S3475	**Peridotite**	**Pd gt**	53.23	31.49	5.09	0.86	9.61	100.27
		Ca-Pv	48.06	6.17	1.13	35.97	2.09	93.42
	Basalt	**Baslt gt**	49.03	27.26	3.28	3.03	17.03	99.62
		Ca-Pv	46.97	0.43	0.15	45.41	0.72	93.68

	Majorite	**Maj gt**	49.32	16.34	2.41	21.32	7.36	96.75
		Ca -Pv	49.06	0.96	0.20	44.84	0.58	95.64
	Pyrope	**Pyr gt**	44.96	24.00	3.58	5.04	22.35	99.94
		Ca-Pv	42.84	0.52	0.26	44.77	2.38	90.77
S3478	**Peridotite**	**Pd gt**	51.90	33.15	5.20	0.20	9.09	99.53
		Ca-pv	48.86	0.15	0.11	46.80	0.08	96.00
	Basalt	**Baslt gt**	47.40	28.31	4.42	2.96	16.32	99.41
		Ca-Pv	42.92	0.95	0.41	45.06	2.56	91.89
	Pyrope	**Pyr gt**	44.22	24.56	4.81	4.28	21.55	99.41
		Ca-Pv	45.29	1.30	0.58	44.21	2.20	93.58
	Fo 50	**Pv**	51.19	27.09	19.74	0.24	1.92	100.19
		(Mg,Fe)0	0.38	20.28	78.75	0.00	0.10	99.51
		SiO_2	97.62	0.37	2.18	0.00	0.02	100.19
S3757	**Peridotite**	**Pd gt**	52.37	29.20	4.14	4.48	8.42	98.61
		Ca-pv	47.99	0.39	0.25	45.93	0.73	95.29
	Basalt	**Baslt gt**	47.64	24.98	3.36	6.26	15.54	97.78
		Ca-Pv	44.64	1.13	0.49	43.13	1.16	90.55
	Fo50	**Olivine**	34.19	26.74	39.20	0.02	0.10	100.25
		(Mg,Fe)0	0.22	14.33	82.58	0.02	0.09	97.23
		SiO2	79.56	7.10	12.08	0.02	0.17	98.93
	Fo 30	**Olivine**	35.04	25.43	40.32	0.01	0.07	100.86
		(Mg,Fe)0	0.94	13.63	84.07	0.01	0.08	98.73
		SiO_2	94.94	1.56	3.37	0.02	0.21	100.10
S3764	**Peridotite**	**Pd gt**	52.70	28.41	4.82	3.67	9.60	99.19
		Ca-pv	48.12	1.14	0.19	43.70	0.96	94.11
	Basalt	**Baslt gt**	48.06	27.32	3.58	4.68	15.44	99.09
		Ca-Pv	49.43	0.04	0.04	46.96	0.03	96.50
	Fo30	**Olivine**	35.64	27.84	37.14	0.00	0.09	100.70
		(Mg,Fe)0	1.98	17.16	80.91	0.01	0.10	100.16
		SiO_2	90.05	4.11	7.14	0.00	0.25	101.56
S3784	**Peridotite**	**Pd gt**	51.46	32.16	4.87	0.50	10.17	99.15
		Ca-pv	49.83	0.29	0.13	46.69	0.26	97.19
	Fo70	**(Mg,Fe)0**	6.90	29.88	64.18	0.04	0.01	101.01
		Pv	55.18	34.70	11.18	0.16	0.08	101.30

S3783	**Peridotite**	**Pd gt**	51.34	30.92	5.77	1.45	9.39	98.87
		Ca-Pv	49.22	0.58	0.19	45.07	0.36	95.43
	Basalt	**Baslt gt**	50.28	15.75	2.98	23.26	4.87	97.15
		Ca-Pv	48.47	0.24	0.13	44.60	0.29	93.72
	Majorite	**Maj gt**	49.83	11.87	2.27	28.60	3.73	96.29
		Ca-Pv	49.04	0.16	0.08	45.60	0.11	94.99
	Fo70	**Olivine**	37.18	32.30	31.24	0.00	0.07	100.79
		(Mg,Fe)0	8.31	12.62	74.94	0.11	0.60	96.58
		SiO_2	91.16	1.26	3.35	0.02	0.15	95.93

(B) Runs at 1400°C

Run no.	Composition	Phases observed	SiO_2	MgO	FeO	CaO	Al_2O_3	Total
S3611	**Pyrope**	**Pyr gt**	44.92	18.91	2.48	14.50	19.34	100.14
		Ca-Pv	48.94	0.44	0.12	45.83	0.45	95.78
	Basalt	**Basalt gt**	46.66	19.99	3.38	14.66	15.74	100.42
		Ca-Pv	49.61	0.93	0.18	46.22	0.50	97.43
	Peridotite	**Pd gt**	51.22	26.26	4.36	9.21	8.56	99.61
		Ca- Pv	49.55	0.19	0.12	47.35	0.05	97.26
S3614	**Pyrope**	**Pyr gt**	44.15	19.66	3.29	13.64	18.79	99.53
		Ca-Pv	48.32	0.22	0.12	47.13	0.38	96.18
	Basalt	**Basalt gt**	47.00	23.50	3.77	11.35	14.07	99.69
		Ca-Pv	48.49	0.28	0.12	47.16	0.36	96.41
	Peridotite	**Pd gt**	50.74	27.91	4.54	8.60	8.24	100.03
		Ca- Pv	49.20	0.11	0.11	47.41	0.13	96.96
H2375	**Pyrope**	**Pyr gt**	45.21	18.65	3.23	14.01	17.93	99.02
		Ca-Pv	50.21	0.10	0.06	46.94	0.08	97.39
	Basalt	**Basalt gt**	47.46	20.57	3.73	13.36	13.67	98.79
		Ca-Pv	48.97	0.18	0.13	46.71	0.17	96.15
H2370	**Pyrope**	**Pyr**	44.03	23.22	4.08	6.33	22.52	100.18
		Ca-Pv	50.22	0.07	0.09	47.55	0.06	97.99
	Fo 30	**olivine**	33.45	20.65	51.13	0.01	0.04	105.28
		(Mg,Fe)O	0.75	3.24	93.06	0.10	0.31	97.46
		SiO_2	94.96	0.53	2.74	0.15	0.16	98.54
H2241	**Pyrope**	**Pyr gt**	44.04	22.89	3.25	6.31	21.20	97.68

(C) Reversal runs at 1600°C

Run no.	Composition	Phases observed	SiO_2	MgO	FeO	CaO	Al_2O_3	Total
S3538	**Ca-basalt**	**Ca-baslt gt**	44.76	25.91	0.88	7.44	16.02	95.00
S3543	**Ca-basalt**	**Ca-baslt gt**	43.36	24.25	2.65	7.11	18.41	95.78
S3515	**Ca-basalt**	**Ca-baslt gt**	48.26	28.28	4.15	2.67	17.00	100.37
		Ca-Pv	42.96	1.99	0.50	43.16	0.93	89.54
S3521	**Ca-Peridotite**	**Ca-Pd gt**	53.18	32.04	4.87	0.74	8.99	99.82
S3523	**Ca-basalt**	**Ca-baslt gt**	48.75	24.30	4.08	8.45	14.39	99.97
		Ca-Pv	42.85	12.67	2.18	24.56	8.93	91.19
S3784	**Ca-basalt**	**Ca-baslt gt**	46.26	23.36	4.19	4.91	19.01	97.73

Appendix B

Table B.1: Run details of the perovskite single crystal synthesis using multianvil press (see table 3.2 for crystal compositions). The run numbers marked with stars produced the sample with suitable size for compression experiments. For crystal 4 we could only produced tiny crystal aggregates, which were not suitable for compression experiments. (Details in Chapter 3)

Run no.	Pressure Assembly	Pressure GPa	Temperature °C	Capsule	Duration
Crystal 1					
H2351	8/3	25	2000	Re	10 minutes
H2363	8/3	25	2000-1900	Re	1 hr
H2369*	8/3	25	2000	Re	½ hr
Crystal 2 (fluxed with H_2O)					
H2417	8/3	25	1900-1800	Au	Blow out
H2428	8/3	25	~1550	Au	45 minutes
H2430	8/3	25	1700	Au	5 minutes
H2428	8/3	25	1700	Au	1 hr
H2438*	8/3	25	1800	Au	10 minutes
Crystal 3					
S3602*	7/3	25	1100	Pt	2 hrs
Crystal 4 (fluxed with H_2O)					
H2454	8/3	25	1800	Au	20 minutes
H2460	8/3	25	1900	Au	10 minutes
H2491	8/3	25	1900	Au	15 minutes
H2496	8/3	25	1950	Au	15 minutes
H2536	8/3	25	~1975	Au	10 minutes
H2538	8/3	25	~1920	Au	10 minutes
H2563	8/3	25	2000	Au	5 minutes
H2565	8/3	25	1900	Au	5 minutes
H2569	8/3	25	1900-1700	Au	1 hr
H2528	8/3	25	~1600	Au	1hr

References

Allan, D. R., Miletich, R. and Angel, R. J. (1996) A diamond-anvil cell for single-crystal x-ray diffraction studies to pressures in excess of 10 GPa. *Review of Scientific Instruments*, 67: 840-842.

Allègre, C. J., Poirier, J. P., Humler, E. and Hofmann, A. W. (1995) The chemical composition of the Earth. *Earth and Planetary Science Letters*, 134: 512-526.

Akaogi, M. and Akimoto, S. (1977) Pyroxene and Garnet solid solution equilibria in the systems $Mg_4Si_4O_{12}$-$Mg_3Al_2Si_3O_{12}$ and $Fe_4Si_4O_{12}$-$Fe_3Al_2Si_3O_{12}$ at high pressure and temperatures. *Physics of the Earth and Planetary Interiors*, 15: 90-106.

Akaogi, M., Navrotsky, A., Yagi, T. and Akimoto, S. (1987) Pyroxene-garnet transformation: Thermochemistry and elasticity of garnet solid solutions and application to a pyrolite mantle. In Syono Y. and Manghnani, M. H., editors, *High-pressure research in Mineral Physics*, p. 251-260, Terra Scientific Publishing Co., Tokyo/American Geophysical Union, Washington, DC.

Akaogi, M. (1990) Thermodynamics and stability relations of Mantle minerals. In Marumo, F., editor, *Dynamic processes of Material Transport and Transformation in the Earth's interior*, p. 239-251,Terra Scientific publishing company, Tokyo.

Akaogi, M., Ohmure, N. and Suzuki, T. (1998) High-pressure dissociation of $Fe_3Al_2Si_3O_{12}$ garnet: phase boundary determined by phase equilibrium experiments and calorimetry. *Physics of Earth and Planetary Interiors*, 106: 103-113.

Akaogi, M. and Ito, E. (1999) Calorimetric study on majorite–perovskite transition in the system $Mg_4Si_4O_{12}$-$Mg_3Al_2Si_3O_{12}$: transition boundaries with positive pressure–temperature slopes. *Physics of Earth and Planetary Interiors*, 114: 129-140.

Akaogi, M., Tanaka, A. and Ito, E. (2002) Garnet-ilmenite-perovskite transitions in the for mantle structure. *Physics of Earth and Planetary Interiors,* 132: 303-324.

Amthauer, G., Grodzicki, M., Lottermose, W. and Redhammer, G. (2004) Mössbauer Spectroscopy: Basic principles. In Beran, A. and Libowitzky, E., editors, *Spectroscopic Methods in Mineralogy*,

volume 6 of *European Mineralogical Union Notes in Mineralogy*, p 345-367, Eötvös University Press, Budapest.

Anderson, D. L. (1983) Chemical composition of the mantle. *Journal of Geophysical Research*, 88: B41-B52.

Anderson, O. L., Masuda, K.and Guo, D. (1995) Pure silicate perovskite and the PREM lower mantle model: a thermodynamic analysis. *Physics of the Earth and Planetary Interiors*, 89(15): 35-49.

Andrault, D., Bolfan-Casanova, N. and Guignot, N. (2001) Equation of state of lower mantle (Al,Fe)-$MgSiO_3$ perovskite. *Earth and Planetary Science Letters*, 193: 501-508.

Angel, R. J. (2000) Equations of state. In. Hazen, R. M and Downs, R. T., editors, *High-Temperature and High–Pressure Crystal Chemistry*, volume 41 of *Reviews in Mineralogy and Geochemistry*, p., 35-59, Mineralogical Society of America, Chantilly, Virginia.

Angel, R. J., Downs, R. T. and Finger, L. W. (2000) High-temperature-High-pressure diffractometry. In. Hazen, R. M and Downs, R. T., editors, *High-Temperature and High–Pressure Crystal Chemistry*, volume 41 of *Reviews in Mineralogy and Geochemistry*, p. 521-527, Mineralogical Society of America, Chantilly, Virginia.

Birch, F. (1947) Finite elastic strain of cubic crystals. *Physical Reviews*, 8: 625–630.

Boyd, F. R. and England, J. L. (1960) Apparatus for phase equilbria measurements at pressures up to 50 kbars and temperatures up to 1750°C. *Journal of Geophysical Research*, 65: 741-748.

Bolfan-Casanova, Keppler, H. and Rubie, D. C. (2000) Water partitioning between nominally anhydrous minerals in the MgO-SiO2-H2O system up to 24 GPa: implications for the distribution of water in the Earth's mantle. *Earth and Planetary Science Letters*, 182: 209-221.

Brown, J. M. and Shankland, T. J. (1981) Thermodynamic parameters in the Earth as determined from seismic profiles. *Geophyiscal Journal of Royal Astronomical Society*, 66: 579-596.

Cammarano, F., Goes, S., Vacher, P. and Giardini, D. (2003) Inferring upper mantle temperatures from seismic velocities. *Physics of Earth and Planetary Interiors*, 138: 197-222.

Cammarano, F., Deuss, A., Goes, S. and Giardini, D. (2005). One-dimensional physical reference models for the upper mantle and transition zone: combining seismic and mineral physical constraints. *Journal of Geophysical Research*, 110(B01306), doi: 10.1029/2004JB003272.

Cammarano, F., Goes, S., Deuss, A. and Giardini, D. (2005). Is pyrolitic adiabatic mantle compatible with seismic data? *Earth and Planetary Science Letters*, 232(3-4): 227-243.

Canil, D., (1994) Stability of clinopyroxene at pressure–temperature conditions of the transition region. *Physics of the Earth and Planetary Interiors*, 86: 25-34.

Charlu, T. V., Newton, R. C. and Kleppa, O. J. (1975) Enthalpies of formation at 970 K of compounds in the system MgO-Al_2O_3-SiO_2 from high temperature solution calorimetry. *Geochimica et Cosmochimica Acta*, 39: 1487-1497.

Christensen, U. R. (1994) Segregation of subducted oceanic crust in the convecting mantle. *Journal of Geophysical Research*, 99(B10): 19867-19884.

Christensen, U. R. (1997) Influence of chemical buoyancy on the dynamics of slab in the transition zone. *Journal of Geophysical Research*, 102: 22435-22443.

Conrad, P. G., Zha, C. S., Mao, H. K. and Hemley, R. J. (1999) The high-pressure single crystal elasticity of pyrope, grossualr and andradite. *American Mineralogist*, 84: 374-383.

Daniel, I., Bass, J. D., Fiquet, G., Cardon, H., Zhang, J. and Hanfland, M. (2004) Effect of aluminium on the compressibility of silicate perovskite. *Geophysical Research Letters*, 31(L15608), doi: 10.1029/2004GL020213.

Daniel, I., Cardon, H. and Fiquet, G. (2001) Equation of state of Al-bearing perovskite to lower mantle pressure conditions. *Geophysical Research Letters*, 27: 21-24.

Duffy, T. S. and Wang, Yanbin (1998) Pressure-Volume-Temperature Equations of state. In Ribbe, P. H., editor, *Ultrahigh-pressure mineralogy Physics and Chemistry of the Earth's deep interior*, volume 37 of *Reviews in Mineralogy and Geochemistry,* p. 425-452, Mineralogical Society of America, Chantilly, Virginia.

Deuss, A. and Woodhouse, J. (2001) Seismic observations of splitting of the mid-transition zone discontinuity in earth's mantle. *Science*, 294: 354-357.

Deuss, A., Redfern, S., Chambers, K. and Woodhouse, J. H. (2006) The nature of the 660-kilometer discontinuity in Earth's mantle from global seismic observations of PP precursors. *Science*, 311: 198-201.

Dziewonski, A. M. and Anderson, D. L. (1981) Preliminary Reference Earth Model. *Physics of Earth and Planetary Interiors*, 25: 297–358.

Fabrichnaya, O. B., Saxena, S. K., Richet, P. and Westrum E. F. (2004) *Thermodynamic data, models and phase diagrams in multicomponent oxide systems*. Springer, Berlin-Heidelberg-New York, p 198.

Fei, Y., Mao, H. K. B. and Mysen, O. B. (1991) Experimental determination of element partitioning and calculation of phase relations in the MgO -FeO -SiO_2 system at high pressure and high temperature. *Journal of Geophysical Research,* 96: 2157-2169.

Fei, Y., Mao, H. K., Shu, J. and Hu, J. (1992) P-V-T equation of state of magneiowüstite. *Physics and Chemistry of Minerals*, 18: 416-422.

Fei, Y., Wang, Y. and Finger, L. W. (1996) Maximum solubility of FeO in (Mg, Fe)SiO_3-perovskite as a function of temperature at 26Gpa: implication for FeO content in the lower mantle. *Journal of Geophysical Research*, 101(B5): 11525-11530.

Fei, Y. and Bertka, C. M. (1999) Phase transitions in the Earth's mantle and mantle mineralogy. In Fei, Y., Bertka, C. M. and Mysen, B. O., editors, *Mantle petrology: Field observations and high pressure experimentation*: *A tribute to Francis R. Boyd*, volume 6 of *The Geochemical Society special Publication*, p 189-207. The Geochemical Society, Houston.

Fei, Y., van Orman, J., Li, J., van Westrenen, W., Sanloup, C., Minarik, W., Hirose, K., Komabayashi, T., Walter, M. and Funakoshi, K. (2004) Experimentally determined post-spinel transformation boundary in Mg_2SiO_4 using MgO as an internal pressure standard and its geophysical implications. *Journal of Geophysical Research*, 109(B02305), doi: 10.1029/2003JB002562.

Fiquet, G., Andrault, D., Dewaele, A., Charpin, T., Kunz, M. and Haüsermann, D. (1998) P-V-T equation of state of $MgSiO_3$ perovskite. *Physics of Earth and Planetary Interiors*, 105: 21-31.

Fiquet, G., Dewaele, A., Andrault, D., Kunz, M. and Le Bihan, T. (2000) Thermoelastic properties and crystal structure of $MgSiO_3$ perovskite at lower mantle pressure and temperature conditions. *Geophysical Reaserch Letters*, 27(1): 21-24.

Flanagan, M. P. and Shearer, P. M. (1998) Global mapping of topography on transition zone velocity discontinuities by stacking *SS* precursors. *Journal of Geophysical Research*, 103: 2673–2692.

Frost, D. J., Langenhorst, F., van Aken, P. (2001) Fe-Mg partitioning between ringwoodite and magnesiowüstite and the effect of pressure, temperature and oxygen fugacity. *Physics and Chemistry of Minerals*, 28: 455-470.

Frost, D. J. and Langenhorst, F. (2002) The effect of Al_2O_3 on Fe-Mg partitioning between magnesiowüstite and magnesium silicate perovskite. *Earth and Planetary Science Letters*, 199: 227-241.

Frost, D. J. (2003a) The structure and sharpness of $(Mg,Fe)_2SiO_4$ phase transformations in the transition zone. *Earth and Planetary Science Letters*, 216: 313-318.

Frost, D. J. (2003b) Fe^{2+}-Mg partitioning between garnet, magnesiowüstite, and $(Mg,Fe)_2SiO_4$ phases of the transition zone. *American Mineralogist*, 88: 387-397

Frost, D. J., Liebske, C., Langenhorst, F., McCammon, C., Trnnes, R. G. and Rubie, D. C. (2004) Experimental evidence for the existence of iron-rich metal in the Earth's lower mantle. *Nature*, 428: 409-412.

Frost, D. J., Poe, B. T., TrØnnes, R. G., Liebske, C., Duba, A., and Rubie, D. C. (2004) A new large volume multianvil system. *Physics of Earth and Planetary Interiors*, 143-144: 507-514.

Frost, D. J. (2006) The stability of hydrous mantle phases. In Keppler, H. and Smyth, J. R., editors, *Water in nominally anhydrous minerals*, volume 62 of *Reviews in Mineralogy and Geochemistry,* p. 243-271, Mineralogical Society of America, Chantilly, Virginia.

Frost, D. J. and Dolejs D. (2007) Experiemntal determination of the effect of H_2O on the 410 km discontinuity. *Earth and Planetary Science Letters*, 256(1-2): 182-195.

Frost, D. J. (2007) The upper mantle and transition zone. *Elements* (in press).

Funamori, N., Yagi, T., Utsumi, W., Kondo, T., Uchida, T. and Funamori, M. (1996) Thermoelastic properties of $MgSiO_3$ perovskite determined by in situ X-ray observations up to 30 GPa and 2000K. *Jouranl of Geophysical Research*, 101(B4): 8257-8269.

Gasparik, T. (1990) Phase relations in the Transition Zone. *Journal of Geophysical Research*, 95 (B10): 15751-15769.

Gasparik, T. (1996) Melting experiments on the enstatite-diopside join at 70-224 Kbar, including the melting of diopside. *Contributions to Mineralogy and Petrology*, 124: 139-153.

Gasparik, T. (2003) *Phase diagrams for geoscientists. An atlas of the Earth's interior*. Springer, Berlin Heidelberg New York, p 462.

Gilbert, F. and Dziewonski, A. M. (1975) An application of normal mode theory to the retrieval of structural parameters and source mechanisms from seismic spectra. *Philosophical Transactions Royal Society London*, A 278: 187–269.

Gilbert, H. J., Sheehan, A. F., Dueker, K. G. and Molnar, P. (2003) Receiver functions in the western United States, with implications for upper mantle structure and dynamics. *Journal of Geophysical Research*, 108, 10.1029/2001JB001194.

Galzer, A. M. (1972) The classification of tilted octahedra in perovskites. *Acta Crystallographica*, B28: 3384-3392.

Glazer, A. M. (1975) Simple ways of determining perovskite structures. *Acta Crystallographica,* A31: 756-762.

Gwanmesia, G. D., Liu, J., Chen, G., Kesson, S., Rigden, S. M. and Libermann, R. C. (2000) Elasticity of the pyrope ($Mg_3Al_2Si_3O_{12}$)-majorite ($MgSiO_3$) garnets solid solution. *Physics and Chemistry of Minerals*, 27: 445-452.

Harte, B., Harris, Hutchinson, M. T., G. R., Watt, M. C. and Wilding, M. C. (1999) Lower mantle mineral associations in diamonds from São Luiz, Brazil. In Fei, Y., Bertka, C. M. and Mysen, B. O., editors, *Mantle petrology: Field observations and high pressure experimentation*: *A tribute to Francis R. Boyd*, volume 6 of *The Geochemical Society Special Publication*, p 125-153. The Geochemical Society, Houston.

Haselton, H. T. and Newton, R. C. (1980) Thermodynamics of pyrope-grossular garnets and their stabilities at high temperatures and high pressures. *Journal of Geophysical Research,* 85: 6973-6982.

Hatch, D. M. and Ghose, S. (1989) Symmetry analysis of the phase transition and twinning in $MgSiO_3$ garnet: Implications to mantle mineralogy. *American Mineralogist*, 74: 1221-1224.

Heinemann, S., Sharp, T. G., Seifert, F. and Rubie, D. C. (1997) The cubic to tetragonal phase transition in the system majorite ($Mg_4Si_4O_{12}$)-pyrope ($Mg_3Al_2Si_3O_{12}$), and garnet symmetry in the Earth's transition zone. *Physics and Chemistry of Minerals*, 24: 206-221.

Heinrich, K. F. G. and Newbury, D. E. (1991) *Electron probe Quantitation*. Springer, p. 412.

Hemley, R. J. and Cohen, R. E. (1992) Silicate perovskite. *Annual Reviews in Earth and Planetary Science*, 20: 553-600.

Helffrich, G. R and Wood, B.J. (1996) 410 km discontinuity sharpness and the form of the olivine α-β phase diagram: resolution of apparent seismic contradictions. *Geophysical Journal International*, 126: F7-F12.

Helffrich, G. R. and Wood, B. J. (2001) The Earth's mantle. *Nature*, 412: 501-507.

Hirose, K and Fei, Y. (2002) Subsolidus and melting phase relations of basaltic composition in the uppermost lower mantle. *Geocheimca Cosmochimica Acta*, 66: 2099-2108.

Holzapfel, C., Rubie, D. C., Frost, D. J., Langenhorst, F. (2005) Fe-Mg interdiffusion in (Mg, Fe)SiO_3 perovskite and lower mantle reequilibration. *Science*, 309: 1707-1710.

Howard, C. J. and Stokes, H. T. (1998) Group theoretical analysis of octahedral tilting in perovskites, *Acta Crystallographica*, B54: 782-789.

Irifune, T. (1987) An experimental investigation of the Pyroxene- Garnet transformation in a pyrolite composition and its bearing on the constitution of the mantle. *Physics of the Earth and Planetary Interiors*, 45: 324-336.

Irifune, T. and Ringwood, A. E. (1993) Phase transformations in subducted oceanic crust and buoyancy relationships at depths of 600-800 km in the mantle. *Earth and Planetary Science Letters*, 117: 101-110.

Irifune, T. (1994) Absence of an aluminous phase in the upper part of the Earth's lower mantle. *Nature*, 370: 131-133.

Irifune, T. and Isshiki, M. (1998) Iron partitioning in a pyrolite mantle and the nature of the 410-km seismic discontinuity. *Nature*, 349: 409-411.

Irifune, T., Nishiyama, N., Kuroda, K., Inoue, T., Isshiki, M., Utsumi, W., Funakoshi, K-I., Urakawa, S., Uchida, T., Katsura, T. and Ohtaka, O. (1998) The post-spinel phase boundary in Mg_2SiO_4 determined by in situ x-ray diffraction. *Science*, 279: 1698-1701.

Ita, J. and Stixrude, L. (1992) Petrology, elasticity, and composition of the mantle transition zone. *Journal of Geophysical Research*, 97: 6849–6866.

Ito, E. and Takahashi, E. (1989) Post spinel transformations in the system Mg_2SiO_4-Fe_2SiO_4 and some geophysical implications. *Journal of Geophysical Research*, 94: 10637-10646.

Jackson, I. and Rigden, S. M. (1996) Analysis of P-V-T data: Constraints on the thermoelastic properties of high-pressure minerals. *Physics of Earth and Planetary Interiors*, 96: 85-112.

Jackson, J. M., Zhang, J., Shu, J., Sinogeikin, S. V. and Bass, J. D. (2005) High-pressure sound velocity and elasticity of aluminous $MgSiO_3$ perovskite to 45 GPa: implications for lateral heterogeneity in Earth's lower mantle. *Geophysical Research Letters*, 32L21305, doi: 10.1029/2005GL023522.

Javoy, M. (1995) The integral enstatite chondrite model of the Earth. *Geophysical Research Letters*, 22(16): 2219-2222.

Jeffreys, H. and Bullen, K: E. (1940) *Seismological Tables*. British Association Seismological Committee, London.

Jiang, F., Speziale, S. and Duffy, T. S. (2004) Single-crystal elasticity of grossular-and almandine-rich garnets to 11 GPa by Brillouin scattering. *Journal of Geophysical Research*, 109, 10.1029/2004JB003081.

Karason H. and van der Hilst, R. D. (2000) Constraints on mental convection from seismic tomography, In Richards, M. A., Gordon R. G. and van der Hilst, R. D., editors, *History and dynamics of global plate motion*, volume 121 of *Geophysical Monograph Series*, p. 277-288, American Geophysical Union, Washington.

Karato, S-I and Jung, H. (1998) Water, partial melting and the origin of the low velocity and high attenuation zone in the upper mantle. *Earth and Planetary Science Letters*, 157(3-4): 193-207.

Katsura, T. and Ito, E. (1989) The system Mg_2SiO_4-Fe_2SiO_4 at high pressures and temperatures: Precise determination of stabilities of olivine, modified spinel, and spinel. *Journal of Geophysical Research*, 94(B11): 15663-15670.

Katsura, T., Yamada, H., Shinmei, T., Kubo, A., Ono, S., Kanzaki, M., Yoneda, A., Walter, M. J., Ito, E., Urakawa, S., Funakoshi, K. and Utsumi, W. (2003) Post-spinel transition in Mg_2SiO_4 determined by high P-T in situ X-ray diffractometry. *Physics of the Earth and Planetary Interiors*, 136: 11-24.

Kawai, N. and Endo, S. (1970) The generation of ultrahigh pressures by a split sphere apparatus. *Review of scientific Instruments*, 41: 1178-1181.

Kennett, B. L. N. and Engdahl, E. R. (1991) Travel times for global earthquake location and phase identification. *Geophysical Journal International*, 105: 429–465.

Kennett, L. N., Engdahl, E. R. and Buland, R. (1995) Constraints on the velocity structure in the Earth from travel times. *Geophysical Journal International*, 122: 108–124.

Keppler, H. and Frost, D. C. (2005) Introduction to minerals under extreme conditions. In Miletich, R., (editor), *Mineral behaviour at extreme conditions*, volume 7 of *European Mineralogical Union Notes in Mineralogy*, p. 1- 7, Eötvös University press, Budapest.

Kiefer, B., Stixrude, L., Hafner, J. and Kresse, G. (2001) Structure and elasticity of wadsleyite at high pressures. *American Mineralogist*, 86: 1387-1395.

King, H. E. and Finger, L. W. (1979) Diffracted beam crystal centering and its application to high-pressure crystallography. *Journal of Applied Crystallography*, 12: 374-378.

Kleppa, O. J. (1976) Mineralogical applications of high–temperature reaction calorimetry. In Strens, R. G. J., editor, *The physics and chemistry of Rocks and Minerals*, p. 369-387, New York, Wiley

Knittle, E. and Jealoz, R. (1987) Synthesis and equation of state of $(Mg,Fe)SiO_3$ perovskite to over 100 GPa. *Science*, 235: 688-670.

Kubo, A., Yagi, T., Ono, S. and Akaogi, M. (2000) Compressibilty of $Mg_{0.9}Al_{0.2}Si_{0.9}O_3$ perovskite. *Proceedings of Japan Academy*, 76B: 103-107.

Kubo, T., Eiji Ohtani, E., Kondo, T., Kato, T., Toma, M., Hosoya, T., Sano, A., Takumi Kikegawa ,T. and Nagase, T. (2002) Metastable garnet in oceanic crust at the top of the lower mantle. *Nature*, 420: 803-806.

Lauterbach, S., McCammon, C. A., van Aken, P., Langenhorst, F. and Seifert, F. (2000) Mössbauer and ELNES spectroscopy of $(Mg,Fe)(Si,Al)O_3$ perovskite: a highly oxidised component of the lower mantle. *Contributions to Mineralogy and Petrology*, 138: 17-26.

Libermann, R. C. and Wang, Y. (1992) Characterisation of sample environment in a uniaxial split sphere apparatus. In Syono, Y. and Manghnani, M. H., editors, *High Pressure Research: Application to Earth and Planetary Sciences,* p. 19–31,Terra Scientific Publishing Co., Tokyo/American Geophysical Union, Washington, DC.

Li, B., Liebermann, R. C. and Weidner, D. J. (1998) Elastic Moduli of Wadsleyite (β-Mg_2SiO_4) to 7 Gigapascals and 873 Kelvin. *Science*, 281(5377): 675-677.

Li, B. and Li, B. (2003) Compressional and shear wave velocities of ringwoodite {gamma}-Mg_2SiO_4 to 12 GPa. *American Mineralogist*, 88: 1312-1317.

Li, L., Brodholt, J. P., Stackhouse, S., Weidner, D. J., Alfredsson, M. and Price, G. D. (2005) Elasticity of $(Mg,Fe)(Si,Al)O_3$- perovskite at high pressure. *Earth and Planetary Science Letters*, 240: 529-536.

Li, L., Weidner, D.J., Brodholt, J., Alfè, D., Price, G. D, Caracas, R. and Wentzcovitch, R. (2006) Elasticity of $CaSiO_3$ perovskite at high pressure and high temperature. *Physics of Earth and Planetary Interiors*, 155**:** 249–259.

Litasov, K. D. and Ohtani, E. (2005) Phase relations in hydrous MORB at 18-26 GPa: Implications for heterogeneity of the lower mantle. *Physics of Earth and Planetary Interiors*, 150: 239-263.

Mao, H. K., Hemley, R. J., Fei, Y., Shu, J. F., Chen, L. C., Jephcoat, A. P. and Wu, Y. (1991) Effect of pressure, temperature and composition on lattice parameters and density of $(Fe,Mg)SiO_3$ peovskites to 30 Gpa. *Journal of Geophysical Research*, 96(B5): 8069-8079.

Matsuzaka, K., Akaogi, M., Suzuki, T. and Suda, T. (2000). Mg-Fe partitioning between silicate spinel and magnesiowüstite at high pressure: experimental determination and calculation of phase relations in the system Mg_2SiO_4-Fe_2SiO_4. *Physics and Chemistry of Minerals*, 27: 310-319.

McCammon, C. (1997) Perovskite as a possible sink for ferric iron in the lower mantle. *Nature*, 387: 694-696.

McCammon, C. (1998) The crystal chemistry of ferric iron in $Fe_{0.05}Mg_{0.95}SiO_3$ perovskite as determined by Mössbauer spectroscopy in the temperature range 80-293K. *Physics and Chemistry of Minerals,* 25: 292-300.

McCammon, C. (2004) Mössbauer spectroscopy: applications, in Spectroscopic methods. In Beran, A. and Libowitzky, E., editors, *Spectroscopic Methods in Mineralogy*, volume 6 of *European Mineralogical Union Notes in Mineralogy*, p. 369-398, Eötvös University Press, Budapest.

McCammon, C. A., Lauterbach, S., Seifert, F., Langenhorst, F., and van Aken, P. A. (2004) Iron oxidation state in lower mantle assemblages I Empirical relations derived from high–pressure experiments. *Earth and Planetary Science Letters*, 222: 435-449.

McDonough, W. F. and Sun, S. S. (1995) The composition of the Earth. *Chemical Geology*, 20: 223-253.

Megaw, H. D. (1973) *Crystal structure: a working approach*, Philadelpheia, Saunders.

Meng, Y., Fei, Y., Weidner, D. J., Gwanmesia, G. D. and Hu, J. (1994) Hydrostatic compression of γ-Mg_2SiO_4 to mantle pressures and 700 K: Thermal equation of state and related thermoelastic properties. *Physics and Chemistry of Minerals*, 21: 407-412.

Miletich, R., Allan, D. R. and Kuhs, W. F. (2000) High-pressure single-crystal techniques. In Hazen, R. M. and Downs, R. T., editors, *High-Temperature and High–Pressure Crystal Chemistry*, volume 41 of *Reviews in Mineralogy and Geochemistry*, p. 445-519, Mineralogical Society of America, Chantilly, Virginia.

Miletich, R., (2005) Diffraction techniques: Shedding light on structural changes at extreme conditions. In Miletich, R., editor, *Mineral Behaviour at Extreme conditions*, in volume 7 of *European Mineralogical Union Notes in Mineralogy*, p. 281-331, Eötvos University Press, Budapest.

Murakami, M., Hirose, K., Kawamura, K., Sata, N., Ohisi, Y. (2004) Post perovskitephase transition in $MgSiO_3$, *Science*, 304(5672): 855-858.

Nasdala, L., Smith, D. C., Kaindal, R. and Zieman, M. A. (2004) Raman Spectroscopy: Analytical Perspectives in Mineralogical Research. In Beran, A. and Libowitzky, E., editors, *Spectroscopic Methods in Mineralogy*, volume 6 of *European Mineralogical Union Notes in Mineralogy*, p. 281-243, Eötvös University Press, Budapest.

Navrotsky, A. (1997) Progress and New directions in High temperature calorimetry revisited. *Physics and Chemistry of Minerals*, 24: 22-241.

Navrotsky, A. (1999) A lesson from ceramics, *Science*, 284: 1788-1789.

Navrotsky, A., Schoenitz, M., Kojitani, H., Xu, H., Zhang, J., Weidner, D. J., Jeanloz and R. (2003) Aluminium in magnesium silicate perovskite: formation, structure, and energetics of magnesium–rich defect solid solutions. *Journal of Geophysical Research*, 108(B7), 2330, doi: 10.1029/2002JB002055.

Navrotsky, A. (2004) Thermochemistry, energetic modeling and systematics. In Gramaccioli, C, editor, *Energetic modeling in minerals,* volume 4 of *European Mineralogical Union Notes in Mineralogy*, p. 5-31, Eötvös University Press, Budapest.

Newton, R. C., Charlu, T. V. and Kleppa, O. J. (1977) Thermochemistry of high pressure garnets and clinopyroxenes in the system CaO-MgO-Al_2O_3-SiO_2. *Geochimica et Cosmochimica Acta*, 41(3): 369-377.

Nishihara, Y. and Takahashi, E. (2001) Phase relation and physical properties of an Al-depleted komatiite to 23 GPa. *Earth and Planetary Science Letters*, 190: 65-77.

Nishio-Hammane, D., Nagai, T., Fujino, K., Seto, Y., Takafuji, N. (2005) Fe^{3+} and Al solubilities in $MgSiO_3$ perovskite: implications of the $Fe^{3+}AlO_3$ substitution in $MgSiO_3$ perovskite at the lower mantle conditions. *Geophysical Research Letters*, 32:L16306, doi: 10.1029/2005GL023529.

Ono, S., Kikegawa, T. and Iizuka, T. (2004) The equation of state of orthorhombic perovskite in a pyrolitic mantle upto 80 GPa: Implications for chemical composition of the lower mantle, *Physics of the Earth and Planetary Interiors,* 145(1-4): 9-17.

O'Neill, H. St. C. and Wood, B. J. (1979) An experimental study of Fe-Mg partitioning between garnet and olivine and its calibration as a geothermometer. *Contributions to Mineralogy and Petrology*, 70: 59–70.

Ralph, R. L. and Finger, L. W. (1982) A computer program for refinement of crystal orientation on matrix and lattice constants from diffractometer data with lattice symmetry constraints. *Journal of Applied Crystallography*, 15: 537-539.

Reed, S. (1996) *Electron Microprobe Analysis and Scanning Electron Microscopy in Geology*. Cambridge University Press, Cambridge, p. 187.

Richmond, N. C. and Brodholt, J. P. (1998) Calculated role of aluminium in the incorporation of ferric iron into magnesium silicate perovskite. *American Mineralogist*, 83(9-10): 947-951.

Ringwood, A. E. (1967) The pyroxene-garnet transformation in the Earth's mantle. *Earth and Planetary Science Letters,* 2: 255-263.

Ringwood, A. E. and Major, A. (1967) Some high-pressure transformations of geophysical significance. *Earth and Planetary Science Letters*, 2, 106-110.

Ringwood, A. E. (1975) *Composition and petrology of the Earth's mantle*. McGraw-Hill, New York, p. 618.

Ringwood, A. E. (1991) Phase transformations and their bearing on the constitution and dynamics of the mantle. *Geochemica Cosmochimica Acta*, 55: 2083-2110.

Robie, R. A., Hemmingway, B. S. and Fisher, J. R. (1978) Thermodynamic properties of minerals and related substances at 298.15 K and 1 bar pressure and at higher temperature. *US Geolological Survey Bulletin*, 1452, p. 456.

Ross, N. L. and Hazen, R. M. (1989) Single crystal X- ray diffraction study of $MgSiO_3$ perovskite from 77 to 400 K. *Physics and Chemistry of Minerals*, 16: 415-420.

Ross, N. L. and Hazen, R. M. (1990) High-pressure crystal chemistry of $MgSiO_3$ perovskite. *Physics and Chemistry of Minerals*, 17: 228-237.

Rubie, D. C. (1993) Mechanisms and kinetics of reconstructive phase transformations in the Earth's mantle. In Luth, R., editor, *Experiments at high pressure and Applications to the Earth's mantle*, p. 247-303, *Short course handbook*, Mineralogical Association of Canada, Edmenton.

Rubie, D. C., Karato, S., Yan, H. and O'Neill, H. S. C. (1993) Low differential stress and controlled chemical environment in multi anvil high pressure experiments. *Physics and Chemistry of Minerals*, 20: 315-322.

Samuel, H., Farnetani, C. G. and Andrault, D. (2005) Heterogeneous lowermost mantle: Compositional constraints and seismological observables. In van der Hilst, R. D., Bass, J. D., Matas, J. and Trampert, J. editors, *Earth's deep mantle structure, composition and evolution*, volume 160 of *Geophysical Monograph Series*, p. 101-116, American Geophysical Union, Washington D. C.

Sato, Y. (1977) Equation of state of mantle minerals through high pressure x -ray study. In *High Pressure Research in Geophysics,* p. 307-324, Academic Press, New York.

Shearer, P. M. (1990) Seismic imaging of upper-mantle structure with new evidence for a 520-km discontinuity, *Nature*, 344: 121-126.

Shearer, P. M. (1996) Transition zone velocity gradients and the 520-km discontinuity. *Journal of Geophysical Research*, 101: 3053-3066.

Shearer, P. M. (2000) Upper mantle discontinuities. In Karato, S., Forte, A. M., Liebermann, R. C., Musters G. and Stixrude, L., editors, *Earth's deep Interior: Mineral Physics and Tomography from the Atomic to Global Scale*, volume 117 of *Geophysical Monograph*, p. 115-131, American Geophysical Union, Washington, D.C.

Shim, S-H., Duffy, T. S. and Shen, G. (2001) The post-spinel transformation in Mg_2SiO_4 and its relation to the 660-km seismic discontinuity. *Nature*, 411: 571-574.

Sinogeikin, S. V. and Bass, J. D. (2002) Elasticity of majorite and a majorite-pyrope solid solution to high pressure: implications for the transition zone. *Geophysical Research Letters,* 29, 10.1029/2001GL013937

Sinogeikin, S. V., Bass, J. D. and Katsura, T. (2001) Single-crystal elasticity of g-$(Mg_{0.91}Fe_{0.09})_2SiO_4$ to high pressures and to high temperatures. *Geophysical Research Letters*, 28: 4335–4338.

Sinogeikin, S. V. and Bass, J. D. (2002) Elasticity of pyrope and majorite-pyrope solid solutions to high temperatures. *Earth and Planetary Science Letters*, 203: 549-555.

Skinner, B. J. (1966) Thermal expansion. In Clark, Jr. S. P., editor, volume 97 of *Hand Book of Physical Constants,* p. 75-95, Geological Society of America Memoir.

Smyth, D. M. (1989) Defects and structural changes in perovskite systems: from insulators to superconductors. *Crystal Lattice Defects Amorphous material*, 18: 355-375.

Stebbins, J. F. and Kroeker, S. (2001) The mechanism of solution of aluminium oxide in $MgSiO_3$ perovskite, *Geophysical Research Letters*, 28: 615-618

Stixrude, L. (1997) Structure and sharpness of phase transitions and mantle discontinuities. *Journal of Geophysical Research*, 102 (B7): 14835–14852.

Stixrude, L. and Lithgow-Bertelloni, C. (2005) Mineraolgy and elasticity of the oceanic upper mantle: origin of the low-velocity zone. Journal of Geophysical Research ,110(B03204) doi: 10.1029/2004JB002965.

Smyth, J. R. and Frost, D. J. (2002) The effect of water on the 410 km discontinuity –an experiemnatl study. *Geophysical Research Letters*, 298(10): 1231-1234.

Sun, S-s. and McDonough, W. F. (1989) Chemical and isotopic systematics of oceanic basalts: implications for mantle composition and processes. *Geological Society, London, Special Publications*, 42: 313-345.

Suzuki, I. (1975) Thermal expansion of periclase and olivine, and their anharmonic properties. *Journal of Physics of Earth*, 23: 145-159.

Tackley, P. J, Stevenson, D. J., Glatzmaier, G. A. and Schubert, G. (1993) Effects of an endothermic phase transition at 670 km depth in a spherical model of convection in the Earth's mantle. *Nature*, 361: 699-704.

Thompson. Jr. J. B. (1967) Thermodynamic properties of simple solutions. In Ableson, P. H., editor, vol 2 of *Reasearches in Geochemistry*, p. 340-361,Wiley, New York.

Trampert, J., Deschamps, F., Resovsky, A. and Yuen, D. 2004 Probabilistic tomography maps chemical heterogeneities throughout the lower mantle. *Science,* 306(8697): 853-856.

Utsumi, W., Funamori, N., Yagi, T., Ito, E., Kikegawa, T. and Shimomura, O. (1995) Thermal expansivity of $MgSiO_3$ perovskite under high pressures up to 20 GPa. *Geophysical Research Letters*, 22(9): 1005-1008.

Vanpeteghem, C. B., Zhao, J., Angel, R. J., Ross, N. L. and Bolfan-Casanova, N. (2006) Crystal structure and equation of state of $MgSiO_3$ perovskite. *Geophysical Research Letters*, 33, L03306 doi: 10.1029/2005GL024955.

Vanpeteghem, C. B., Angel, R. J., Ross, N. L., Jacobsen, S. D., Dobson, D. P., Litasov, K. D. and Ohtani, E. (2006) Al, Fe substitution in the $MgSiO_3$ perovskite structure: a single crystal X-ray diffraction study. *Physics of the Earth and Planetary Interiors*, 155: 96-103.

van Aken, P. A., Liebscher, B. and Styrsa, V. J. (1998) Quantitaive determination of iron oxidation states in minerals using Fe L2,3-edge electron energy-loss near-edge structure spectrscopy. *Physics and Chemistry of Minerals*, 25: 323-327.

van Cappellen, E. and Doukhan, J. C. (1994) Quantitative x-ray microanalysis of ionic compounds. *Ultramicrsocopy*, 53: 343-349.

van Keken, P. E., Hauri, E. H. and Ballentine, C. J. (2002) Mantle mixing: The generation, preservation, and destruction of chemical heterogeneity. *Annual Reviews in Earth and Planetary Science*, 30: 93-525.

van der Meijde, M., Van der Lee, S. and Giardini, D. (2005) Seismic discontinuities in the Mediterranean mantle. *Physics of Earth and Planetary Interiors*, 148: 233-250.

Vinograd, V. L., Winkler, B., Putnis, A., Kroll, H., Milman, V., Gale, J. D. and Fabrichnaya, O. B. (2006) Thermodynamics of pyrope-majorite, $Mg_3Al_2Si_3O_{12}$-$Mg_4Si_4O_{12}$ solid solution from atomistic model calculations. *Molecular simulations*, 32(2): 85-99.

Vinograd, V. L., Winkler, B., Wilson, D. J., Putnis, A. and Gale, J. D., (2006) Monte Carlo simulation of mixing in $Ca_3Fe_2Ge_3O_{12}$-$Ca_4Ge_4O_{12}$ garnets and implications for the thermodynamic stability of pyrope–majorite solid solution. *Physics and Chemistry of Minerals*, 33: 533-544.

Walker, D., Carpenter, M. A. and Hitch, C. M. (1990) Some simplifications to multi anvil devices for high-pressure experiments. *American Mineralogist*, 75: 1020-1028.

Walter, M, J. (2004) Melt extraction and compositional variability in mantle lithosphere. In Carlson, R. W. editor, *The Mantle and Core*, volume 2 of *Treaties on Geochemistry*, p. 363-394, Elsevier-Pergamon, Oxford.

Walter, M. J., Kubo, A., Yoshino, T., Brodholt, J., Koga, K. T. and Ohishi, Y. (2004) Phase relations and equation-of-state of aluminous Mg–silicate perovskite and implications for Earth's lower mantle. *Earth and Planetary Science Letters*, 222: 501-516.

Walter, M. J., Trønnes, R. G., Armstrong, L. S., Lord, O. T., Caldwell, W. A. and Clark, S. M. (2006) Subsolidus phase relations and perovskite compressibility in the system MgO-$AlO_{1.5}$-SiO_2 with implications for Earth's lower mantle. *Earth and Planetary Science Letters*, 248: 77-89.

Wang, Y., Weidner, D. J., Libermann, R. C. and Zhao, Y. (1994) PVT equation of state of (Mg,Fe)SiO_3 perovskite: constraints on composition of the lower mantle. *Physics of Earth and Planetary Interiors*, 83: 13-40.

Weidner, D. J. and Wang, Y. (2000) Phase Transformations: Implications for Mantle Structure. In Karato, S., Forte, A., Liebermann, R., Masters, G. and Stixrude, L., editors, *Earth's Deep Interior:*

Mineral Physics and Tomography From the Atomic to the Global Scale, volume 117 of *Geophysical Monograph,* p. 215-235, American Geophysical Union, Washington DC.

Wänke, H. G., Dreibus, E. and Jagoutz, E. (1984) Mantle chemistry and accretion history of the Earth. In, Kröner, A., Hansons G. N. and Goodwin, A. M., editors, *Archean Geochemistry*, p. 1-24, Springer-Verlag, Berlin.

Williams, D. B., and Carter, C. B. (1996) *Transmission Electron Microscopy: A textbook for Material Science*. Springer, NewYork, p. 729.

Williams, Q. and Garnero, E. J. (1996) Seismic evidence of partial melts at the base of the lower mantle. *Science*, 277(5326): 670-673.

Wood, B. J. and Fraser, D. J. (1977) *Elementary thermodynamics for geologists*. Oxford University press, Oxford, p. 303.

Wood, B. J. (1995) The effect of H_2O on the 410 km seismic discontinuity. *Science*, 268, 74-76.

Wood, B. J. and Rubie, D. C. (1996) The effect of alumina on phase transformations at the 660 km discontinuity from Fe-Mg partitioning experiments. *Science*, 273: 1522-1524.

Woodward, P. M. (1997) Octahedral tilting in perovskites I Geometrical considerations, *Acta Crystallographica*, B53: 32-43.

Yagi, T., Mao, H. K. and Bell, P. M. (1979) Lattice parameters and specific volume for the perovskite phase of ortho-pyroxene composition, $(Mg,Fe)SiO_3$. In *Year Book Carnegie Institution*, 78: 612-625, Washington.

Yagi, T., Okabe, K., Nishiyama, N., Kubo, A. and Kikegawa, T. (2004) Complicated effects of aluminium on the compressibility of silicate perovskite. *Physics of the Earth and Planetary Interiors*, 143-144: 81-91.

Yeganeh-Haeri, A. (1994) Synthesis and reinvestigation of the elastic properties of single crystal magnesium silicate perovskite. *Physics of Earth and Planetary Interiors*, 87: 111-121.

Yusa, H., Akaogi, M. and Ito, E. (1993) Calorimetric study of $MgSiO_3$ garnet and Pyroxene: Heat capacities, Transition enthalpies, and Equilibrium Phase relations in $MgSiO_3$ at high pressures and Temperatures. *Journal of Geophysical Research*, 98(B4): 6453-6460.

Zhao, Y., Weidner, D. J., Praise, J. B. and Cox, D. E. (1993a) Thermal expansion and structural distortion of perovskites-data for $NaMgF_3$ perovskite, *Physics of Earth and Planetary Interiors*, 76(1-2): 1-16.

Zhao, Y., Weidner, D. J., Praise, J. B. and Cox, D. E. (1993b) Critical phenomena and phase transition of perovskites-data for $NaMgF_3$ perovskite, *Physics of Earth and Planetary Interiors*, 76(1-2): 17-34.

Zhang, J. and Weidner, D. J. (1999) Thermal equation of state of aluminium-enriched silicate perovskite. *Science*, 284: 82-84.

Erklärung

Hiermit versichere ich, die vorliegende Arbeit selbstständig verfasst und keine anderen als die von mir angegebenen Quellen und Hilfsmittel benutzt zu haben.

Ferner erkläre ich, dass ich weder an der Universität Bayreuth, noch an einer anderen Hochschule versucht habe, eine Dissertation einzureichen, oder mich einer Promotionsprüfung zu unterziehen.

Ashima Saikia
Bayreuth, October 2007